TOTAL YIELD MEASUREMENTS FOR THE $^{24}Mg(\alpha,\gamma)^{28}Si$ and $^{27}Al(p,\gamma)^{28}Si$ REACTIONS

Thesis by

Peter Bruce Lyons

In Partial Fulfillment of the Requirements

For the Degree of

Doctor of Philosophy

California Institute of Technology

Pasadena, California

1969

(Submitted May 7, 1969)

ACKNOWLEDGMENTS

The author is happy to acknowledge the support and assistance of the entire staff of the Kellogg Radiation Laboratory. The friendly and stimulating research environment of this Laboratory would be difficult, if not impossible, to duplicate elsewhere.

Particular thanks are given to Professor W. A. Fowler and Professor C. A. Barnes for their guidance during the course of this project. Professor Fowler initially suggested the project and provided the astrophysical motivation. Professor Barnes provided much needed advice on many experimental details.

A substantial portion of the experimental work on the $^{27}Al(p,\gamma)^{28}Si$ reaction and the gamma ray spectrometer calibration was carried out in collaboration with Mr. J. W. Toevs and Dr. D. G. Sargood. The help of Mrs. B. A. Zimmerman, who provided guidance on many computing problems, is gratefully acknowledged. The pyrex target chambers would have been difficult to obtain without the cooperation and skill of Mr. F. Wild. Most of the results presented in this thesis have been presented at several colloquia, the APS 1968 Winter meeting, and in three articles submitted for publication.

Thanks for fellowship assistance are given to the National Science Foundation and the National Phi Kappa Phi Foundation. Graduate research assistantships from the California Institute of Technology are also gratefully acknowledged. This research program was supported in part by the Office of Naval Research [Nonr-220(47] and the National Science Foundation [GP-9114].

ABSTRACT

The $^{27}Al(p,\gamma)^{28}Si$ and $^{24}Mg(\alpha,\gamma)^{28}Si$ reactions have been investigated to provide the data needed for calculation of the ^{28}Si photodisintegration rate in astrophysical situations, particularly in the silicon-burning stage of stellar nucleosynthesis. A large solid angle NaI gamma ray spectrometer was employed which provided high detection efficiencies. The $^{27}Al(p,\gamma)^{28}Si$ reaction was investigated over the proton energy range 0.3 - 2.6 MeV; total gamma ray strengths were determined for 85 resonances. From 1.4 - 2.6 MeV, the gamma ray yield curve was measured and an upper limit for the nonresonant cross section was determined. Where possible, total resonance widths were deduced from the data. The gamma-ray detection efficiencies and target purity were investigated experimentally. Comparison was made with resonance strengths, measured by other methods, in the reactions $^{30}Si(p,\gamma)^{31}P$ and $^{26}Mg(p,\gamma)^{27}Al$. The reaction $^{24}Mg(\alpha,\gamma)^{28}Si$ was investigated for alpha particle energies up to 2.8 MeV; total gamma ray strengths were determined for 16 resonances, including a previously unreported resonance at 1.358 ± 0.007 MeV. Stellar interaction and photodisintegration rates were calculated from the measured resonance strengths, and semi-empirical fits to these rates were determined for use in astrophysical calculations.

TABLE OF CONTENTS

TABLE OF CONTENTS (continued)

TABLE OF CONTENTS (continued)

LIST OF FIGURES

I. INTRODUCTION

A. Astrophysical Motivation

Nuclear reactions have been believed for many decades to be the basic energy-generating mechanisms in stars, and the Kellogg Laboratory of the California Institute of Technology has been one of the leaders in experimental investigation of the nuclear parameters which must underlie a detailed theoretical understanding of the stages of stellar nucleosynthesis. These experimental investigations have taken many forms in searching for various aspects of nuclear structure in order to understand the behavior of these nuclei under particular stellar environments. The work described in this dissertation is a part of this continuing experimental program of astrophysically oriented measurements.

At the time the current program was initiated (1965), a late stage of stellar evolution, known as silicon-burning, was believed to follow the oxygen-burning stage (Fowler and Hoyle, 1964). The view held then was that oxygen-burning, a stage in which reactions between oxygen nuclei provide the stellar energy, would probably result in an element distribution peaked at ^{32}S, with appreciable amounts of other α-particle nuclei near ^{32}S. Further reactions between these heavy nuclei are improbable due to their high Coulomb barriers, and subsequent nucleosynthesis was believed to depend upon photodisintegration-rearrangement reactions. At temperatures of $T_9 \approx 2$ (where T_9 refers to temperature in units of $10^9\ ^oK$), only slightly above the oxygen-burning temperatures, the ^{32}S will photodisinte-

grate mainly into ^{28}Si, and since ^{28}Si has the slowest photodisintegration rate among the nuclei in this mass region, it was believed that a core consisting essentially of ^{28}Si would result. However, for $T_9 \gtrsim 3$, the ^{28}Si can be photodisintegrated on a reasonably short time scale. This photodisintegration through the (γ,p), (γ,α), and (γ,n) channels, and the subsequent more rapid photodisintegration of the products of the ^{28}Si photodisintegration, were believed to create a pool of free nucleons and alpha particles which would then serve to build toward the iron group nuclei, through very rapid capture of these particles on the remaining ^{28}Si nuclei. On this model, the photodisintegration rate $\lambda_\gamma(^{28}Si)$ determines the rate at which alphas and nucleons are made available, and hence the rate for buildup to the iron group, where the e-process (Fowler and Hoyle, 1964) was believed to determine the final abundances of the iron group nuclei.

This picture is now known to be an oversimplification of a more complicated state of affairs. The original view neglected the possibility of "back-currents" in the photodisintegration process, i.e., the possibility that the effect of photodisintegration might be partially canceled by its inverse reaction, for example

$$^{28}Si + \gamma \rightleftharpoons {}^{24}Mg + \alpha \ . \qquad (1)$$

Detailed studies by Bodansky, Clayton, and Fowler (1968) and by Truran, Cameron, and Gilbert (1966) have shown that this effect is not only present, but is in approximate equilibrium for the reaction given in equation 1 . The total rate at which alphas and nucleons are made available is no longer simply given by $\lambda_\gamma(^{28}Si)\, n(^{28}Si)$,

but instead is the leakage out of the above quasi-equilibrium, i.e., $\lambda_\gamma(^{24}Mg)\, n(^{24}Mg)$. The crucial point is that even though $\lambda_\gamma(^{28}Si) < \lambda_\gamma(^{24}Mg)$, the equilibrium concentration of ^{24}Mg, $n(^{24}Mg)$, is much less than $n(^{28}Si)$, due to the very strong binding of an alpha in ^{28}Si. Thus $\lambda_\gamma(^{28}Si)\, n(^{28}Si) >> \lambda_\gamma(^{24}Mg)\, n(^{24}Mg)$, which is a sufficient condition for the quasi-equilibrium of equation 1 to exist. These realizations have shifted the emphasis away from $\lambda_\gamma(^{28}Si)$ and have shown that $\lambda_\gamma(^{24}Mg)$ is, in fact, a more crucial parameter.

At the time the present work was begun, two goals were established: 1) a complete determination of $\lambda_\gamma(^{28}Si)$ through study of the inverse (radiative capture) reactions, and 2) the development of an experimental technique to obtain the data required for the calculation of $\lambda_\gamma(^{28}Si)$ which could be applied to other radiative capture cross sections of astrophysical interest.

As is shown in detail in Appendix I, the calculation of a photodisintegration rate, including the contribution of photodisintegration from excited states of, in this case, ^{28}Si, requires a knowledge of the <u>total</u> resonance strength $(2J+1)\Gamma_{p_0}\Gamma_\gamma/\Gamma$ (for calculations of (γ,p_0) photodisintegrations) for each resonance in the compound nucleus. In this expression Γ_γ is the total electromagnetic decay width of a given resonance level to all lower states. In addition to the contributions of the resonances, the possibility of a non-resonant contribution must be considered as well. The equation for λ_γ (equation 45) involves a sum over all resonances of the compound system, but two effects serve to limit the energy range over which the radiative capture reaction must be studied in detail, i.e., the

range of excitation energy over which resonances make substantial contributions to the total photodisintegration rate is limited. At low energies, the Coulomb barrier (represented by the Gamow-Condon-Gurney penetration factor) reduces particle widths. At high energies, the tail of the Planck radiation distribution reduces the importance of higher energy resonances by introducing a Boltzmann factor dependence on the excitation energy of the resonance. The product of these two factors exhibits a maximum at bombarding energy E_0, of full width Δ, which should contain the resonances making significant contributions to λ_γ. Expressions for this product have been derived in the literature (Fowler, Caughlan, Zimmerman, 1967; Fowler and Vogl, 1964; Clayton, p. 302, 1968) where it is shown that for the reaction $0 + 1 \rightarrow 2 + 3$,

$$E_0 = 0.122(Z_0^2 Z_1^2 A)^{1/3} T_9^{2/3} \text{ MeV} \qquad (2)$$

and

$$\Delta = 0.237(Z_0^2 Z_1^2 A)^{1/6} T_9^{5/6} \text{ MeV} \qquad (3)$$

where $A = A_0 A_1/(A_0+A_1)$. From these equations, one estimates that for the temperature range of interest, $1 < T_9 < 5$, data are needed for the $^{27}Al(p,\gamma)^{28}Si$ reaction from $E_p \sim 0.4$ MeV to ~ 3.0 MeV. For (γ,n) photodisintegrations, Coulomb effects are not present, but these photodisintegrations require gamma rays of much higher energy than do the (γ,p) and (γ,α) channels, and thus do not contribute appreciably to the total photodisintegration rate in the case under study.

B. State of Previous Knowledge

Both the $^{27}Al(p,\gamma)^{28}Si$ and $^{24}Mg(\alpha,\gamma)^{28}Si$ reactions have been studied previously by several groups and many references are cited in the review article by Endt and Van der Leun (1967). For the $^{27}Al(p,\gamma)^{28}Si$ reaction, for proton energies below 1.4 MeV, published strengths show discrepancies among the results of various experimental groups of at least a factor of two in some cases. Since at $T_9 = 5$ the $^{27}Al(p,\gamma)^{28}Si$ reaction contributes about 90% of the total photodisintegration rate of ^{28}Si, this spread in the literature values introduces essentially the same factor of two uncertainty in $\lambda_\gamma(^{28}Si)$. Above 1.4 MeV the available data were not sufficient for a calculation of the photodisintegration rate since only a few resonances had been studied in detail (Antoufiev et al., 1963; Gibson, Battleson, and McDaniels, 1968). Possibly the most important experimental discrepancies are between measurements based on resonance absorption techniques (Engelbertink and Endt, 1966) and those based on more conventional resonance yield techniques (Endt and Heyligers, 1960).

The $^{24}Mg(\alpha,\gamma)^{28}Si$ reaction, in the energy interval studied here ($E_\alpha \leq 2.8$ MeV), has been investigated by only one group (Smulders and Endt, 1962). The detection techniques developed for ^{28}Si resonance levels (for the $^{27}Al(p,\gamma)^{28}Si$ reaction) were directly applicable to the $^{24}Mg(\alpha,\gamma)^{28}Si$ reaction, and in this manner, resonance strengths could be determined for both reactions on a consistent absolute strength scale.

C. Experimental Considerations

A simplified level diagram for ^{28}Si is given in figure 1. In this work, the $^{27}Al(p,\gamma)^{28}Si$ reaction, which dominates the photodisintegration rate of ^{28}Si, was investigated over the energy range 0.3 - 2.6 MeV, thus covering most of the energy range required for calculation of photodisintegration rates for $T_9 \leq 5$. Reference to figure 1 shows that the Q of the $^{27}Al(p,\gamma)^{28}Si$ reaction is 11.58 MeV, thus excitation energies (and gamma ray energies) up to about 14 MeV must be considered. The $^{24}Mg(\alpha,\gamma)^{28}Si$ reaction, which contributes only about 10% of the total photodisintegration rate of ^{28}Si, was investigated in the present work only up to excitation energies of about 12.5 MeV.

Several techniques could be used to measure the total gamma ray strengths for the resonances of interest. For instance, for each resonance, a NaI(Tl) or Ge(Li) spectrum could be taken with sufficiently good counting statistics to allow careful peeling of the individual gamma ray contributions from the spectrum. In this way, the intensity of each transition contributing to de-excitation of the resonance level could be obtained. From this intensity information, the branching ratios of the various decays of the resonance could be inferred; an absolute intensity measurement for any one of the lines in the spectrum, together with the decay scheme of the resonance, would then allow the total gamma strength to be deduced. It must be emphasized, however, that while important nuclear spectroscopic data would thus be obtained, the astrophysical use of the data requires only the total gamma ray strength of each resonance.

FIGURE 1: Energy Level Diagram of ^{28}Si

The data concerning energies, spins and parities for the lower levels of ^{28}Si shown in this figure were taken from the compilation of Endt and Van der Leun (1967). Thresholds for the three photodisintegration channels of interest, (γ,p), (γ,α), and (γ,n), are indicated. The energy ranges studied in the current work for the inverse reactions to the first two photodisintegration channels are also indicated.

FIGURE 1

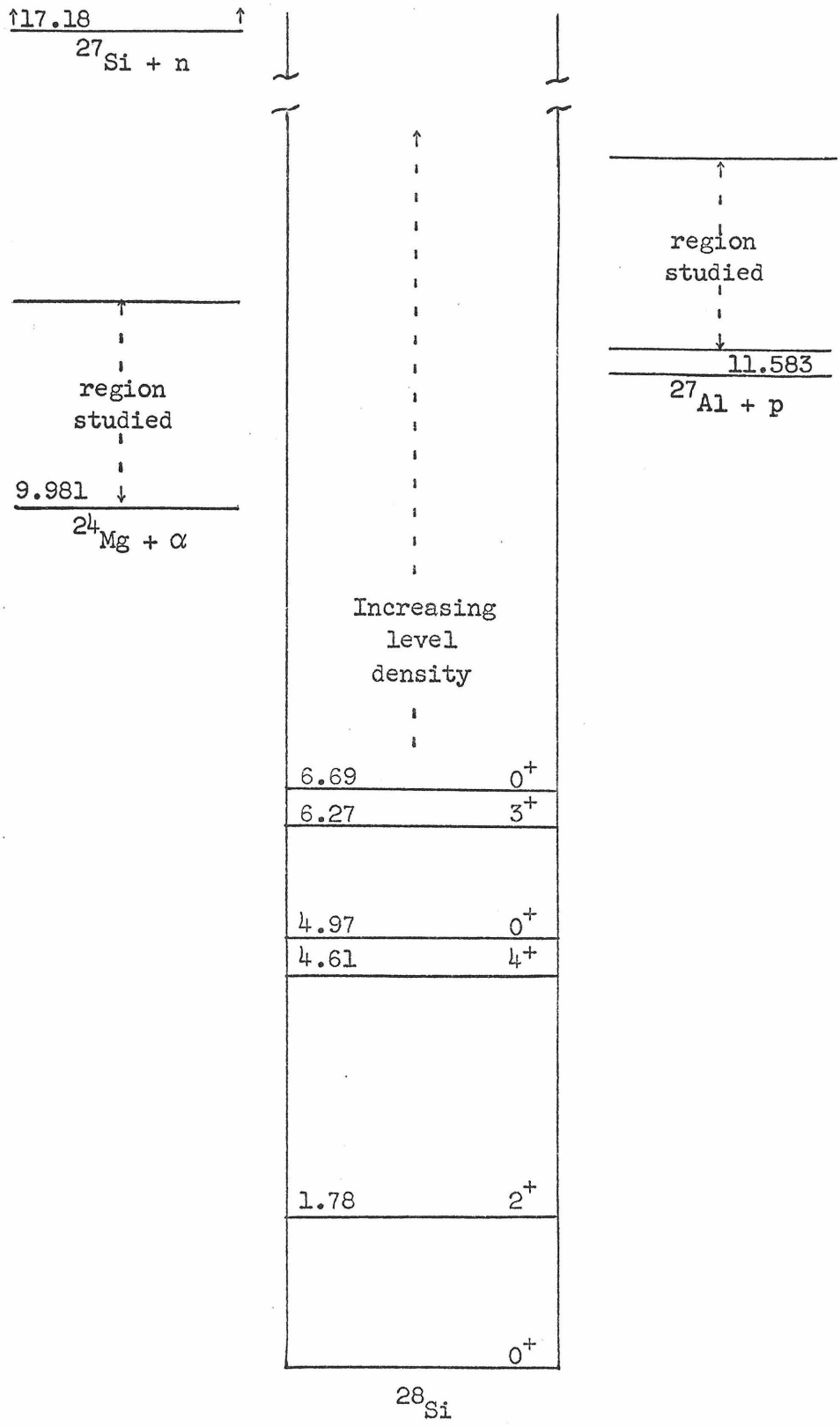
17.18
^{27}Si + n
region studied
9.981
^{24}Mg + α
Increasing level density
6.69 0+
6.27 3+
4.97 0+
4.61 4+
1.78 2+
0+
^{28}Si
region studied
11.583
^{27}Al + p

The spectrum peeling approach becomes prohibitively time-consuming when it is realized that there are at least 85 resonances in the region of interest for the $^{27}Al(p,\gamma)^{28}Si$ reaction alone. From the astrophysical viewpoint, a technique yielding less spectroscopic information, but consuming far less time than spectrum peeling is essential.

A detection technique whose efficiency does not depend on the detailed cascade structure of a resonance is needed. One such technique involves a detector of the type discussed by Moxon and Rae (1963; Macklin, Gibbons, and Inada, 1963), consisting of a thick gamma ray converter and a very thin plastic scintillator secondary electron detector. Because of the approximate constancy of the gamma ray conversion cross section and the approximately linear relation between electron energy and electron range in the converter plate, this detector has an efficiency which (although quite low) is very nearly proportional to the energy of the incident gamma ray. In the limit of detection efficiencies much less than unity, the detection probability for a cascade is just the sum of the individual efficiencies for the members of the cascade; thus for any cascade beginning from a fixed excitation energy, the detection efficiency is a constant. However, the pulse height distribution from the thin plastic scintillator gives no indication of the gamma ray spectrum, and hence no possibility of eliminating unwanted contributions produced by contaminant reactions. This lack of discrimination, as well as the low efficiency, rules out the Moxon-Ray detector for the present application.

An arrangement which combines high efficiency with the ability to distinguish most contaminant contributions is the total absorption detector in which every gamma ray emitted by the target is totally absorbed. Such a detector could consist, for instance, of a very large well-type crystal of NaI(Tl). This system would have a detection efficiency of unity for each radiative capture independent of the cascade structure, and each radiative capture would result (ideally) in a monoenergetic pulse from the scintillator. While a total absorption detector is feasible in principle, the material requirements for high energy gamma rays are excessively large. However, a practical compromise can be effected through the use of two large cylindrical NaI crystals placed on opposite sides of the target chamber, as close to the target as possible, with electrical summing of the phototube outputs. This was the technique adopted for the present work. With the largest NaI crystals available to us, the probability for a single gamma ray to interact through any process was ~ 0.5. Even though this efficiency differs substantially from unity, it is sufficiently high that detection efficiencies depend only slightly on the structure of a cascade. For purpose of reference, this technique will be called the semi-total absorption technique.

D. General Discussion of the Semi-Total Absorption System

Two general types of spectrum analysis (discussed in detail in part IV) were applied to the gamma ray spectra, but in all cases, the formula for the strength could be expressed schematically as, for the (p,γ) reaction,

$$(2J+1)\frac{\Gamma_p \Gamma_\gamma}{\Gamma} = CN_\gamma \qquad (4)$$

where N_γ denotes the total number of radiative capture processes proceeding through the resonance. The quantity C contains kinematical and statistical parameters as well as quantities depending on charge integration and target composition.

One method of analysis involved determination of the total number of interactions with the crystals, N_i, due to the reaction under study (including pulses resulting from interaction with the crystals of secondary Compton gamma rays or electrons from primary gamma rays converted outside the crystal volume). The total detection efficiency, ϵ_t, is defined as the probability that a gamma decay of a given resonance level will result in any kind of interaction with the crystals. Thus, in equation 4 ,

$$N_\gamma = N_i/\epsilon_t \quad . \qquad (5)$$

For the high efficiencies of the present geometry, ϵ_t is very insensitive to details of the cascade structure of a given resonance. However, for any resonance for which branching ratios were already known, the gamma ray detection efficiencies for single gamma rays (the determination of these efficiencies is dealt with in part III) could be used to calculate ϵ_t.

Because of various experimental difficulties, the entire pulse height spectrum could not always be used with confidence; thus N_i could not be obtained at all resonances. In these cases, only an $N_i'(f)$ could be reliably estimated, where this quantity is the number of

pulses larger than some fraction f of the full energy pulse E_x. A parameter $\eta(f)$ was defined as the probability that a gamma decay of a resonance resulted in an interaction with the NaI yielding a pulse height above fE_x. Thus the quantity N_γ in equation 4 can also be written as

$$N_\gamma = \frac{N_i'(f)}{\eta(f)} \quad . \tag{6}$$

It was determined that for an empirically chosen value f_0, η was relatively insensitive to cascade structure; thus for any resonance, N_γ could be obtained with acceptable precision from a measurement of $N_i'(f_0)$.

Part V discusses the use of N_γ in the two types of yield analysis utilized in this work. Parts VI and VII are concerned with the application of the detection and analysis techniques to the two reactions under study. Part VIII compares the resonance strengths obtained in this work with strengths obtained by previous workers; resonance strengths in reactions other than $^{27}Al(p,\gamma)^{28}Si$ and $^{24}Mg(\alpha,\gamma)^{28}Si$ are also briefly considered.

Of particular interest in this work were detailed tests of internal consistency, the goal being to avoid the dangerous "pitfalls" which can be present in yield analyses of this type. Part IX is devoted to these tests.

Astrophysical interaction rates and photodisintegration rates are given in Part X, and discussed in greater detail in Appendix I.

II. EXPERIMENTAL APPARATUS

The Caltech 3 MV electrostatic accelerator provided charged particle beams for all the absolute efficiency calibrations and resonance strength measurements. After a preliminary mass analysis with a small cross-field magnet, the beam passed through a 90^{o} double-focusing magnetic analyzer. The machine energy was regulated by controlling the corona load current from a signal obtained on slits following the 90^{o} analyzer. Tests of target composition, not involving detection of gamma rays, used electrostatic deflection of the beam into a small scattering chamber on another experimental beam line of the accelerator. The beam tube of the accelerator was pumped with baffled oil diffusion pumps.

All gamma ray measurements were carried out in a stainless steel and pyrex target system which was isolated from the beam tube by a 38 cm long, in-line, liquid-nitrogen-cooled trap. A schematic illustration of the system is given in figure 2. To reduce target contamination, only hydrocarbon-free pumping was used; roughing vacuum was obtained with a molecular sieve sorption pump and an Ultek 8 l/s ion pump was switched on at pressures below 5 microns. During operation typical pressures measured by the ion pump were $\sim 5\times10^{-7}$ Torr. Where O-ring seals were required (to the pyrex tube, teflon insulators, and to the movable target rod), only Viton O-rings were used. Apiezon-L vacuum grease (vapor pressure $\lesssim 10^{-10}$ Torr at room temperature) was used sparingly where lubrication was required.

A grounded tantalum collimator of 2.5 mm diameter was

FIGURE 2: Experimental Apparatus

This figure shows a schematic view of the experimental apparatus. Numbers on the figure refer to: 1-target, 2-electron suppressor, 3-beam defining aperture. The electron suppressor was maintained at -300 volts. Both the target and the internal silvering on the pyrex were used as a Faraday cup. (Not to scale.)

FIGURE 2

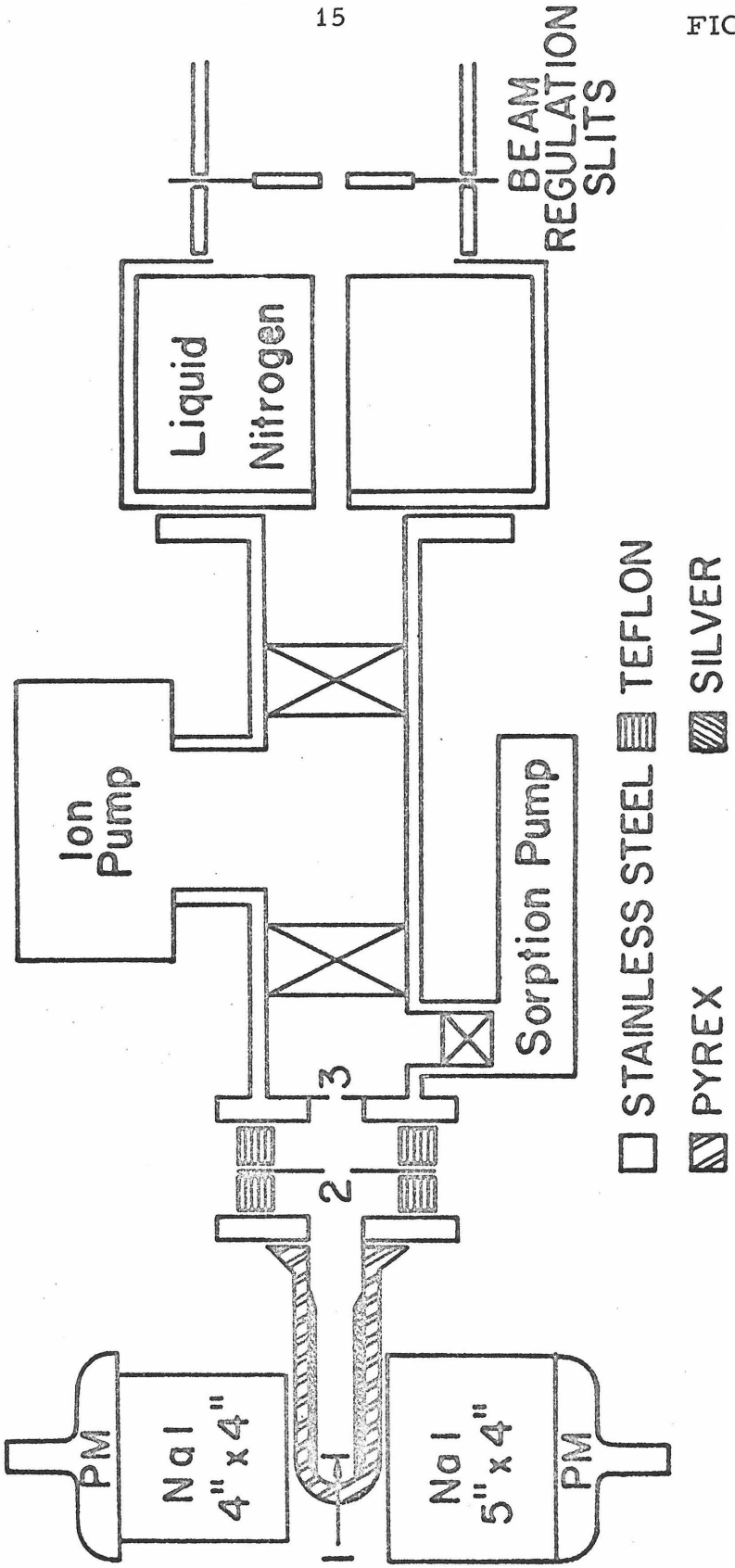
BEAM REGULATION SLITS
Liquid Nitrogen
Ion Pump
Sorption Pump
STAINLESS STEEL
TEFLON
PYREX
SILVER
PM
NaI 4" x 4"
NaI 5" x 4"
PM
1
2
3

followed by a tantalum suppressor ring maintained at -300 volts. The target was contained in a pyrex chamber fabricated by Mr. Fred Wild from 12 mm o.d. pyrex tubing. The chamber was silvered internally; a small window in the silver layer, which was normally covered by the target blank, was left to observe beam alignment, focusing, and target position. The silver layer was electrically connected to the target blank and the entire assembly was used as a Faraday cup. The Faraday cup was maintained at low potential (< +50 volts) by the beam current integration system. Current leakage was completely negligible. The beam integrator was frequently calibrated by recording the charging time for a known current.

For most of the measurements to be discussed, solid Ta target backings of 0.25 mm thickness were used. Targets were prepared by evaporation in vacuo onto these backings.

Two unshielded Harshaw NaI(Tl) crystals, 12.7 cm diameter × 10.2 cm long (5"×4") and 10.2 cm diameter×10.2 cm long (4"×4") were positioned on the two sides of the target chamber; their aluminum containers were separated by 13.5 mm. The 5"× 4" crystal was viewed by a CBS 7819 phototube and the 4" × 4" crystal was viewed by an RCA 2065 phototube. Both tubes were selected by Harshaw for low count-rate gain changes.

The gains of the two crystal-photomultiplier units were equalized by varying their individual high voltage supplies. The preamplifiers were slightly modified so the pulse output from a preamp could be switched off without disturbing the high voltage on the phototube or the output impedance (to the passive summing network) of the

preamplifier. The high voltage was left on the phototubes for a minimum of eight hours prior to any measurements to minimize gain drifts.

The two preamplifier outputs were fed into a passive summing network. After amplification, the pulses were fed into a single channel analyzer (SCA) and a RIDL 400-channel analyzer (PHA). The SCA drove a scaler and could also be used to gate the multichannel analyzer, when desired, to correlate the SCA bias level with PHA channel number. The beam current integrator (BCI) gated the analyzer, the scaler, a clock, and the beam (see figure 3).

The above portions of the apparatus were common to most of the measurements to be described. Experimental details relating to particular types of measurements will be described subsequently, together with the experimental results for that measurement.

FIGURE 3: Electronic Circuitry

This figure shows a block diagram of the electronic circuitry. The abbreviations used in the figure are: HV-adjustable high voltage supply, SCA-single-channel analyzer, PHA-pulse height analyzer, BCI-beam current integrator.

FIGURE 3

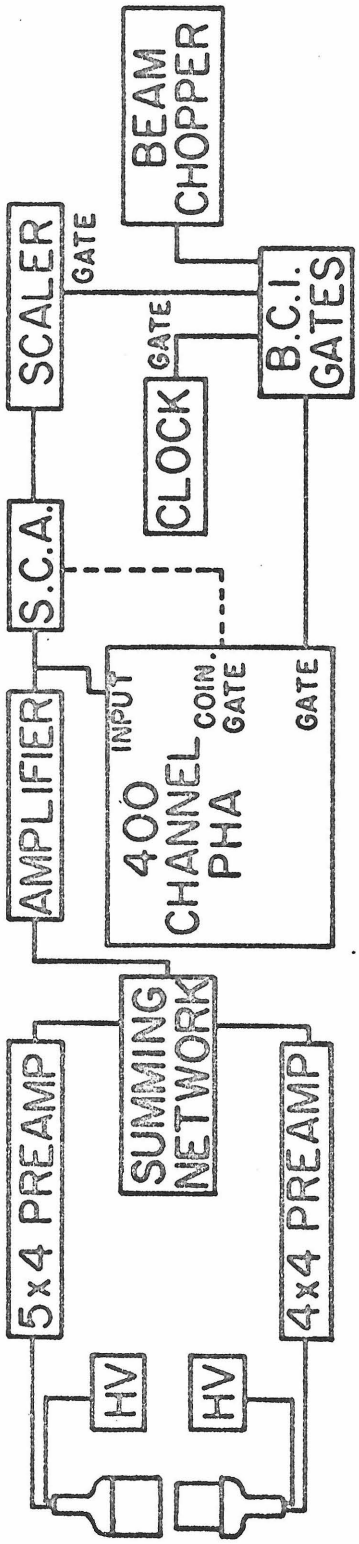
BEAM CHOPPER
SCALER
GATE
B.C.I. GATES
GATE
CLOCK
S.C.A.
AMPLIFIER
INPUT
400 CHANNEL PHA
COIN. GATE
GATE
SUMMING NETWORK
5x4 PREAMP
4x4 PREAMP
HV
HV

III. DETECTION EFFICIENCY FOR SINGLE GAMMA RAYS

A. NaI(Tl) Scintillation Detectors

A scintillation detection system consists basically of, 1) a gamma ray converter whose function is to generate electrons through the interaction of the incident gamma rays with the electrons and nuclei of the converting material, 2) a medium (ideally the converter) in which some portion of the ionization energy loss of the conversion electrons is radiated as visible light, and 3) a photomultiplier tube and associated electronics for detecting the light pulse. For the high gamma ray energies (> 1 MeV) under consideration here, the most important primary gamma ray interactions are through Compton and pair production events (Davisson, 1965). The magnitude of the Compton cross section per atom is proportional to the Z of the converting material, while the pair production cross section is proportional to Z^2. Thus high Z materials will enhance the pair production effect which dominates the total cross section at high energies. In addition to using high Z materials, a practical scintillator should possess several qualities including, 1) high usable light output (the crystal must be transparent to its own radiation, and this radiation must be of a wave length suitable for available photocathodes), 2) rapid decay of the light output pulse, 3) pulse height proportional to energy lost in the crystal (although inconvenient, a slight non-linearity could be tolerated for most applications), and 4) reasonable physical properties (ideally not degraded by exposure to atmosphere, fairly easy to grow crystals, easily shaped, etc.).

The use of thallium-activated sodium iodide was first suggested in 1948 (Hofstader). NaI(Tl) is a highly deliquescent material and, as such, is difficult to handle, but its high usable light output, fairly short decay time (0.25 μsec), fairly linear response, and high density (3.67 g/cc) have made it the most widely used gamma ray detector over a wide range of gamma energies (Neiler and Bell, 1965; Harshaw, 1962). Other inorganic, high Z, scintillating materials have been suggested which offer specific advantages over NaI(Tl); of some interest are CaI_2(Eu) and CsI(Tl). CaI_2(Eu) is denser (3.96 g/cc) than NaI and produces twice the light output of NaI(Tl), but it is extremely difficult to handle and has a decay constant of 0.55 μsec (Hofstader, O'Dell, and Schmidt, 1964). CsI(Tl) is considerably denser (4.51 g/cc) and very easy to handle (non-deliquescent), but the relative pulse height is only about a quarter of that of NaI(Tl) and the decay time is 1.1 μsec (Harshaw, 1962).

B. Calculated Efficiencies of NaI(Tl) Crystals

The number of primary interactions in a bare block of NaI can be accurately calculated using the known gamma ray attenuation coefficients for NaI (Grodstein, 1957), however the introduction of any scattering material other than the scintillator complicates the situation. The pulse height spectrum measured for a monochromatic gamma ray varies as an extremely complex function of experimental conditions. Crystal size is of crucial importance in determining to what extent secondary Compton gamma rays, electrons, bremsstrahlung, and annihilation quanta will interact further with the

crystal volume. In addition, the presence of scattering media (e.g., air, crystal can, etc.) in the vicinity will alter pulse height distributions. Great effort has been expended in experimental determinations of such spectral shapes under conditions selected to minimize confusion due to such absorber scatterings; frequently these studies are pursued in order to determine the photofraction for a given geometry. (The photofraction ϕ is defined as the fraction of the primary interactions which are totally absorbed, or equivalently, the ratio of the counts in the full energy peak to the total spectrum counts). Useful spectrum shape information, for various geometries, may be found in the literature (Heath, 1964; Harshaw, 1962; Leutz, Schulz, and Van Gelderen, 1966; Neiler and Bell, 1965). Several attempts at calculation of spectral shapes and photofractions of bare crystals exist in the literature (Zerby and Moran, 1961; Miller and Snow, 1961; Snyder, 1967); these calculations involve complex Monte Carlo programs in which the interaction histories of individual gamma rays are generated by a computer. Agreement between these "theoretical" or "idealized" shapes and the experimentally observed shapes is not good in the region of low pulse height, where the experimental shapes are sensitive to scattering events exterior to the crystal volume. Zerby and Moran (1961) pointed out that ideally the zero energy intercept of a spectrum will involve only singly-interacting, forward-scattered, Compton gamma rays, and as such, may be evaluated analytically. This analytic zero intercept concept has been used by various experimenters (Pearson, 1963; Parker, 1963; Larson, 1965), even though experimental shapes measured by these authors do not reproduce this

zero intercept, and are consistent with a nearly horizontal extrapolation of the low energy region (Pearson, 1963; Kavanaugh, 1956). In figure 5, discussed in section III.C, the zero energy intercept will be applied, for illustration, to one monochromatic gamma ray spectrum shape measured in the present geometry. The equation for calculation of this intercept is given later in this section.

Two philosophies can be followed with regard to the discrepancy between the analytic zero energy intercept concept and the more horizontal low energy pulse distribution which is experimentally observed. If one wishes to use theoretical interaction efficiencies, and concentrate attention only on the high energy region of a spectrum, then the use of the analytic intercept (or photofractions obtained in the most carefully controlled, minimal scattering, experimental geometries) would seem the most logical choice. If, however, one is concerned with application of the entire spectral shape (as in this experiment), one would be well advised to experimentally determine detection efficiencies for the precise geometry of interest since the events in the low pulse height region will, to some extent, arise from primary interactions exterior to the detector volume.

As a guide to interpretation of the experimentally determined detection efficiencies $\epsilon(E)$ given in the next section, detection efficiencies were calculated for several illustrative models.

The first determination completely ignored the presence of any absorbers and calculated the detection efficiency $\epsilon_0(E)$ for a bare NaI crystal.

$$\epsilon_0(E) = \frac{1}{2}\int_{\text{crystals}} \left\{1 - \exp\left[-\mu_1(E)\, x(\theta)\right]\right\} \sin\theta \, d\theta \qquad (7)$$

where $\mu_1(E)$ = attenuation coefficient of NaI (Grodstein, 1957) for gamma rays of energy E, and $x(\theta)$= path length of NaI at angle θ, where θ is measured relative to a z-axis passing through the centers of both crystals, giving cylindrical symmetry for the crystals.

The second determination of detection efficiency $\epsilon_-(E)$ considered the presence of absorbers, but assumed that conversion electrons, secondary Compton gammas, and bremsstrahlung from absorber interactions would not result in any interaction with the NaI.

$$\epsilon_-(E) = \frac{1}{4\pi}\int\int_{\text{crystals}} \exp\left[-\mu_2(E) y(\theta,\phi)\right] \left\{1 - \exp\left[-\mu_1(E)\, x(\theta)\right]\right\} \sin\theta \, d\theta \, d\phi \qquad (8)$$

where $y(\theta,\phi)\,\mu_2(E)$ represents a sum of the products of attenuation coefficient and path length in the Ta target backing, the pyrex target chamber, the Al crystal cans, and the packed reflector material surrounding the crystals. ϕ is an angle measured relative to a vertical axis.

Since the sum of the absorber thicknesses (excluding the Ta target blank which affects only half the solid angle subtended by the crystals) is only about 580 mg/cm^2, which is roughly the total path length of a 1.1 MeV electron (Berger and Seltzer, 1964), $\epsilon_-(E)$ will surely be inaccurate for high energy gamma rays. Also, some secondary Compton gammas will enter the crystals. The third determination of detection efficiency, $\epsilon_+(E)$, involved the assumption

that all absorber events produced interactions with the NaI, thereby contributing to the total efficiency.

$$\epsilon_+(E) = \frac{1}{4\pi} \int\int_{\text{crystals}} \left\{ 1 - \exp\left[-\mu_1(E)\, x(\theta) - \mu_2(E)\, y(\theta,\phi) \right] \right\} \sin\theta \, d\theta \, d\phi \tag{9}$$

The integration for $\epsilon_+(E)$ over only the 81% of 4π subtended by the crystals is open to some question. Certainly some absorber events in the 19% of 4π not subtended by the crystals will produce an interaction with the crystals; but at the same time, some absorber events counted by this integral will actually involve scattering outside the cone subtended by the crystals. To some degree, these effects will cancel, and in any case, $\epsilon_+(E)$ serves as an illustration of the effect absorber events can make on detection efficiencies.

The above integrals were programmed for numerical integration on the Caltech IBM 7094 computer by replacing the integrals with double summations over a (θ,ϕ) grid. Accuracy of these summations was checked by varying the grid size over a wide range and by comparison of selected cases with published tables for bare crystals (Wolicki *et al.*, 1956).

The absorber thicknesses for the Ta target blanks (0.25-mm) and the pyrex target chamber (1 mm) were known, and the thickness of the Al can (0.081 cm) was taken from specifications in the Harshaw catalog. The thickness of packed reflector for each crystal was measured by monitoring crystal response as the crystal was moved past a collimated slit source of gamma rays. The thickness of

absorber was measured as 0.28 cm for the 4" × 4" and 0.43 cm for the 5" × 4"; errors in these reflector thickness determinations should not exceed about 1 mm. The density assumed for the packed reflector was 0.5 g/cc, obtained as a rough estimate from data in the Harshaw catalog. Attentuation coefficients (Grodstein, 1957) for the pyrex and the oxide reflectors were taken as equal to those of Al (in units of cm^2/g), while tungsten (Z = 74) attentuation coefficients were used for tantalum (Z = 73), in units of cm^2/g.

Figure 4 shows the calculated curves discussed above. Uncertainties in the calculated curves arise from several sources. The rate of change of $\epsilon(E)$ with total distance to the NaI surface was 3.6%/mm (for the 4" × 4" crystal) and 3.0%/mm (for the 5" × 4" crystal). Error in this total distance would arise mainly from the reflector thickness measurements. Additional uncertainty arises from the attenuation coefficients themselves, an uncertainty of 5% in the NaI attenuation coefficient leads to an uncertainty of about 3.2% in $\epsilon_{4X4}(E)$ and 3.0% in $\epsilon_{5X4}(E)$. Grodstein (1957) estimates that uncertainties in her attentuation coefficient tables do not exceed 5%. Strictly speaking, photonuclear cross sections should also have been included in the attenuation coefficients, although this would have amounted to a very small correction. At 12 MeV, the NaI attenuation coefficient is about 9.5 barns/molecule. The total photonuclear cross section for ^{23}Na at 15 MeV is only ~ 4 mb (Wyckoff et al., 1965); for iodine, only the (γ,n) cross section has been measured, at 12 MeV $\sigma_{\gamma n} \sim 70$ mb; at 14 MeV, $\sigma_{\gamma n} \sim 190$ mb (Bramblett et al., 1966). Even if the (γ,p) cross section of ^{127}I were equal to the (γ,n) cross

FIGURE 4: Calculated Detection Efficiencies

Detection efficiencies calculated for the present geometry are illustrated in this figure. The three calculated curves involve different assumptions about the fate of secondary electrons and Compton gamma rays arising from scattering by absorbers. The central curve, $\epsilon_0(E)$, represents the efficiency calculated for a bare NaI crystal neglecting the presence of absorbers. The upper curve, $\epsilon_+(E)$ is calculated on the assumption that all electrons from absorber scatterings actually enter the volume of NaI, or equivalently, that all absorber events produce pulses and contribute to the efficiency. In the lower curve, $\epsilon_-(E)$, it is assumed that all such absorber electrons, and associated Compton-degenerated gamma rays, do not enter the detection volume of NaI. Note the depressed zero on the efficiency scale.

FIGURE 4

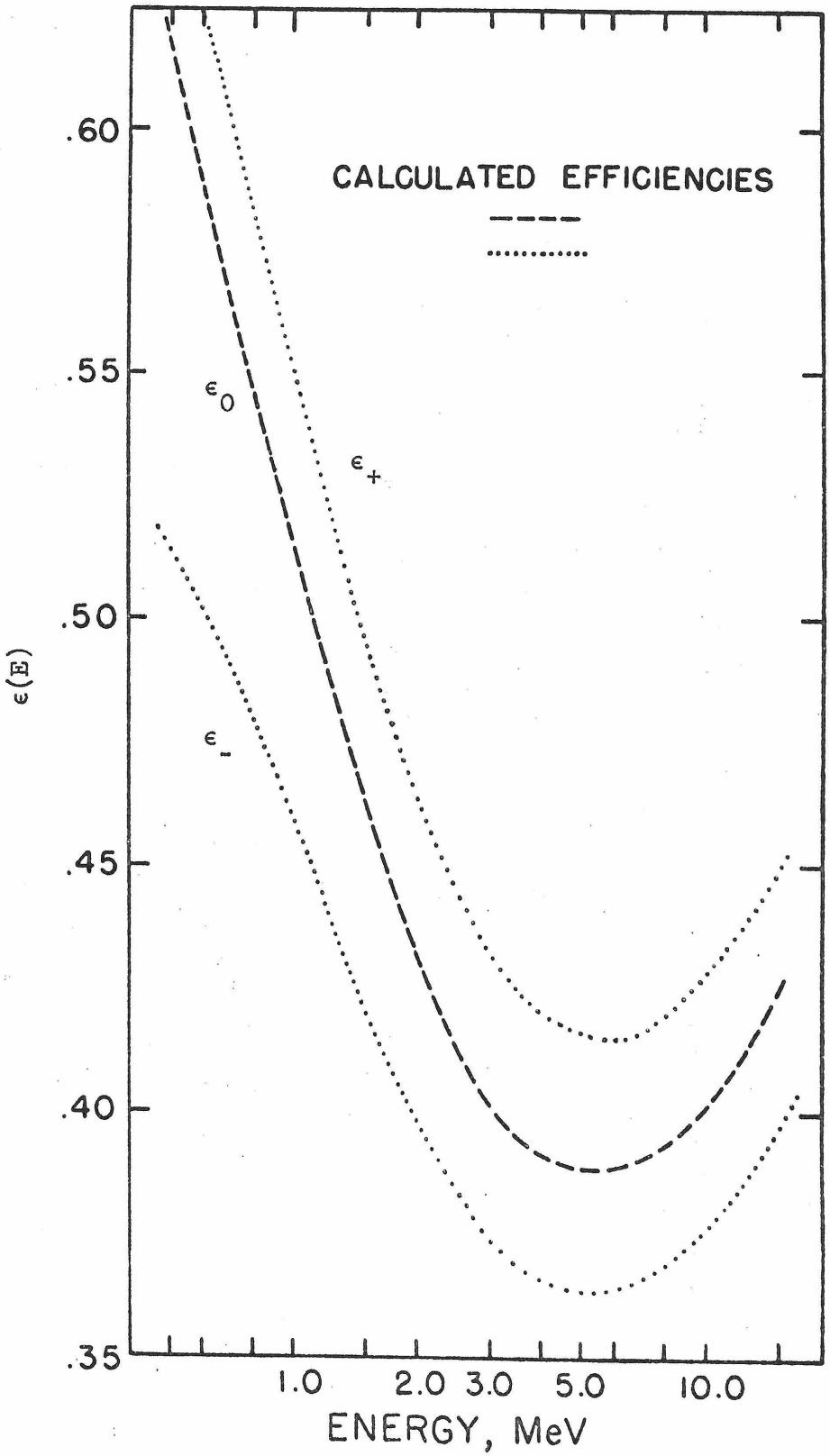
CALCULATED EFFICIENCIES
ϵ_0
ϵ_+
ϵ_-
$\epsilon(E)$
.60
.55
.50
.45
.40
.35
1.0
2.0
3.0
5.0
10.0
ENERGY, MeV

section, the photonuclear processes would contribute at most a 2% correction at 12 MeV, or 5% correction at 14 MeV, to the attenuation coefficient. In addition, the integration limits which should be imposed on the calculation of $\epsilon_+(E)$ were somewhat uncertain, as discussed previously.

It would be anticipated that at the highest energies under consideration, where very energetic Compton electrons and electron pairs were being produced in the absorbers, the $\epsilon_+(E)$ detection efficiency would be the best estimate of efficiency. At energies of 1-2 MeV, the ϵ_0 curve would probably be favored (since absorber interactions are mainly Compton events, the low energy Compton electrons may not enter the NaI, and the Compton gammas can be treated like the incident radiation in first approximation). At still lower energies, photoelectric events should make the ϵ_- curve the best estimate. The calculated curves, though, are primarily to be taken as indicative of the sensitivity of detection efficiency to the fate of secondary particles from absorber events; the ϵ_- and ϵ_+ curves differ from ϵ_0 by about 6.5% at 13 MeV.

While discussing efficiency integrals, it is convenient to give the form of the integral required for a calculation of the analytic zero intercept (Zerby and Moran, 1961). This integral was performed using basically the same techniques which were developed for evaluation of the integrals of equations 7, 8, and 9. This integral, as mentioned previously, is a theoretical prediction of the number of events N_0 in the zeroth energy channel of width ΔE; it is useful mainly for

cases in which absorber conversion events are nonexistent (or if contributions from these events are to be removed from the spectrum). If there are N gamma decays (and absorber effects are ignored):

$$N_0 = N \int_{\text{crystal}} \frac{d\Omega}{4\pi} \int_0^{x(\theta)} \Delta E \left(\frac{d\sigma}{dE}\right)_{E=E'} \left\{ \exp\left[-\mu_1(E)L\right] \right\} \left\{ \exp\left[-\mu_1(E)(x(\theta)-L)\right] \right\} N_e \, dL \tag{10}$$

where: $\left(\frac{d\sigma}{dE}\right)_{E'=E} = 2\pi r_0^2 m_e c^2/E^2$ is the differential cross section for scattering a photon of energy E into the energy interval dE at E', evaluated at $E = E'$ (Davisson, 1965).

$r_0 = e^2/m_e c^2$

m_e = electron rest mass

N_e = electron density in NaI = 9.43×10^{23} electrons/cc.

If f_0 is the fraction of the total number of spectrum counts in channel 0, equation 10 simplifies to:

$$f_0 = \frac{N_0}{N_i} = \frac{\Delta E}{2\epsilon_0(E)} \left(\frac{d\sigma}{dE}\right)_{E=E'} \int_{\text{crystals}} x(\theta) \exp\left[-\mu_1(E)\, x(\theta)\right] \sin\theta \, d\theta \tag{11}$$

Figure 5 shows the calculated analytic zero intercept for a nearly (96%) monochromatic spectrum of 6.14 MeV gamma rays for the present experimental geometry.

C. Experimental Detection Efficiencies

The preceding section has discussed the uncertainties encountered in using gamma ray efficiencies calculated, or measured, for certain "idealized" geometries. In the present geometry, these idealized (minimal absorber) geometries are not even remotely

FIGURE 5: Monochromatic 6.13 MeV Gamma Ray Spectrum

This figure shows the spectrum shape measured for nearly monochromatic (96%) 6.13 MeV gamma rays obtained from the $^{19}F(p,\alpha_1\gamma)^{16}O$ reaction at the 0.341 MeV resonance. The spectrum has been corrected for beam-induced, non-resonant, background as well as a beam-independent background. Details of the experimental efficiency determination using this spectrum are given in subsection III.C.2.

The low energy extrapolation used for the efficiency determination is shown on the figure, it is very nearly horizontal. The analytic zero intercept is also indicated (calculated from equation 11), together with the low energy extrapolation it would imply. Note that the analytic intercept falls well below the experimental points. It should be pointed out that the modified target holders used for this series of efficiency determinations did not present quite as much Ta absorber thickness as did the standard blanks. For the case in the figure the analytic intercept is about 60% of the experimental extrapolation used. A check of this same resonance on the standard backings gave an analytic intercept of about 50% of the experimental extrapolation.

Figure 7 gives two more monochromatic gamma spectra and comments about the zero analytic intercepts in those cases.

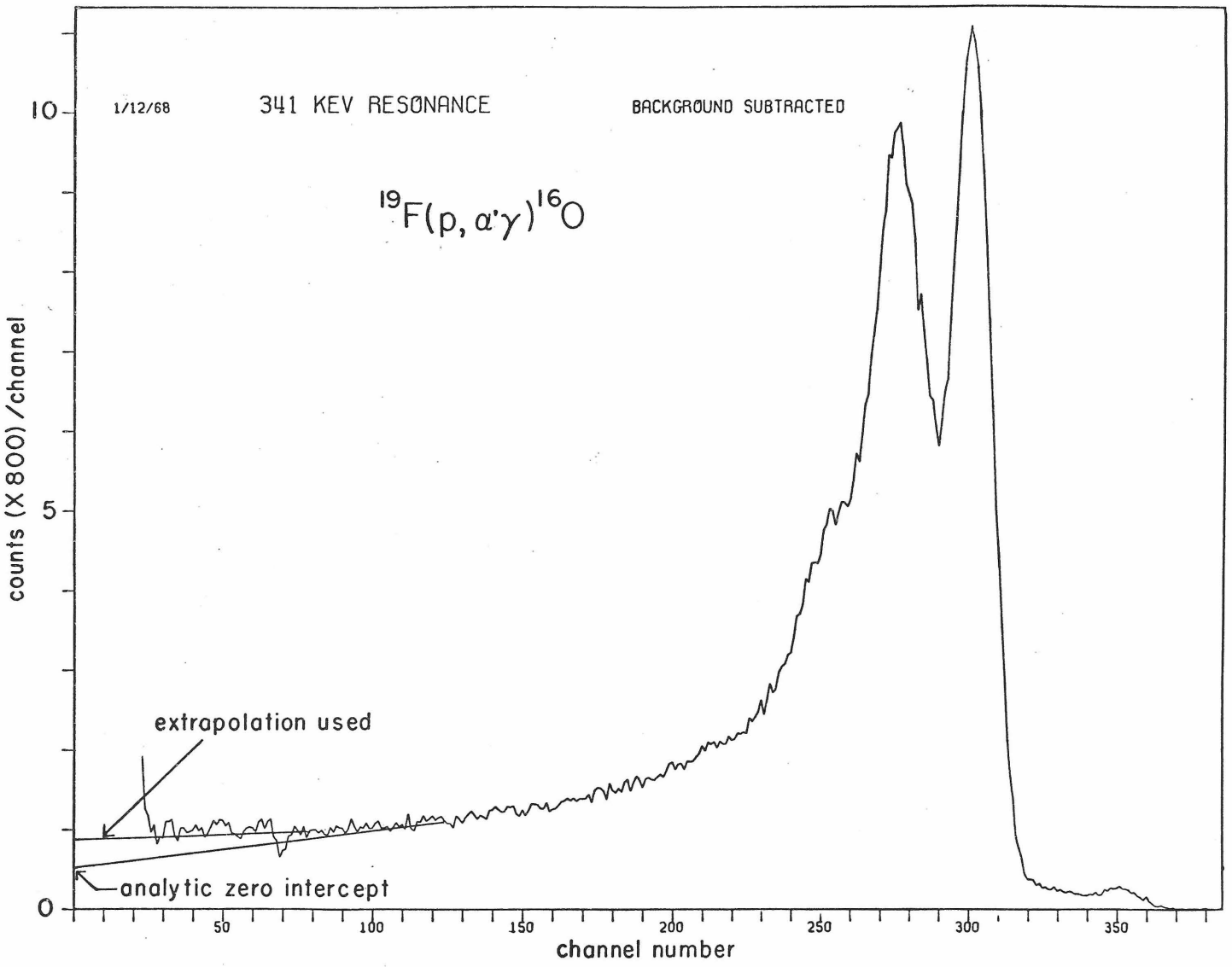
1/12/68
341 KEV RESONANCE
BACKGROUND SUBTRACTED
$^{19}F(p,\alpha\gamma)^{16}O$
counts (X 800) /channel
10
5
0
extrapolation used
analytic zero intercept
50
100
150
200
250
300
350
channel number

FIGURE 5

approached, and an experimental determination of the detection efficiency was made. In all such measurements, any changes in the actual experimental configuration (required by the particular measurement) were kept at a minimum. The low energy portion of the spectra was obtained by smooth extrapolation of the higher energy region. Four general types of absolute efficiency determinations were made: 1) calibrated sources, 2) $(p,\alpha'\gamma)$ reactions, 3) a (p,γ,β^+) reaction, and 4) the use of pure two gamma cascades involving a low-energy and a high-energy member.

1) Calibrations at gamma ray energies of 0.83, 0.9, and 1.84 MeV were obtained through the use of calibrated ^{88}Y and ^{54}Mn sources obtained from the Radiochemical Centre, England, and the Commissariat a l'Energie Atomique, France. Estimated standard deviations quoted on these sources were 2%. Accurate half-lives (1% or better) were taken from the work of Anspach et al. (1965). All spectra were corrected for room background effects.

The actual efficiency measurements were made with weak (0.1 μCi) sources which had been deposited on the standard 0.25-mm thick Ta target blanks. Solutions from which these sources were deposited were obtained from General Radioisotopes Processing Corporation (San Ramon, California). These weak sources were then standardized against the calibrated sources by observing, under identical detection conditions, the ratio of photopeak counts for the two sources; corrections for room background were applied.

From the ^{54}Mn source (electron capture followed by 0.835 MeV gamma ray), the efficiency for 0.83 MeV gamma rays was determined.

Using the shape of the ^{54}Mn spectrum, the contribution to the ^{88}Y spectrum (electron capture followed mainly by a cascade of 0.90 and 1.84 MeV gamma rays) from the 0.90 MeV gamma ray was peeled from the spectrum yielding a determination of the detection efficiency at energies of 0.9 and 1.84 MeV. Using the ratio of theoretical efficiencies, the efficiency obtained from the ^{54}Mn measurement at 0.83 MeV was scaled to yield an efficiency at 0.90 MeV; this result was then averaged with the 0.9 MeV efficiency from the ^{88}Y source. The averaged 0.90 MeV efficiency, and the 1.84 MeV efficiency are shown in figure 8.

2) Several $(p,\alpha'\gamma)$ reactions were used for efficiency calibrations at resonances for which essentially monochromatic gamma rays result. For these measurements, an Ortec surface barrier detector was mounted at the top of the pyrex target chamber behind a circular aperture whose diameter was measured with a traveling stage microscope. Ideally (if the α' group is isotropic), the detection efficiency for alphas involves only geometrical factors which can be measured accurately. Thus the unknown gamma ray detection efficiency could be related to an absolute count of alpha particles.

The ideal reaction for such a test would possess several desirable properties. Both the γ and α yields should be isotropic, or if not, their angular distribution parameters should be accurately known. The Q for the (p,α') reaction should be large, preferably several times the resonance energy; this places the α' group at considerably higher energy than the elastic protons. This serves to limit difficulties in interpretation of the α' peak due to a background

of proton pileup pulses from the intense elastic peak. As mentioned, the resonant gamma rays should be monochromatic. Three reactions satisfied these criteria to at least some extent, and are discussed below in order of their desirability.

The $^{19}F(p,\alpha'\gamma)^{16}O$ reaction at the $E_p = 0.341$ MeV resonance ($J^\pi = 1^+$) yields a nearly monochromatic (96%) 6.14 MeV gamma ray from the α_1 transition. The (p,α_1) reaction Q is 1.98 MeV and the yield is very nearly isotropic (Ajzenberg-Selove and Lauritsen, 1959). CaF_2 provided a convenient target. The (p,p') reaction is, at most, only weakly resonant, and in any case, would give gamma rays of energy below 0.2 MeV. If α_π transitions had been present to the pair-emitting ($J^\pi = 0^+$) state of ^{16}O at 6.06 MeV excitation energy, it would have been difficult to separate the α_1 and α_π groups. However, angular momentum considerations forbid the α_π transition, as well as excluding an α_0 resonance for the same reason. The (p,γ) reaction is not resonant at this energy. The gamma spectrum obtained from this measurement was shown in figure 5.

The $^{23}Na(p,\alpha_1\gamma)^{20}Ne$ reaction at the $E_p = 1.163$ MeV resonance ($J^\pi = 2^+$) yields 1.63 MeV gamma rays. The Q is 0.74 MeV and the yield should be isotropic. The angular distribution has not been measured for the α_1 group, but the measured isotropy for the resonant α_0 group (Stelson, 1954) implies s-wave proton capture and hence isotropy of all other reaction products as well. NaCl was used as a target. The (p,p') reaction (which yields a 0.44 MeV gamma ray) is resonant at this energy, but with only about 7% the strength of the (p,α_1) channel (Endt and Van der Leun, 1967). The (p,γ) reaction

is resonant also, but with less than 1% the strength of the (p,α_1) group (Endt and Van der Leun, 1967). The charged particle spectrum is shown in figure 6 and the gamma ray spectrum is given in figure 7a.

The $^{15}N(p,\alpha_1\gamma)^{12}C$ reaction at the $E_p = 0.898$ MeV resonance ($J^\pi = 2^-$) yields a monochromatic 4.43 MeV gamma ray; however the Q is only 0.53 MeV, and the yield is highly anisotropic (Kraus et al., 1953). The angular distribution parameters are not accurately known (20% uncertainty). KNO_3 (enriched to 61% ^{15}N) was used as a target. The (p,p') reaction is well below threshold, the (p,γ) reaction is not resonant, and the (p,α_0) reaction is forbidden by angular momentum considerations. The gamma spectrum recorded is shown in figure 7b.

For these measurements, the targets were evaporated on 10-20 $\mu g/cm^2$ carbon foils (obtained from Yissum Research Development Company, Jerusalem, Israel). None of the above resonances are near $^{12}C(p,\gamma)^{13}N$ resonances, and no gamma rays from the carbon foil were evident in the spectra. The standard solid Ta target backings were modified to allow the use of transmission targets; this was necessary to prevent intense elastic scattering of the incident beam from the solid backings into the particle detector. In addition to the gamma ray instrumentation described in Part II, a standard preamp-amplifier system was used for the solid state detector. A second RIDL 400 channel PHA was employed to record the charged particle spectra. The two analyzers were gated on and off together, but coincidences were not required. Gamma ray spectra were taken on and off the resonance, and combined with the beam-independent background to yield a spectrum characteristic of the resonance. The procedure

FIGURE 6: Charged Particle Detector Spectrum

A charged particle spectrum, in the vicinity of the α_1 peak is shown for the $^{23}Na(p,\alpha_1\gamma)^{20}Ne$ reaction at the E_p = 1.163 MeV resonance. This spectrum is typical of those obtained during gamma detection efficiency determinations discussed in the text. The high energy edge of the intense elastic scattering peak is evident at about channel number 160. The background under the α_1 peak is due to proton pileup and possibly some scattered, higher-energy α_0 particles arising from (p,α_0) reactions on either the sodium or the chlorine in the target.

FIGURE 6.

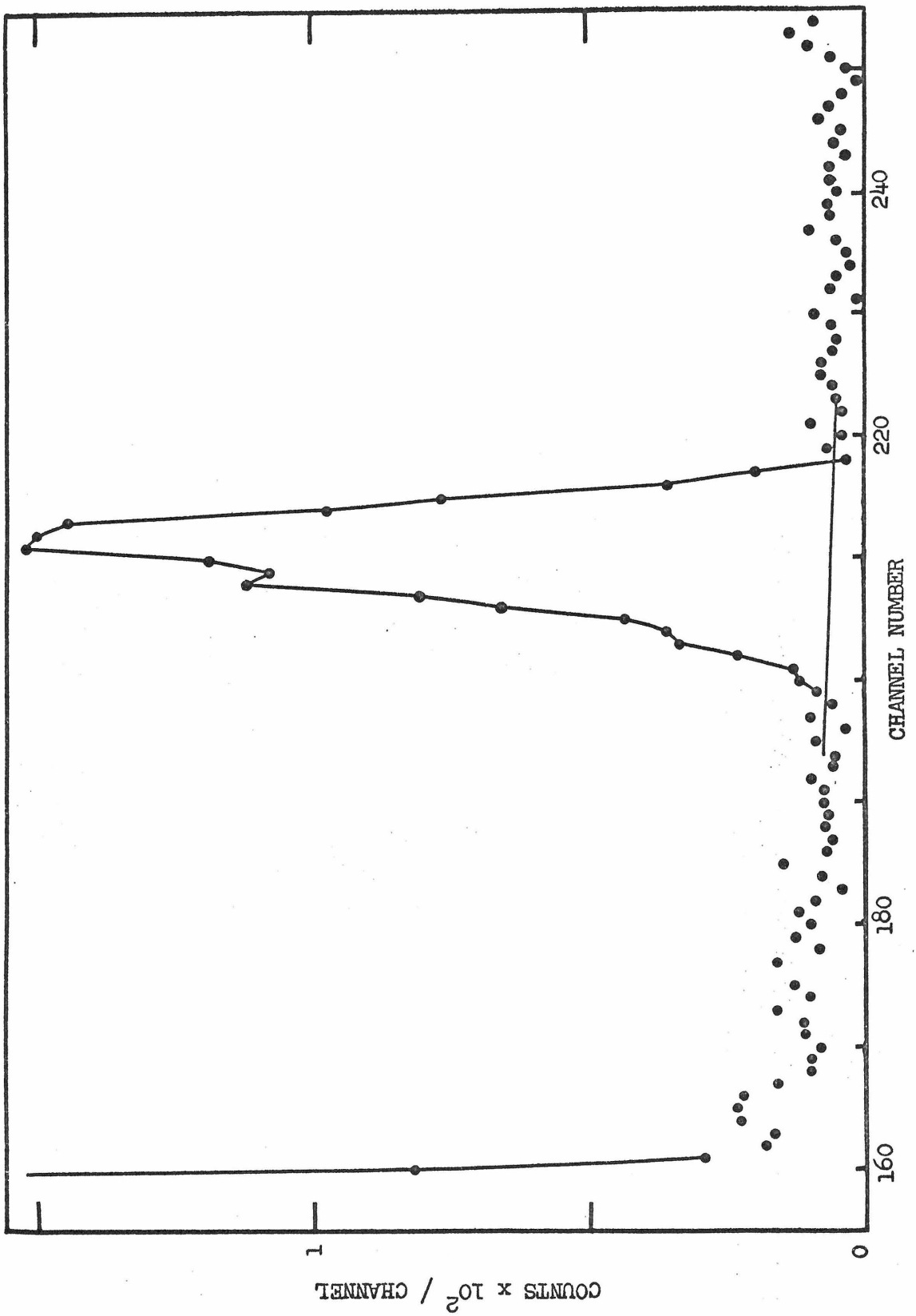

FIGURE 7: Monochromatic Gamma Ray Spectra

Monochromatic gamma ray spectra of energy 1.63 and 4.43 MeV are shown in this figure, obtained from the $^{23}Na(p,\alpha_1\gamma)^{20}Ne$ and $^{15}N(p,\alpha_1\gamma)^{12}C$ reactions, respectively. These spectra have been corrected for both beam-induced background, and beam-independent background. Figure 5 showed another monochromatic spectrum also measured for the present geometry. Details of the measurements associated with these spectra are discussed in the text.

The analytic zero intercept (see equations 10 and 11) was calculated for these curves. For the 1.63 MeV shape, the analytic intercept approximately corresponded to the low energy extrapolation used. For the 4.43 MeV spectrum, the analytic zero intercept was 75% of the zero intercept used on the figure. Figure 5 explicitly showed the zero analytic intercept calculated for the 6.14 MeV spectrum shape; in that case, the analytic intercept was 60% of the experimentally-guided zero intercept. Thus external conversion events are playing a greater role in distorting the "theoretical" spectra (i.e., for a bare crystal) as energy is increased.

FIGURE 7

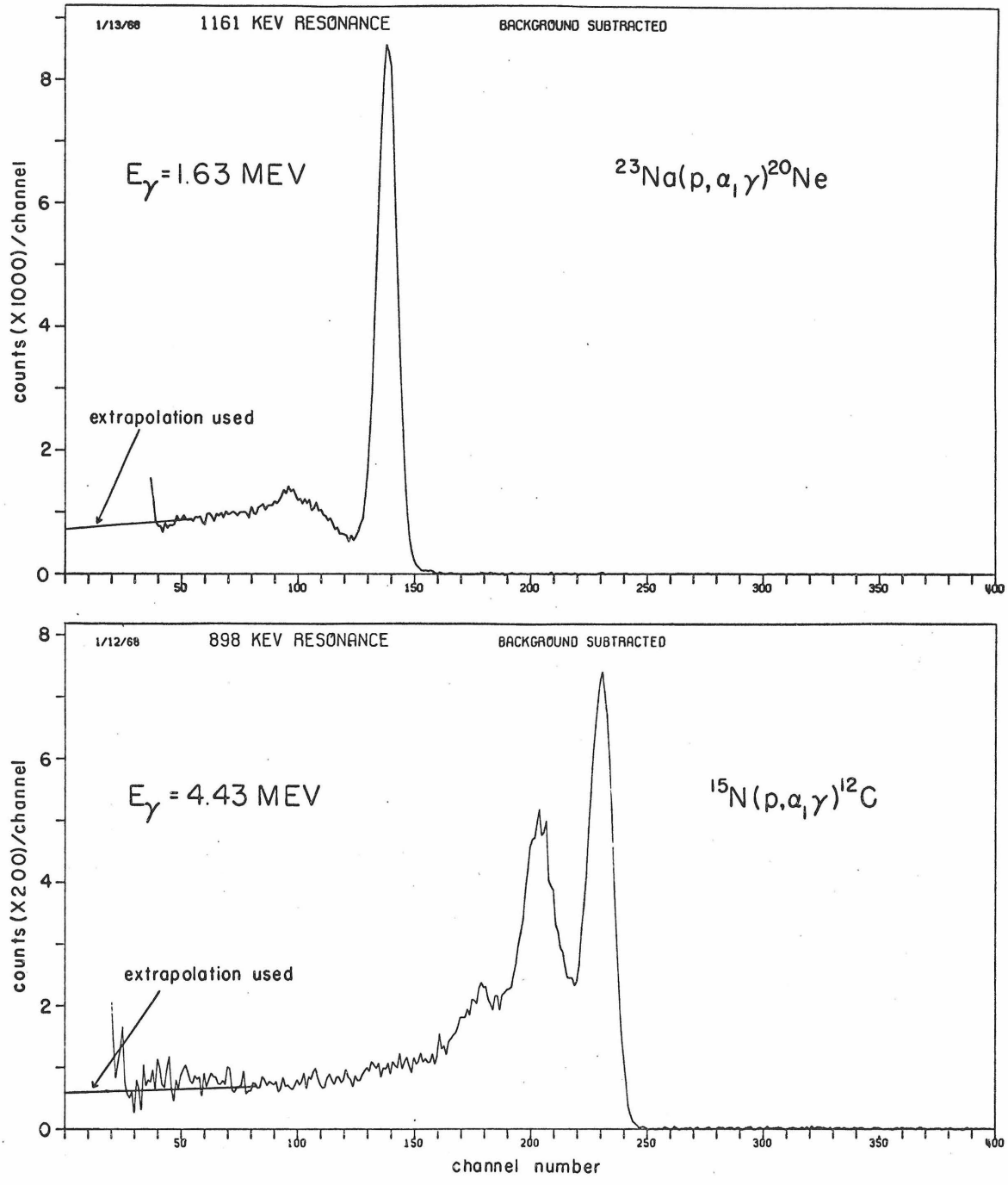
1/13/68
1161 KEV RESONANCE
BACKGROUND SUBTRACTED
E_γ = 1.63 MEV
$^{23}Na(p,\alpha_1\gamma)^{20}Ne$
extrapolation used
counts (X1000)/channel
1/12/68
898 KEV RESONANCE
BACKGROUND SUBTRACTED
E_γ = 4.43 MEV
$^{15}N(p,\alpha_1\gamma)^{12}C$
extrapolation used
counts (X200)/channel
channel number

followed was identical to that used for the $^{27}Al(p,\gamma)^{28}Si$ and $^{24}Mg(\alpha,\gamma)^{28}Si$ resonance spectra, and will be discussed in Appendix II. Angular distribution corrections to the α detection efficiency were applied only for the $^{15}N(p,\alpha_1\gamma)^{12}C$ case (the total correction was 28%). Details of the effect of an anisotropic gamma ray angular distribution on the gamma ray detection efficiency are discussed in Section III.D (these corrections were needed only for the $^{15}N(p,\alpha_1\gamma)^{12}C$ case and amounted to 4%). The efficiencies determined from these measurements are shown in figure 8.

c) The reaction $^{29}Si(p,\gamma)^{30}P(\beta^+)^{30}Si$ was used to obtain a measurement of the gamma ray detection efficiency at 5.3 MeV by a method substantially different from case b. The general technique involved 4π β-counting of the radioactive decay of the target after measurement of the gamma ray yield. In this way, the unknown detection efficiency for gamma rays was related to the absolutely measured number of β^+ decays. The half life of ^{30}P is 2.5 minutes, which allowed adequate time for transfer of the target out of the vacuum system into the 4π counter. Most (87%) of the decays of the resonance used (at 0.416 MeV) proceed directly to the 0.67 first excited state of ^{30}P; only about 1.6% of the decays populate this state by other cascades (Endt and Van der Leun, 1967). By peeling the 0.67 MeV gamma ray spectrum from the total spectrum, the detection efficiency was obtained for 5.3 MeV gamma rays. (Contributions to the gamma ray spectrum from positron annihilation were also removed, of course).

The 4π β-counter consisted of two cylinders (each 5 cm

diameter × 3 cm long) of Pilot B plastic scintillator, covered with 0.037 mm Al foil (0.0103 g/cm^2). At normal incidence, this foil thickness is roughly the total pathlength of a 0.07 MeV electron. The β^+ decay is a Gamow-Teller allowed transition with the very high end point energy of 3.24 MeV; thus the effect of the foils on the total number of recorded counts was small. The two cylinders of scintillator were separated by a spacer 0.25 mm thick. The targets were isotopically enriched, elemental silicon (95% ^{29}Si) evaporated on 200 μg/cm^2 copper foils. (Mr. David Gordan provided these targets.) During bombardment, these transmission foils were backed by tantalum to reproduce the "standard" geometry as closely as possible. The beam current was monitored as a function of time by a system built by Dr. Dale Hebbard and Mr. Harold Spinka. From this current vs. time information, the known transfer time into the counting system, and a measurement of the counting time in the 4π counter, the ratio of the total number of radiative captures to the number of β^+ decays occurring in the 4π counter could be easily derived.

The efficiency of the β^+ counter was determined by numerically folding the allowed-transition spectrum, compiled from published tables (Fano, 1952), with an electron range $R(E_e)$ inferred from calculated total pathlength tables (Berger and Seltzer, 1964). Such pathlength tables are calculated on the Continuous Slowing Down Approximation, abbreviated by CSDA. Electron range, however, is not easily calculated due to the "tortuous" path of an electron, therefore, this numerical folding was done for both $R(E_e)$ = CSDA value and $R(E_e) = \frac{1}{2}$ CSDA value, yielding 0.942 and 0.911, respectively,

for the probability that an electron would enter the scintillator. Katz and Penfold (1952) defined a "practical range" $R_p(E_e)$ for homogeneous electron beams which is about 75% of the CSDA values; however the half-range (the range at which an incident beam is attenuated to half its initial intensity) is somewhat smaller than R_p. Experimental half-ranges (Chang et al., 1953; Marshall and Wood, 1937) are (0.5 ± 0.1) of the CSDA value. Thus using the $\frac{1}{2}$ CSDA value is probably reasonable; nevertheless an uncertainty of 0.03 was attached to the adopted efficiency of 0.91 for the β-counter.

It might seem that the gamma ray detection probability for the scintillators (44% for the co-linear annihilation quanta) would have added to this efficiency. However, the beam independent background in the Pilot B scintillators was of sufficient magnitude that the low energy region (< 0.5 MeV) of the β^+ spectrum was treated as a smooth extrapolation to 0 counts at channel 0, ignoring the occurrence of pulses resulting from a positron stopping in the foil when a pulse was nevertheless produced by the annihilation quanta.

The value obtained for ϵ (5.3 MeV) is shown in figure 8. Small corrections have been applied for two effects. A 2% correction was applied for the measured gamma ray angular distribution (Van der Leun and Endt, 1958). A weak yield was detected from the $^{12}C(p,\gamma)^{13}N(\beta^+)^{13}C$ resonance at 0.46 MeV, correction to the observed number of β^+ counts in the plastic scintillators was less than 1%.

d) Three resonances at high excitation energy, which decay predominantly by two-gamma cascades, were used to obtain gamma

ray efficiency information. The spectrum and efficiency for the lower energy member of the cascade were already known from the work described above; thus the efficiency for the higher energy member could be obtained relative to the previously measured efficiency for the lower energy member.

For the case of a 100% cascade of gammas γ_A and γ_B, $E_{\gamma_B} > E_{\gamma_A}$, the number of interactions due to only γ_A interacting is just

$$N_i(\gamma_A \text{ only}) = \epsilon(\gamma_A)(1 - \epsilon(\gamma_B))N_d \qquad (12)$$

where N_d is the total number of disintegrations of the level. The total number of counts excluding the "γ_A only" piece is

$$N_i(\gamma_B \text{ interactions}) = \epsilon(\gamma_B)N_B \qquad (13)$$

The ratio of these two quantities allows the determination of $\epsilon(\gamma_B)$ in terms of $\epsilon(\gamma_A)$. For the low energy γ_A, the efficiency had been previously measured by cases a, b, or c discussed earlier.

The $^{11}B(p,\gamma)^{12}C$ reaction at the 0.163 MeV resonance (16.1 MeV excitation energy) gave a very nearly pure cascade (96%) through the 4.43 first excited state of ^{12}C (Ajzenberg-Selove and Lauritsen, 1959). The spectral shape and efficiency for the 4.43 MeV gamma ray was known from the work described above for the $^{15}N(p,\alpha_1\gamma)^{12}C$ reaction, which excites the same ^{12}C state. In addition, two resonances in the $^{27}Al(p,\gamma)^{28}Si$ reaction at 0.992 and 1.388 MeV were used (excitation energies 12.54 and 12.92 MeV, respectively); these are predominantly (78% and 90%, respectively) γ_1 cascades through

the 1.78 MeV first excited state of ^{28}Si (Boydell, 1967; Azuma et al., 1966). The photofraction measured for the 1.63 MeV gamma ray from the $^{23}Na(p,\alpha_1\gamma)^{20}Ne$ reaction was corrected slightly to give a photofraction for the 1.78 MeV radiation in question; ϕ (1.78 MeV) = 0.43 was obtained. (As a first approximation, $\phi \propto 1/\sqrt{E}$.) In all cases, resonance spectra were corrected for beam-induced non-resonant background and beam-independent background by the methods of Appendix II. No angular distribution corrections were required for the first two cases (Grant et al., 1954; Antoufiev et al, 1964); angular distributions have not been measured for the third case.

These experimentally determined efficiencies are collected in figure 8, which also includes the three calculated efficiency curves ϵ_0, ϵ_+, and ϵ_- of figure 4. The experimentally determined efficiency adopted for this geometry is the solid curve; at 13 MeV it is 10% above the calculated ϵ_+ curve. In the light of the uncertainties in the calculated curves, discussed in the previous section, this difference is not regarded as serious.

Uncertainties in the experimental efficiency curve are estimated as 5% for the lower energies and 8% at the higher energies. For a γ_0 transition, the error in detection efficiency is just the error in $\epsilon(\gamma_0)$, or 8%. However, as will be shown in detail in Part IV, for multistage cascades, the uncertainty in total detection efficiency is considerably less than that obtained from a simple combination of errors in the $\epsilon(E)$ for each member of the cascade.

FIGURE 8: Experimental Gamma Ray Detection Efficiencies

The gamma ray detection efficiencies determined experimentally for nine energies are shown in this figure. The solid curve represents the detection efficiency adopted for this geometry; it is a curve following the general shape of the calculated efficiencies, and is discussed further in the text. The calculated efficiencies have been discussed in section III.B. The experimental points have been determined by a variety of techniques discussed in the text. The numbered points are from:

1) ^{54}Mn and ^{88}Y sources
2) The $^{23}Na(p,\alpha_1\gamma)^{20}Ne$ reaction
3) ^{88}Y source
4) The $^{15}N(p,\alpha_1\gamma)^{12}C$ reaction
5) The $^{29}Si(p,\gamma)^{30}P(\beta^+)^{30}Si$ reaction
6) The $^{19}F(p,\alpha'\gamma)^{16}O$ reaction
7) The $^{27}Al(p,\gamma)^{28}Si$ reaction
8) The $^{27}Al(p,\gamma)^{28}Si$ reaction
9) The $^{11}B(p,\gamma)^{12}C$ reaction

FIGURE 8

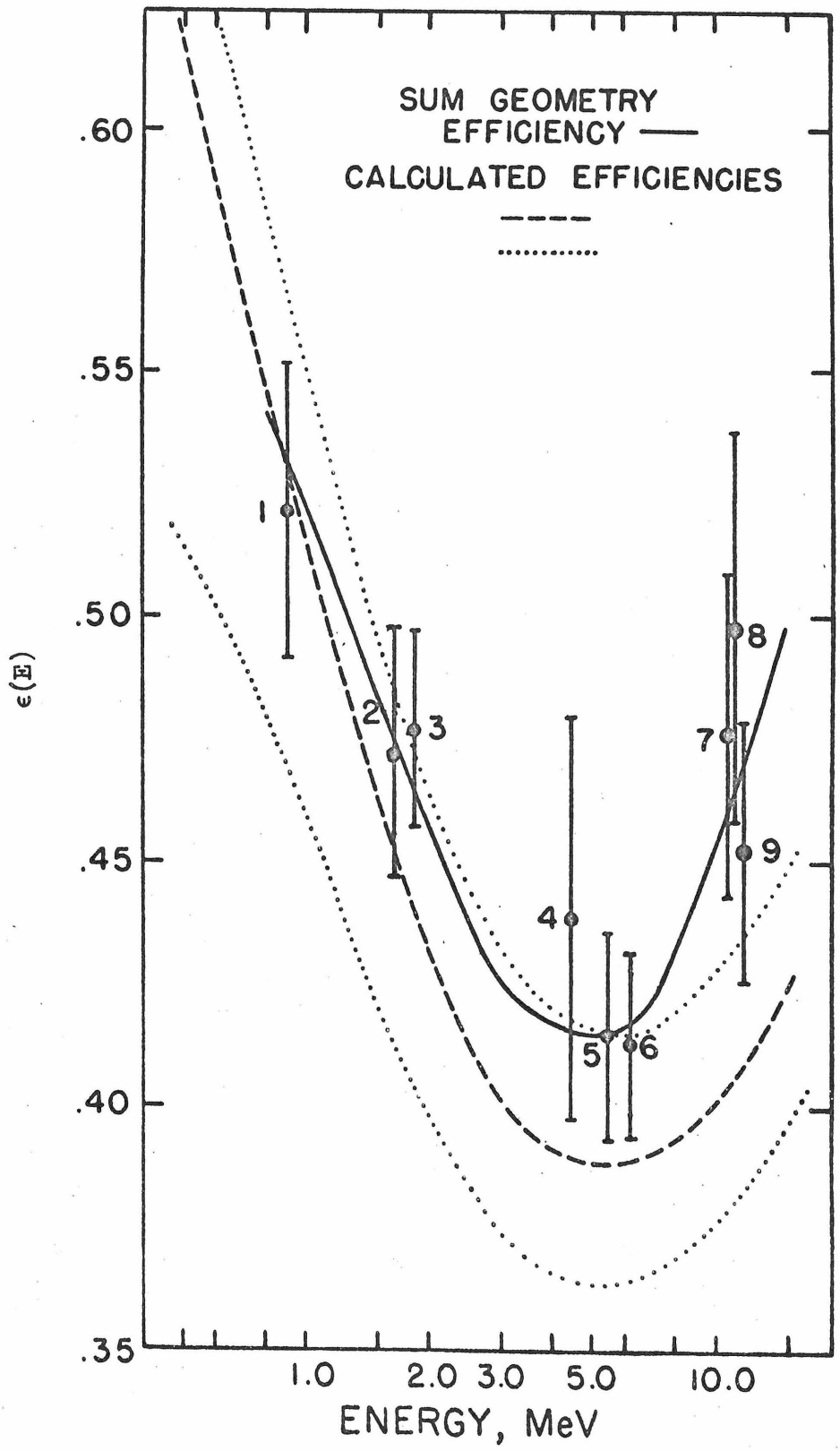
SUM GEOMETRY
EFFICIENCY ——
CALCULATED EFFICIENCIES
- - - -
.....
.60
.55
.50
.45
.40
.35
ε(E)
1
2
3
4
5
6
7
8
9
1.0
2.0
3.0
5.0
10.0
ENERGY, MeV

D. Angular Distribution Attenuation Coefficients

Any detector subtending a finite solid angle will reduce the observed anisotropy of an angular distribution and for the very large solid angle geometry of the present experimental detector configuration, angular distributions are largely averaged out. This is expressed analytically in the following way: if an angular distribution having the true form $\sum_i a_i P_i(\cos\theta)$ is measured by the crystals, an angular distribution weakened to $\sum_i Q_i a_i P_i(\cos\theta)$ will result, where $Q_{i>0} < 1$. This result was first shown by Rose (1953) for an axially symmetric detector; the Q_i's are given by

$$Q_i(E) = \frac{1}{\epsilon_0(E)} \frac{1}{2} \int_{\text{crystals}} P_i(\cos\theta) \left\{1 - \exp\left[-\mu_1(E)\, x(\theta)\right]\right\} \sin\theta \, d\theta \, . \tag{14}$$

From the definition, it is evident that $Q_0 = 1$. The factors, $Q_i(E)$ are approximately energy-independent; and for the present application for which they represent a small correction factor, the energy dependence will be ignored. Numerical evaluation of the above integral yielded $Q_2 = 0.29$ and $Q_4 = -0.060$ for the 4" × 4" NaI crystal; for the 5" × 4" crystal, $Q_2 = 0.25$ and $Q_4 = -0.075$. The inclusion of absorber effects in equation 14 would result only in "second order" corrections, and no attempt has been made to do this. (Since the effect of the absorbers is not axially symmetric, this would not be a trivial addition.)

The detection efficiencies discussed thus far have referred to isotropic radiation, i.e., where $a_{i>0} = 0$; this detection efficiency is

modified due to angular distributions to:

$$\frac{\epsilon(E)}{\epsilon_{iso}(E)} = \sum_{i \text{ even}} a_i Q_i \left[\frac{(-)^{i/2}(i)!}{2^i((i/2)!)^2} \right] \qquad (15)$$

where $\epsilon_{iso}(E)$ refers to the detection efficiency for isotropic radiation. Equation 15 assumes $a_0 = 1$, for convenience. The square bracket in equation 15 is $P_i(0)$ for even i; $P_i(0) = 0$ for odd i. The discussion thus far has dealt only with angular distributions for single gamma rays; if an angular correlation between two gamma rays were involved (involving simultaneous detection of two gammas), the Q_i's would appear squared (Rose, 1953). Powers ≥ 2 of the Q_i are completely negligible with the small Q_i's of the present geometry.

The many initial magnetic substates in the $^{27}Al + p$ reaction tend to produce weak angular distributions. For the $^{27}Al(p,\gamma)^{28}Si$ reaction, a survey of angular distributions measured for γ_1 transitions (Antoufiev et al., 1964) showed angular distribution corrections to $\epsilon(\gamma_1)$ to be typically $\leq 3\%$. Throughout the $^{27}Al(p,\gamma)^{28}Si$ analysis, angular distribution effects on the resonance yield measurements were therefore neglected.

Angular distributions for the $^{24}Mg + \alpha$ reaction (with a much lower number of initial magnetic substates) are not always negligible, and corrections up to 10% were applied for some resonances. For the $^{24}Mg + \alpha$ resonances for which angular distribution information was not available in the literature, an additional uncertainty of 10% has been included.

IV. DETERMINATION OF THE NUMBER OF RADIATIVE CAPTURES

Part III discussed in detail the detection efficiency determined experimentally for monochromatic gamma rays. For γ_0 transitions, such detection efficiencies would be all that would be required for determination of the number of radiative captures N_γ. However, γ_0 transitions are not the dominant mode of de-excitation of many of the resonance levels and methods had to be devised to handle more complicated cascades.

As discussed in the introduction, in order to determine the resonance strength, the total number of radiative captures N_γ must be determined. Two basic methods for determining N_γ from resonance spectra were used. (Appendix II will discuss how on-resonance, off-resonance, and room-background spectra were combined to obtain a spectrum for a given resonance.) On the stronger $^{27}Al(p,\gamma)^{28}Si$ resonances, a procedure utilizing the total number of interactions with the crystals, N_i, yielded the most accurate results. For this procedure $N_\gamma = N_i/\epsilon_t$ where ϵ_t is the total detection efficiency for a given resonance.

For other cases, such as the weaker $^{27}Al(p,\gamma)^{28}Si$ resonances and the $^{24}Mg(\alpha,\gamma)^{28}Si$ resonances, a method using the partial detection efficiency $\eta(f)$ was used; for this method $N_\gamma = N_i'(f)/\eta(f)$, where $N_i'(f)$ is the number of interactions yielding pulses larger than a fraction f of the full energy peak (above a fraction f of the excitation energy E_x of the resonance level), and $\eta(f)$ is the probability of an interaction yielding a pulse above fE_x.

A. Total Detection Efficiency

For a cascade characterized by branching ratios β_i, (where $\sum_i \beta_i = 1$), the total detection efficiency is

$$\epsilon_t = \sum_i \beta_i \left\{ 1 - \prod_{j=1}^{n_i} [1 - \epsilon(E_{ji})] \right\} \qquad (16)$$

where n_i is the number of members in the i^{th} cascade, $\epsilon(E_{ji})$ is the detection efficiency for a monochromatic gamma ray of energy E_{ji} and E_{ji} is the energy of the j^{th} member of the i^{th} cascade.

For many of the resonances studied here, the branching ratios were available in the literature (Endt and Van der Leun, 1967; Boydell, 1967; Azuma et al., 1966; Gibson et al., 1968); however, as mentioned in the introduction, the value of ϵ_t is not a strong function of the β_i's for this detector geometry. Errors in β_i such that the resonance strength is incorrectly shared between competing cascades of the same type (i.e., both two-gamma cascades) yield very small uncertainties in ϵ_t. For example, for a pure γ_1 cascade, from a resonance level at an excitation energy of 12.5 MeV, equation 16 gives: $\epsilon_t = \epsilon(1.78\ \text{MeV}) + \epsilon(10.7\ \text{MeV}) - \epsilon(1.78\ \text{MeV})\epsilon(10.7\ \text{MeV}) = 0.713$, where the $\epsilon(E)$ are taken from the solid curve of figure 8. For a cascade which splits the excitation energy evenly, we have $\epsilon_t = 2\epsilon(6.25\ \text{MeV}) - \epsilon(6.25\ \text{MeV})^2 = 0.660$. Thus, if 10% of the total gamma strength is assigned to a γ_1 transition, when it should have been assigned to the 6.25 + 6.25 MeV cascade, the overall error in ϵ_t is only $\approx 0.0053/0.7 = 0.8\%$.

A slightly more serious error may arise from incorrect

branching ratios among different types of cascades, e.g., two-gamma and three-gamma cascades. A typical three-gamma cascade from a 12.5 MeV level might be $7.89 + 2.83 + 1.78$ (corresponding to the γ_2 transition to the 4.61 MeV state of ^{28}Si); the efficiency for this cascade is 0.827. An error in which 10% of the total gamma strength is incorrectly assigned to a γ_1 transition, where it should have been assigned to the above γ_2 transition, leads to an overall error of only 1.5%.

Additional uncertainty in ϵ_t arises from the experimentally determined single gamma detection efficiencies $\epsilon(E)$. The most important monochromatic gamma ray efficiencies in the present investigation, in terms of frequency of use, are those for the γ_1 transition to the 1.78 MeV state and the subsequent de-excitation of this state by a 1.78 MeV gamma ray. Section III.C discussed the uncertainties in experimental detection efficiency and suggested about 5% at lower energies and 8% at higher energies. For a pure γ_1 transition, equation 16 demonstrates that in the least favorable case in which the errors contributed by $\epsilon(\gamma_1)$ and ϵ(1.78 MeV) add directly, the error in ϵ_t is only 4.5%.

This reduction of the uncertainty in ϵ_t for multistage cascades, due to uncertainty in $\epsilon(E)$, can be demonstrated in general from equation 16. For this demonstration, assume that $\epsilon(E)$ is approximately constant with energy. For a pure n-stage cascade, $\epsilon_t = 1 - (1 - \epsilon)^n$ and

$$\frac{\Delta\epsilon_t}{\epsilon_t} = \frac{n(1 - \epsilon)^{n-1}}{1 - (1-\epsilon)^n} \Delta\epsilon \quad . \tag{17}$$

If $\epsilon \approx 0$, $\Delta\epsilon_t/\epsilon_t \approx \Delta\epsilon/\epsilon$; but if $\epsilon \approx 1$, $\Delta\epsilon_t/\epsilon_t \approx n(1-\epsilon)^{n-1}\Delta\epsilon/\epsilon$ which is a rapidly decreasing function of n. Even for the present detector geometry with $\epsilon \approx 0.5$, the benefits of this error reduction are applicable.

B. Determination of N_i

In order to make use of ϵ_t, the total number of interactions, N_i, with the NaI crystals had to be known. This implies that all pulses in the spectrum, back to the zeroth channel, must be summed. However, only for the very strongest (p,γ) resonances were the lowest channels statistically significant; i.e., background and electronic noise corrections to the spectrum were much greater than the resonance contribution in the lowest channels. Thus an extrapolation procedure was required to estimate the counts in the lower channels for $^{27}Al(p,\gamma)^{28}Si$ resonances. $^{24}Mg(\alpha,\gamma)^{28}Si$ resonances were analyzed by the partial detection efficiency method of the next section.

The accuracy of such extrapolation procedures is improved by using such large detectors in the nearly-4π geometry; this greatly enhances the probability that more than one member of a cascade, or a secondary Compton gamma ray, will interact with the NaI. This has the effect of pushing a larger proportion of pulses into the high energy region of the pulse height spectrum, thereby reducing the importance of the low energy region. On the stronger resonances, the spectra were typically free of distortion by noise and background back to a pulse height of approximately 1 MeV, for proton energies < 2 MeV; in most cases, the photopeak from the 1.78 MeV first excited state of

^{28}Si also was clearly discernible. A schematic resonance spectrum is shown in figure 9. The extrapolation procedure chosen to obtain the total number of events in the pulse height spectrum, N_i, was as follows: the region above the 1.78 MeV photopeak (region A in figure 9) was summed, region B was estimated by extrapolating the plateau above the 1.78 MeV peak down to the zero energy channel, region C was summed, and region D, the remainder of the 1.78 MeV spectrum, was estimated from a previously determined photofraction for gamma rays of this energy. Resonant inelastic scattering to levels of ^{27}Al above ~ 1.5 MeV excitation energy would invalidate this procedure by introducing peaks in the resonance spectra not related to the (p,γ) reaction. However, this extrapolation procedure was not used above 2.1 MeV proton bombarding energy, which avoids any complications from inelastic scattering to the 2.21 MeV state in ^{27}Al. Another complication in the application of this method would be the presence of resonance transitions with energy below 1.78 MeV. Such transitions are extremely rare, however. The only resonance, out of the many for which branching ratios are available in the literature, with strong (44%) transitions of $E_\gamma < 1.78$ MeV, is the 1.118 MeV resonance in the ^{27}Al(p,γ)^{28}Si reaction. At this resonance only, corrections were applied for the presence of these low-lying transitions.

Considerable uncertainty is involved in estimating the photofraction for the 1.78 MeV spectrum which should be used in the above procedure. Although figure 9 suggests that the contribution of multiple interactions and single high energy interactions yields a flat plateau under the 1.78 MeV photopeak, this is not strictly correct. The line

FIGURE 9: Spectrum Extrapolation Procedure

This figure illustrates schematically the extrapolation procedure for gamma spectra. The spectral shape has been distorted for purposes of illustration. For the 0.992 MeV $^{27}Al(p,\gamma)^{28}Si$ resonance, for example, the distribution of counts in the four regions is: A - 64.5%, B - 8.5%, C - 12.5%, D - 14.5%.

FIGURE 9

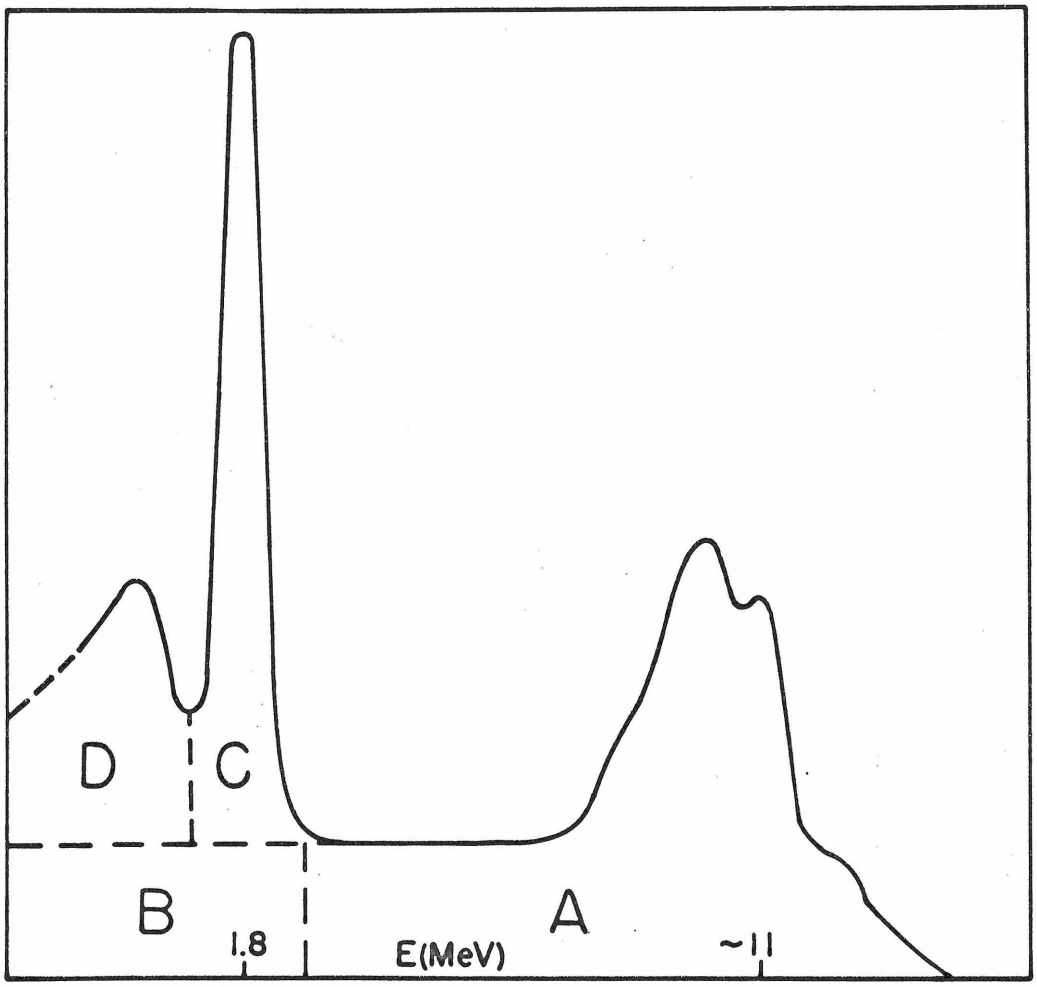

shapes measured for monochromatic gamma rays (figures 5 and 7) had very nearly horizontal low energy tails; however, the spectrum shape from multiple interactions, represented mathematically by the convolution of two (or more) monochromatic shapes, will fall below horizontal at low energies. For computational convenience, however, the horizontal extrapolation of region B was used, and an "effective photofraction," ϕ', was used which was larger than that which would be measured for a monochromatic 1.78 MeV gamma ray. This effective photofraction will be considered further below.

The effect of the convolution of two line shapes is the key to a discussion of the effective photofraction, and since this convolution is not easily visualized, figure 10 has been constructed to illustrate this point. Figure 10 considers a pure γ_1 cascade from a level at an excitation energy of about 11.8 MeV; thus 10.0 and 1.78 MeV gamma rays are present in the cascade. The spectrum produced by the detectors is the sum of three different processes: 1) only the 1.78 MeV gamma ray interacts, 2) only the 10.0 MeV gamma ray interacts, and 3) both the 1.78 and 10.0 MeV gamma rays interact. Part (a) of figure 10 illustrates these three components, the area of each curve is proportional to the probability that the interaction it represents occurred. Thus the area of the "1.8 MeV" spectrum is $\epsilon(1.8)[\,1 - \epsilon(10.0)]$, the area of "10.0 MeV" is $\epsilon(10.0)[\,1 - \epsilon(1.8)]$, and the area of "1.8 + 10.0 MeV" is $\epsilon(1.8)\epsilon(10.0)$. Since $\epsilon \approx 0.5$ for this geometry, the three spectral areas are approximately equal. (Note that the sum of the areas is just $\epsilon(1.8) + \epsilon(10.0) - \epsilon(1.8)\epsilon(10.0)$ as given by equation 16.) The first two curves are

FIGURE 10: γ_1 Spectrum Generation

This figure shows the results of a computer calculation of the γ_1 spectrum shape from the decay of a level with excitation energy of 11.8 MeV. In part (a) of the figure, the three components which make up the observed γ_1 spectrum are shown. These three curves assume that: 1) only the 1.8 MeV gamma ray interacts, 2) only the 10.0 MeV gamma ray interacts, and 3) that both the 1.8 and 10.0 MeV gamma rays interact. The areas under the three curves are proportional to the probabilities that each of these particular types of interaction can occur. Part (b) shows the sum of the three curves, which should correspond to the observed γ_1 cascade spectrum, and is plotted with a different vertical scale than part (a). The text should be consulted for further details.

FIGURE 10

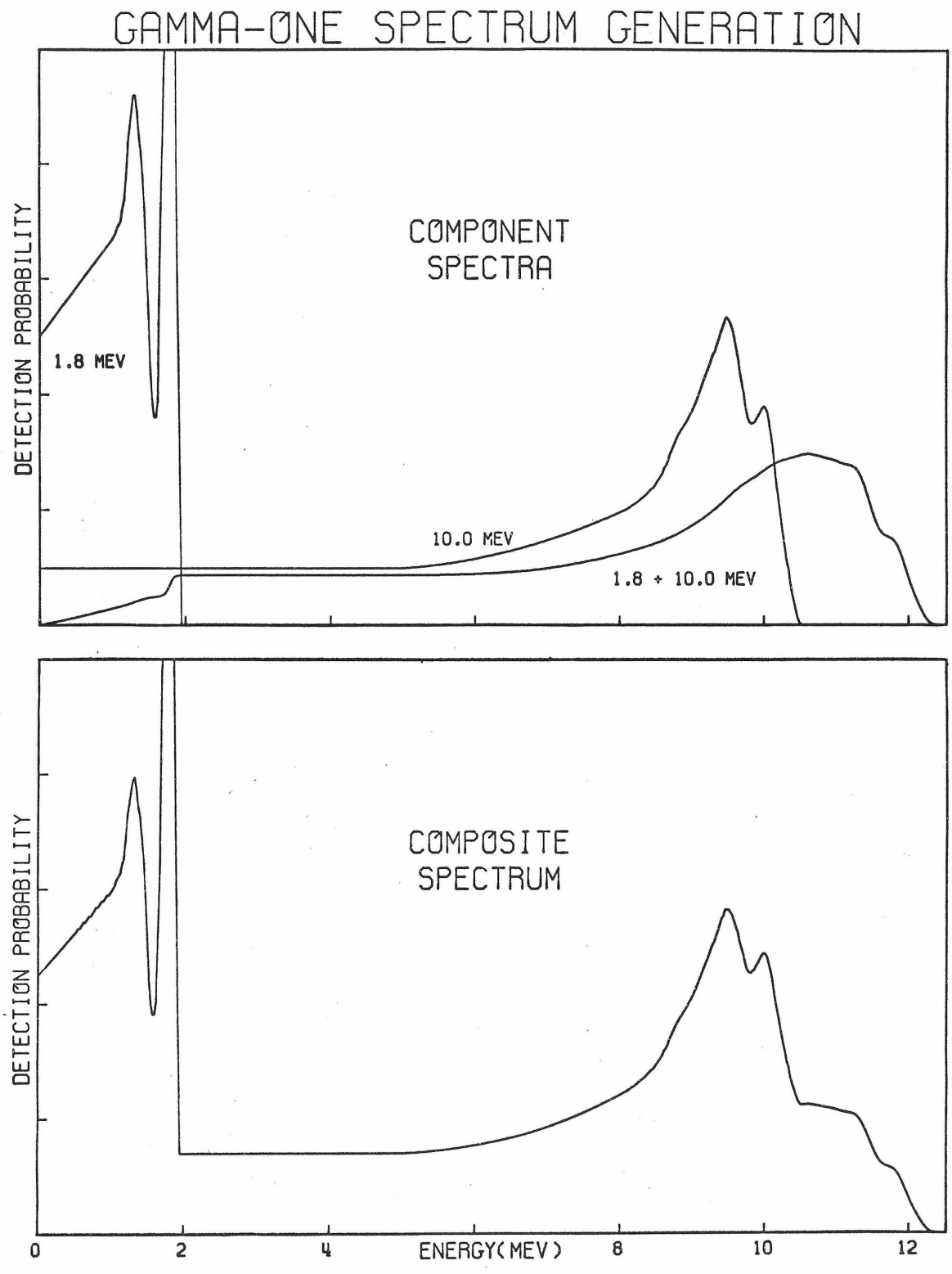
GAMMA-ONE SPECTRUM GENERATION
COMPONENT SPECTRA
1.8 MEV
10.0 MEV
1.8 + 10.0 MEV
DETECTION PROBABILITY
COMPOSITE SPECTRUM
DETECTION PROBABILITY
0
2
4
ENERGY(MEV)
8
10
12

just monochromatic gamma ray spectra. The third curve is the convolution of the curves of cases (1) and (2). Thus, if $f_{1.8}(E)$ represents the distribution of counts in the 1.8 MeV spectrum, $(\int_0^\infty f_{1.8}(E)\,dE = 1)$, and $f_{10.0}(E)$ is defined in the analogous way, then

$$f_{1.8+10.0}(E) = \epsilon(1.8)\epsilon(10.0)\int_0^E f_{1.8}(E')f_{10.0}(E-E')\,dE' \qquad (18)$$

Since $f_{10.0}(E)$ is approximately constant for $E < 5$ MeV, the convolution integral of equation 18 is just proportional to $\int_0^E f_{1.8}(E')\,dE'$ for $E < 5$ MeV. These details are shown in figure 10a; in figure 10b, the three curves are summed to yield the expected spectral shape.

The shape used for the 1.8 MeV spectrum in figure 10 is essentially the shape obtained for 1.63 MeV gamma rays given in figure 7, but scaled upward in energy and modified in peak area to reproduce the photofraction expected for 1.78 MeV radiation (thus the most important feature, the photofraction, is correct). The 10.0 MeV shape was obtained simply by shifting in energy an approximately monochromatic (79%) spectrum of 9.17 MeV gamma rays obtained from the $^{13}C(p,\gamma)^{14}N$ reaction at the 1.747 MeV resonance (Rose et al., 1964). Approximate corrections for cascades competing with γ_0 in this 9.17 MeV spectrum were made by lowering the plateau height of the 10.0 MeV spectrum until the ratio of the 10.0 MeV peak height to the low energy plateau of the composite spectrum of figure 10 approximately matched that obtained experimentally for pure γ_1 cascades. The Caltech IBM 7094 computer was programmed to accept single gamma spectra and perform the

numerical integrations and normalizations necessary to construct the displayed spectra. The CalComp plotter generated the figure from the computed output.

The extrapolation procedure of figure 9 can be applied to the "idealized" spectrum of figure 10b and a value of ϕ' extracted. This ϕ' is the effective photofraction which would be required to match the actual area of figure 10b, if the extrapolation procedure for the counts in the low channels was precisely followed. For figure 10b, $\phi' = 0.47$. This is to be compared with the value for monochromatic 1.78 MeV radiation, $\phi' = 0.43$, from p. 45.

In addition, from some of the strongest of the $^{27}Al(p,\gamma)^{28}Si$ γ_1 resonances, most of the low-energy tail of the 1.78 MeV peak was undistorted; thus the procedure utilizing the effective photofraction could be avoided and, in fact, inverted to calculate ϕ'. From the predominantly two-gamma cascade spectrum of the 1.380 MeV resonance (Boydell, 1967), an effective photofraction of 0.48 was obtained. The value adopted throughout the spectral analyses was 0.46 with an uncertainty of 20%. However, with the enhancement of the high energy region of the pulse height spectrum characteristic of the present geometry, this 20% uncertainty in the treatment of regions C and D typically gave uncertainties of $< 5\%$ in the total number of spectrum events for a γ_1 spectrum.

It is evident from figure 10 that the value of ϕ' required will depend on the particular cascade structure. In particular, a triple cascade through the 1.78 MeV state with another member of energy slightly above 1.78 MeV will build up the spectrum just above the

1.78 MeV photopeak; this will lead (with the extrapolation "recipe") to the choice of a large value for the low energy plateau. This infers that if the variation in such low energy behavior is to be absorbed solely in ϕ', then ϕ' must be considerably larger in such situations. This was investigated with the aid of the spectrum-generation computer program for two different three-gamma cascades. The γ_2 cascade was considered, this cascade includes a 2.84 MeV member which will distort the plateau just above the 1.78 photopeak. The spectrum generation program showed that $\phi' = 0.79$ for this case. But the justification for using $\phi' = 0.46$ for all analyses is simply that for such a triple cascade, very few events are in the 1.78 MeV spectrum (the probability of only the 1.78 MeV member interacting is 0.15 as compared with $\epsilon_t \approx 0.83$). If 0.46 were used for ϕ', the effect on N_i would be less than 7%. The spectrum-generation program was also run for the case of a triple cascade with members of 5.0, 5.0, and 1.78 MeV. For this case, $\phi' = 0.52$ was obtained, and the error made by using $\phi' = 0.46$ is only 2%.

Of the many resonances for which branching ratios are known, no triple cascades which proceed through the 1.78 MeV state and include another transition with energy less than 2.84 MeV have been detected, with branching ratios of greater than 5%. Higher order (than 3) cascades are rare. Thus using $\phi' = 0.46$ and admitting an error $\leq 7\%$ in the determination of N_i will yield correct results. In practice, if branching ratios were known, this error could be reduced for cases known not to exhibit triple cascades. Even if branching ratios were not known, the spectral shapes for predominantly triple cascade

resonances were easily distinguished from the common γ_1 transitions.

Resonance spectra for several $^{27}Al(p,\gamma)^{28}Si$ resonances are shown in the following three figures to illustrate the general characteristics of typical spectra to which this extrapolation method was applied. Figure 11 shows a predominantly γ_0 cascade, figure 12 shows a predominantly γ_1 cascade, and figure 13 shows a complex, predominantly three-gamma cascade.

C. Partial Detection Efficiency

The techniques of the preceding section were used wherever possible, i.e., where the low pulse height region was not seriously distorted by contaminants or by the $^{27}Al(p,\alpha'\gamma)^{24}Mg$ reaction. For some $^{27}Al(p,\gamma)^{28}Si$ resonances, and for all the $^{24}Mg(\alpha,\gamma)^{28}Si$ resonances, the low energy extrapolation techniques could not be applied. For these cases, only some fraction f of the resonance spectrum was statistically meaningful, and the partial detection efficiency $\eta(f)$ was required. As defined in the introduction, $\eta(f)$ is the probability that the gamma decay of a given resonance will result in an interaction with the crystals yielding a pulse height greater than a fraction f of the full energy pulse height E_x. If $N_i'(f)$ is the number of pulses greater than fE_x, it follows that

$$\eta(f) = \frac{N_i'(f)}{N_i} \epsilon_t \qquad (19)$$

For $f = 0$, $N_i'(0) = N_i$, and $\eta(0) = \epsilon_t$. If $\eta(f_0)$ were approximately independent of the type of cascade (for some fraction f_0), the use of $\eta(f_0)$, together with the number of pulses above f_0E_x, would allow

FIGURE 11: $^{27}Al(p,\gamma)^{28}Si$ 0.774 MeV Resonance Spectrum

This figure shows the gamma ray spectrum measured at the 0.774 MeV resonance in the $^{27}Al(p,\gamma)^{28}Si$ reaction. This resonance is predominantly a direct ground state transition (73% according to Endt and Van der Leun, 1967). The spectrum has been corrected for beam-induced, non-resonant, background and a beam-independent background, using the methods of Appendix II.

FIGURE 11

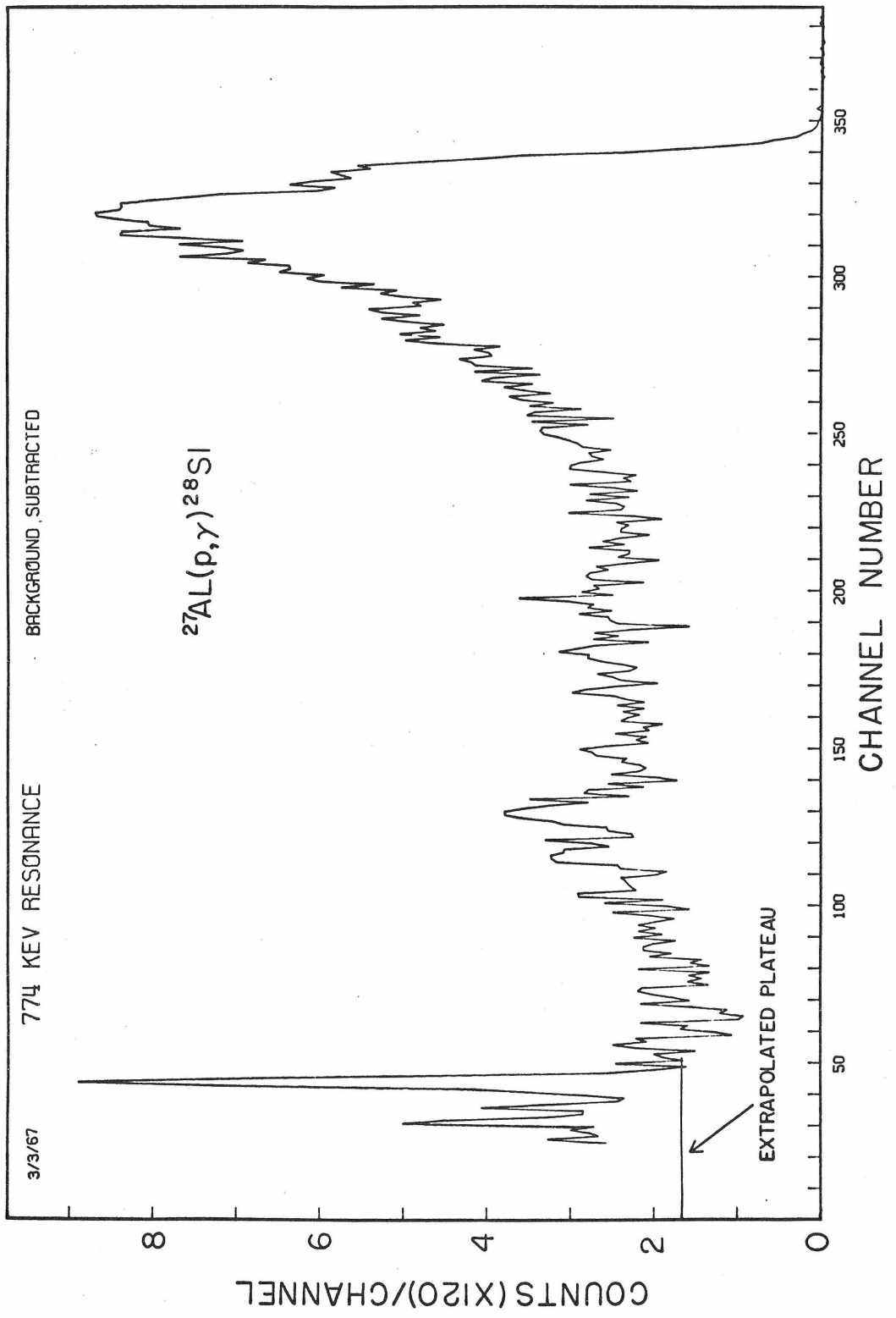
3/3/67
774 KEV RESONANCE
BACKGROUND SUBTRACTED
$^{27}AL(p,\gamma)^{28}SI$
EXTRAPOLATED PLATEAU
COUNTS (X120)/CHANNEL
CHANNEL NUMBER
0
2
4
6
8
50
100
150
200
250
300
350

FIGURE 12: $^{27}Al(p,\gamma)^{28}Si$ 0.992 MeV Resonance Spectrum

This figure shows the gamma ray spectrum measured at the 0.992 MeV resonance in the $^{27}Al(p,\gamma)^{28}Si$ reaction. This resonance is predominantly (78%) a γ_1 transition to the first excited state of ^{28}Si (Azuma, 1966; Boydell, 1967). The spectrum has been corrected for beam-induced, non-resonant, background and a beam-independent background, using the methods of Appendix II.

FIGURE 12

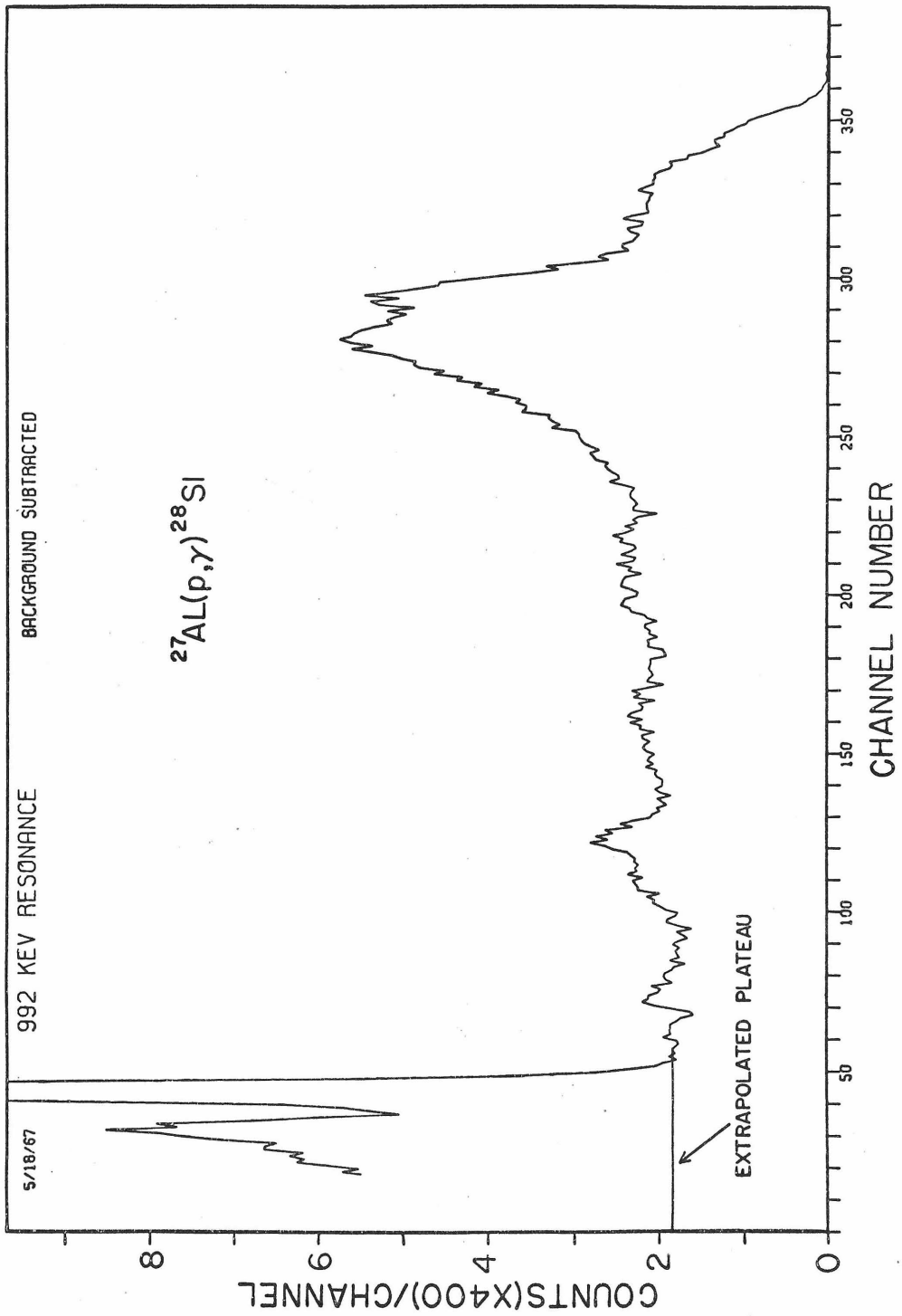
5/18/67
992 KEV RESONANCE
BACKGROUND SUBTRACTED
$^{27}AL(p,\gamma)^{28}SI$
EXTRAPOLATED PLATEAU
COUNTS(X400)/CHANNEL
CHANNEL NUMBER
0
2
4
6
8
50
100
150
200
250
300
350

FIGURE 13: $^{27}Al(p,\gamma)^{28}Si$ 1.317 MeV Resonance Spectrum

This figure shows the gamma ray spectrum measured at the 1.317 MeV resonance in the $^{27}Al(p,\gamma)^{28}Si$ reaction. This resonance is predominantly triple cascade transitions (73% according to Endt and Van der Leun, 1967). The spectrum has been corrected for beam-induced, non-resonant, background and a beam-independent background, using the methods of Appendix II.

FIGURE 13

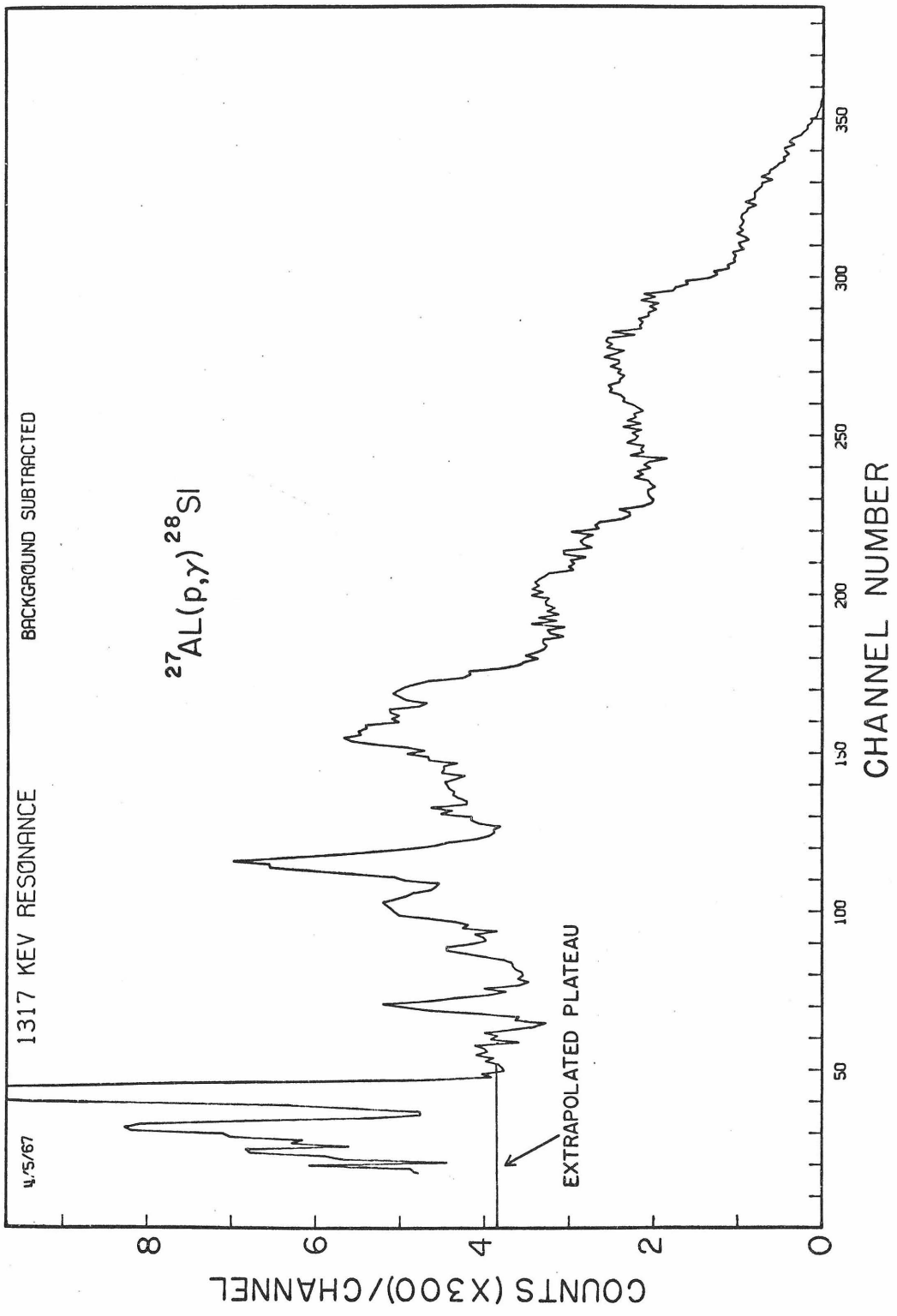
4/5/67
1317 KEV RESONANCE
BACKGROUND SUBTRACTED
$^{27}AL(p,\gamma)^{28}SI$
EXTRAPOLATED PLATEAU
COUNTS (X300)/CHANNEL
CHANNEL NUMBER
0
2
4
6
8
50
100
150
200
250
300
350

an accurate estimate of N_γ for any resonance; i.e., $N_\gamma = N_i'(f_0)/\eta(f_0)$.

In order to test the dependence of $\eta(f)$ on cascade structure and on f, spectra were recorded for 22 $^{27}Al(p,\gamma)^{28}Si$ resonances for which branching ratios were known, i.e., for which ϵ_t could be directly calculated from monochromatic gamma ray efficiencies, and for which N_i could be obtained by the extrapolation procedure of Section III.B. From these data, using equation 19, $\eta(f)$ could be calculated for each resonance as a function of f. The decay schemes of these 22 resonances ranged from cases in which a particular branch dominated the decay, to extremely complex decays with numerous branches. As would be expected, the variations of $\eta(f)$ as a function of f were very similar for resonances having similar decay schemes. Figure 14 presents several curves, each calculated by averaging $\eta(f)$ over several resonances dominated by the type of cascade indicated on the curves. In addition, the extreme values of $\eta(f)$ encountered among the 22 resonances studied are shown.

At a fraction of about 0.35, the η curves do have roughly the same value; the extreme cases give a variation in η of $\pm 13\%$ for this fraction. In many cases, the spectral shape at high pulse heights indicated the dominance of a particular decay mode, suggesting the selection of a particular η curve. Hence greater precision could be obtained than by the use of the averaged curves of figure 14. In some cases, contaminant problems forced the choice of a higher fraction, $f > 0.35$, which increases the uncertainties.

FIGURE 14: Partial Detection Efficiency Curves

This figure illustrates the partial detection efficiency $\eta(f)$ for various types of cascade structures, as a function of f, where $\eta(f)$ refers to the probability of detecting a pulse from the NaI crystals larger than the fraction f of the full energy pulse height (i.e., above the energy fE_x, where E_x is the resonance level excitation energy). The solid lines represent the extreme values of η obtained from the 22 resonances studied to construct these curves. Broken lines were obtained by averaging values of η for many resonances, all of which had a common dominant decay mode. As f goes to zero, η approaches ϵ_t.

FIGURE 14

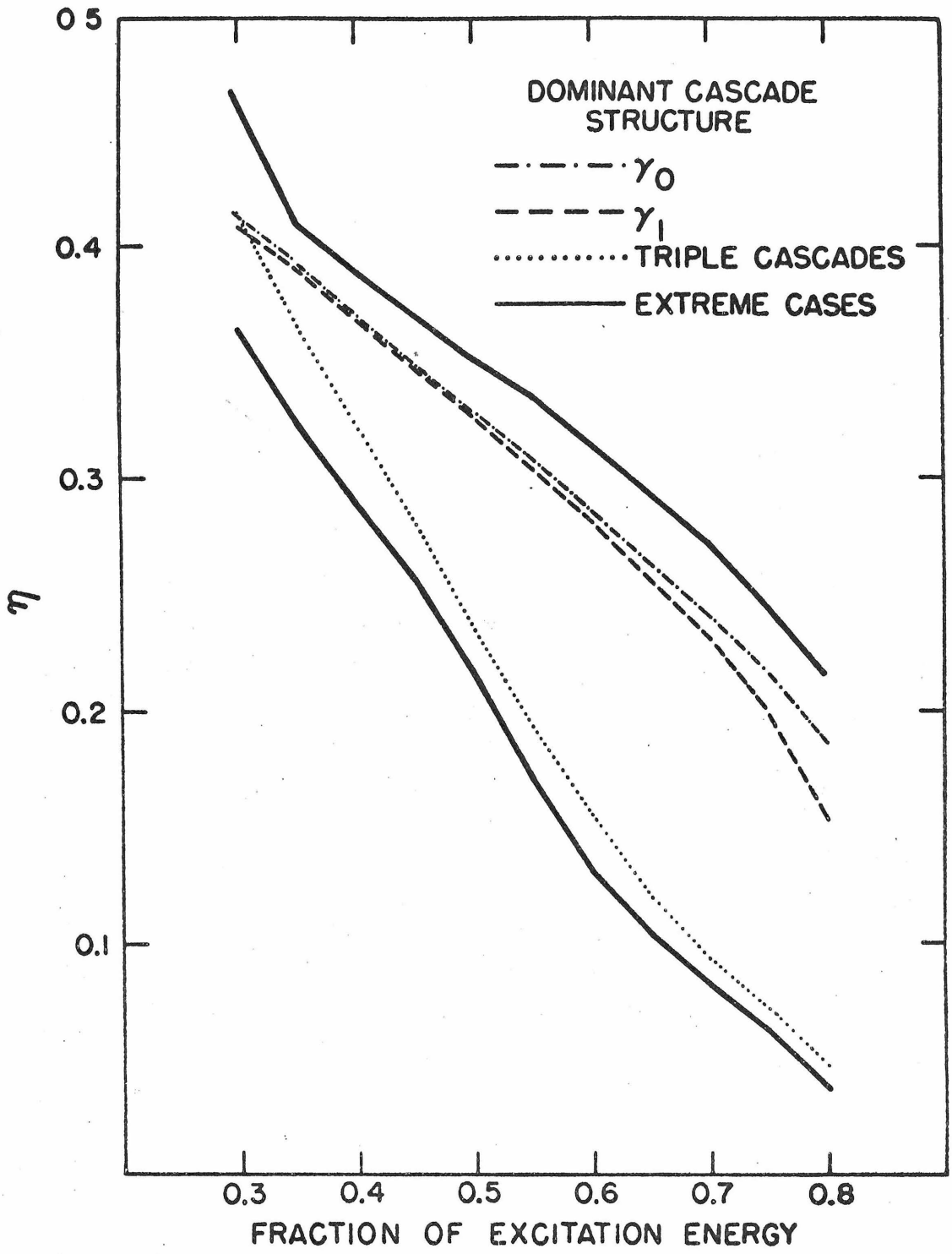
0 5
0.4
0.3
0.2
0.1
η
DOMINANT CASCADE STRUCTURE
γ_0
γ_1
TRIPLE CASCADES
EXTREME CASES
0.3
0.4
0.5
0.6
0.7
0.8
FRACTION OF EXCITATION ENERGY

D. Catalog of Spectrum Analysis Methods

For future reference, it will be convenient to catalog the five possible types of spectrum analysis which were used for different resonances.

1) For resonances for which the branching ratios were known and for which the extrapolation procedure of section IV.B was applicable, the determination of $N_\gamma = N_i/\epsilon_t$ was straightforward. Of the 85 $^{27}Al(p,\gamma)^{28}Si$ resonances studied, 35 were analyzed in this manner.

2) If the branching ratios were not available in the literature, but the extrapolation procedure of section IV.B was applicable, an estimate was made of the value of ϵ_t. The variation in the ratio $N_i'(f)/N_i$ was compared to the variation in the $\eta(f)$ curves (which differ by only the constant factor ϵ_t from this ratio) and by this means the dominant mode of decay was easily inferred. For the present geometry ϵ_t is not a strong function of the cascade structure of the resonance (with the exception of a predominantly γ_0 decay, which is easily identifiable, as can be seen by comparing figures 11, 12, and 13). This approximate knowledge of the cascade structure was sufficient to determine ϵ_t quite accurately. For this method, which was applied to 10 $^{27}Al(p,\gamma)^{28}Si$ resonances, $N_\gamma = N_i/\epsilon_t$ as in the first case, above.

3) If the branching ratios were known, but the extrapolation procedure of section IV.B could not be applied, i.e., the spectrum was too distorted in the low channels, the η curves were used. However, with the catalog of 22 resonances for which η curves had been experimentally determined, it was possible to find one, or a combi-

nation, of the 22 resonances having virtually the same branching ratios as the level in question. The partial detection efficiency is, of course, the same for resonances having identical cascade structure. Thus $\eta(f)$ for the level in question could be determined. Application of this $\eta(f)$ to any usable fraction f of the spectrum gave a determination of N_γ. This procedure was applied to 7 $^{27}Al(p,\gamma)^{28}Si$ resonances.

4) If the branching ratios were unknown, and the extrapolation procedure could not be used, the η curves were used. If the level was strong enough to obtain a usable spectrum above a pulse height of about 4 MeV, then a fraction $f \approx 0.35$ could be used. For $f = f_0 \approx 0.35$, $\eta(f_0)$ is roughly independent of cascade structure so that $N_\gamma = N_i'(f_0)/\eta(f_0)$. This procedure was applied to 7 $^{27}Al(p,\gamma)^{28}Si$ resonances. In addition, for most of the 16 $^{24}Mg(\alpha,\gamma)^{28}Si$ resonances, branching ratios were partially, but not completely, known; these spectra were in a class between cases 3 and 4.

5) For some of the very weak, or very broad, levels, spectra were not taken. For these cases, the fraction f_b corresponding to the SCA lower bias level was determined and an average $\eta(f_b)$ used to convert the SCA counts directly to gamma ray yield. In some cases, visual determination of the dominant decay modes was attempted, allowing a better choice to be made for η. Since f_b was taken in the region 0.55-0.60 for most of the $^{27}Al(p,\gamma)^{28}Si$ data, reference to figure 14 shows that η is not very well determined. This procedure was applied to 26 $^{27}Al(p,\gamma)^{28}Si$ resonances.

V. METHODS OF YIELD ANALYSIS

The scaler counts recorded, as each resonance was traced out in small steps of the incident beam energy, were converted to resonant gamma yield using the techniques of Part IV (i.e., from a spectrum measured for each resonance, the ratio between N_γ and the SCA counts was obtained). It still remained, however, to relate this gamma ray yield information to total gamma resonance strengths.

The most general form for the yield per incident particle, $y(E_b,t)$ for the reaction $0 + 1 \rightarrow 2 + \gamma$, at laboratory bombarding energy E_b, on a target of thickness t is (Gove, 1959):

$$y(E_b,t) = \int_{x=0}^{t}\int_{E_i=0}^{\infty}\int_{E_{lab}=0}^{E_i} g(E_b,E_i)\,w(E_i,E_{lab},x)\,\sigma(E_{lab})\,n_1(x)\,dx\,dE_{lab}\,dE_i \tag{20}$$

where: $g(E_b,E_i)$ = the resolution function for the incident beam at average energy E_b

$w(E_i,E_{lab},x)dE_{lab}$ = the probability a particle incident at energy E_i has laboratory energy between E_{lab} and $E_{lab} + dE_{lab}$ at a depth x in the target

$\sigma(E_{lab})$ = the reaction cross section at energy E_{lab} for the reaction $0 + 1 \rightarrow 2 + \gamma$

and

$n_1(x)$ = number of target nuclei/cc at depth x in the target.

The Breit-Wigner formula for a resonant radiative capture cross section is given by:

$$\sigma(E) = \pi\lambda^2 \frac{(2J_r+1)}{(2J_0+1)(2J_1+1)} \frac{\Gamma_0\Gamma_\gamma}{(E - E^r_{CM})^2 + (\Gamma/2)^2} \qquad (21)$$

where: E = center of mass energy = $\left(\frac{A_1}{A_1+A_0}\right)E_{lab}$

E^r_{CM} = center of mass resonance energy = $\left(\frac{A_1}{A_0+A_1}\right)E^r_{lab}$

$\lambda^2 = \hbar^2/2ME$, where M is the reduced mass of nuclei 0 and 1

J_0 = spin of incident particle

A_0 = mass number of incident particle

J_1 = spin of target nucleus

A_1 = mass number of target nucleus

Γ = total width of resonance, center of mass energy scale

Γ_0 = width of incident particle channel, center of mass energy scale

Γ_γ = total electromagnetic width of the resonance, center of mass energy scale.

One of two standard methods of yield analysis is the "thick target technique" in which a target is used whose energy thickness is large compared to the resonance width. Thus a step in the yield function is observed (with a flat top if $n(x)$ = constant) as the beam energy is raised through the resonance energy. If $n_1(x) = n_1$ and $\varepsilon(E)$ is the stopping power of the target $\left(\varepsilon(E) = \frac{1}{n_1}(dE_{lab}/dx)\right)$, then it is well known (Gove, 1959) that equation 20 yields for the thick target step height:

$$y(\infty,\infty) = \left[\varepsilon(E^r_{lab})\right]^{-1} \int_{-\infty}^{\infty} \sigma(E)\, dE_{lab} \qquad (22)$$

which may be solved with the use of equation 21 to yield, recalling that $y = N_\gamma/N_0$, where N_0 = number of incident particles,

$$(2J_r+1)\left(\frac{\Gamma_0\Gamma_\gamma}{\Gamma}\right)_{CM} = \left(\frac{A_1}{A_0+A_1}\right)^3 \frac{M_0 E^r_{lab} \varepsilon(E^r_{lab})(2J_0+1)(2J_1+1)}{\hbar^2\pi^2} \frac{N^\infty_\gamma}{N_0} \tag{23}$$

where M_0 = mass of incident particle. In this equation N^∞_γ/N_0 refers to the resonant radiative capture yield on the thick target plateau. The subscript "CM" is added to the resonance strength as a reminder that strengths are quoted in this paper on the center-of-mass energy scale. It should be noted here that the procedure of quoting the resonance strengths in center-of-mass coordinates is not always normal practice in the literature, but has been adopted here since it is appropriate to the astrophysical use of the data.

For the case of a target with several constituents, note that $dE/dx = \sum_i n_i \varepsilon_i$ where n_i is the number density of element i and ε_i is the stopping cross section for element i. For the situation where Al is the resonant target nucleus,

$$\varepsilon(E_{lab}) = \varepsilon_{Al}(E_{lab}) + \sum_{i \neq Al} \frac{n_i}{n_{Al}} \varepsilon_i(E_{lab}) \tag{24}$$

The second standard method of analysis is the "thin target technique" in which no particular attention is paid to target thickness, although it is usually convenient to use a thin target. Rather than observing the peak yield (which the thick target technique does for the special case of a flat-topped peak), the area under the yield curve is

used for calculating the resonance strength. Several authors (Gove, 1959; Palmer et al., 1963) have shown that

$$\int_{-\infty}^{\infty} y(E_b,t)\, dE_b = n_1 t \int_{-\infty}^{\infty} \sigma(E)\, dE_{lab} \tag{25}$$

from which it follows that

$$(2J_r+1)\left(\frac{\Gamma_0\Gamma_\gamma}{\Gamma}\right)_{CM} = \left(\frac{A_1}{A_0+A_1}\right)^3 \frac{M_0 E^r_{lab}(2J_0+1)(2J_1+1)}{\pi^2\hbar^2 n_1 t} \int_{-\infty}^{\infty} y(E_b,t)\, dE_b \tag{26}$$

where $y(E_b,t)$ refers to the resonant yield due to a single resonance at bombarding energy E_b. Obviously if the target thickness is large, several resonances may not be resolved and determining which radiative captures, for a given E_b, are due to each resonance may not be trivial. If a thin target is employed the possibility of resolving resonances is greatly enhanced.

Resonance curves were traced out for all resonances studied, and one or both types of analysis were used on each resonance. One special case where both methods were applied is discussed in part IX, resonance yield curves are illustrated by figures 15, 16, and 18.

It should be stressed that with a knowledge of the target composition, an absolute measurement of the resonance strength is straightforward, using thick target techniques. But such an absolute measurement is difficult using thin target analysis because the areal density of target nuclei $(n_1 t)$ is not easily measured. Relative

strengths among many resonances can be accurately obtained using thin target techniques, however, by bombarding the same target spot so that $n_1 t$ cancels out in the strength ratios.

A useful identity which will be required in Part IX is the ratio of equations 26 and 23 for a target thick enough that N_γ^∞ is attained:

$$\mathcal{E}(E^r_{lab}) = \frac{(n_1 t)^{-1}}{y(\infty,\infty)} \int_{-\infty}^{\infty} y(E_b, t)\, dE_b \qquad (27)$$

VI. THE $^{27}Al(p,\gamma)^{28}Si$ REACTION

The preceding three chapters have discussed in considerable detail the methods of analysis to be employed in obtaining resonance strengths. The application of these methods to the two reactions of interest will now be considered.

A. Experimental Details

Targets were prepared from spectrographically analyzed aluminum (> 99.99% Al, obtained from Johnson, Matthey & Co., Ltd., London) evaporated in vacuo onto 0.25-mm tantalum target blanks from directly-heated tantalum boats. Both the target blanks and the boat were outgassed at temperatures above red heat in vacuo prior to the evaporation. After the evaporation, the targets were immediately transferred under a dry argon atmosphere to the target chamber. The pre-heating reduced ^{19}F contamination by a factor of 20 and handling the target in argon significantly reduced ^{15}N contamination. Tests of target purity will be discussed in part IX.

The gamma ray yield was monitored by a single channel analyzer which was set to accept pulses between 7.5 and 14.5 MeV in order to minimize uncertainty due to $^{19}F(p,\alpha'\gamma)^{16}O$ events. (The $^{19}F(p,\alpha_3\gamma)^{16}O$ gamma ray is 7.12 MeV).

The H^+ beam was used for most of the experimental work; at the lowest energies, the H_2^+ beam was employed. Beam currents were usually less than 0.5 μa, to avoid excessive count rates. Since no particular efforts toward target cooling were taken with the Al targets, the targets were hot enough that carbon deposition was only

slight.

B. Thick Target Analysis

Below 1.4 MeV, the $^{27}Al(p,\gamma)^{28}Si$ reaction has been studied by many groups (Endt and Van der Leun, 1967) and the location of the (p,γ) resonances are well known. Most of the resonances were sufficiently isolated from other resonances, and narrow enough, to allow thick target analysis to be employed. It was only necessary to measure the yield function in the neighborhood of the known resonances. In addition, 12 of the resonances above 1.4 MeV were studied by thick target techniques.

In the earlier stages of the experimental work, spectra were taken several keV above, and several keV below, the resonance energy. The methods of Appendix II were then applied to correct for beam-induced nonresonant contributions and beam-independent contributions. While this had the advantage that combining the spectra gave N_γ^∞ directly, i.e., the spectra were taken completely on and off the thick target step, it had the disadvantage that the two spectra were often taken with as much as 5 keV energy separation. Contaminant contributions might change substantially over this range, so γ-ray spectra were also observed by bombarding the back of the target backing at the same two energies whenever contamination was present in the "off resonance" spectrum. These back-of-the-target measurements gave the ratio of the contaminant yield at the two energies, from which a correction to the resonance spectrum could be made if necessary.

An alternative procedure adopted in later stages of the work was to take the "resonance" and "off resonance" spectra on the leading edge of the thick target step, within one or two keV separation in energy. From these spectra, a spectrum shape could be obtained free of all but the most rapidly varying background. The spectrum shape, together with the methods of spectrum analysis (IV.D.1-5) allowed the determination of the ratio N_γ/N_{SCA}. Thus the SCA counts were converted to N_γ for the yield analyses.

Equation 23 was applied to the values of N_γ^∞ obtained. The values of $\mathcal{E}(E)$ were taken from the tables by Whaling (1958) below 1.4 MeV and from data of Nielsen (quoted by Bichsel, 1964) above 1.4 MeV.

Table 1 lists the resonance strengths obtained from the thick target analysis. The methods of gamma spectrum analysis are also indicated in the "N_γ" column, reference should be made to section IV.D for discussion of these methods. The uncertainties which have been attached to the thick target resonance strengths of table 1 arise from several sources. For most thick target measurements, the error in the extraction of N_γ was one of the dominant contributions to the total uncertainty. For the highest energy thick target yields, the presence of broad resonances made the height of the thick target step open to additional uncertainties.

Table 2 lists the uncertainties in N_γ which may be taken as representative of each of the spectrum analysis methods due to angular distributions, uncertainty in ϵ_t (or $\eta(f)$), and in N_i (or $N_i'(f)$). On a

specific resonance, errors depend on the type of cascade structure, neighboring resonances, and contaminant contributions.

For thick target data, any uncertainty in the dE/dx values employed introduces a corresponding error in the resonance strength. Whaling's formula seems to be high by about 2% compared to Nielsen's data for higher energies. Assigning a standard deviation of 7% to Whaling's formula over the range 0.3-1.4 MeV is probably reasonable, with the error possibly increasing at the lower energies. Nielsen's data above 1.4 Mev should be reliable to better than 3% (Nielsen, 1961).

Errors due to uncertainties in beam current integration, dead time corrections, or contaminant corrections remained negligible throughout.

C. Thin Target Analysis

The thick target method of analysis is difficult to apply for broad resonances since the thick target step height is not obtained unless very thick targets are used. Such targets would introduce contributions from neighboring resonances. For the few broad resonances below 1.4 MeV, a yield curve was traced out, and the integrated yield determined. Since the widths and positions of these resonances are well known, extraction of the integrated yield was not difficult.

From equation 26, the ratio of the integrated yields ($Y = \int y(E_b, E_{lab})\, dE_{lab}$) of two resonances (denoted by 1 and 2) measured on the same target, is

$$\frac{Y_1}{Y_2} = \frac{E_2}{E_1} \frac{[(2J+1)\Gamma_p\Gamma_\gamma/\Gamma]_1}{[(2J+1)\Gamma_p\Gamma_\gamma/\Gamma]_2} \quad . \tag{28}$$

The relative strengths thus obtained were normalized in all cases to the thick target yield at the 0.992 MeV resonance.

Above 1.4 MeV only one group (Antoufiev et al., 1963) had published a yield curve for the (p,γ) reaction. While they had determined energies for the more prominent, narrow resonances, they had not attempted identification or strength determinations for any of the broad resonances. For some of the narrow resonances, they had determined resonance strengths, but for the most part they gave only strengths for the γ_1 transition. Further, at lower energies, below 1.4 MeV, their quoted strengths were in gross disagreement with both our thick target yield measurements and other published measurements. Their published yield curve was not of sufficient detail to allow an accurate determination of the resonances present. Thus it was necessary to construct a yield curve for the region above 1.4 MeV in order to proceed with analysis.

An excitation function was therefore measured from 1.40 - 2.62 MeV using steps of ≤ 2.5 keV, each resonance being traced out in steps of 1 keV. The target used was of 7.5 keV thickness for 1 MeV protons; beam currents were ~ 0.3 μa; and the integrated charge per point was ~ 50 μC. The quantity actually measured for the excitation function was the portion of the gamma ray spectrum which fell in the window of the SCA. The excitation function traced out is shown in

figure 15; only a room background, measured with the beam intercepted by a quartz plate 2 meters ahead of the target chamber, has been subtracted from the experimental points. Experimental points are not shown in figure 15 because they could not be resolved on the scale of the figure; however, experimental points are shown for a small region of the spectrum in figure 16 to be discussed below. In addition to tracing out the excitation function, long runs were taken on and off about half the resonances in order to obtain resonance spectra by the methods of Appendix II. Using methods 1-4 of section IV.D, the ratio N_γ/N_{SCA} could be obtained for these resonances. For the other resonances, which were too broad or too weak to obtain spectra, method 5 was used in which $N_\gamma = N_{SCA}/\eta(f_b)$.

The experimental yield curve of figure 15 obviously contains many resonances, and in order to determine the strength of each resonance, it was necessary to fit this curve with Breit-Wigner resonances. The procedure used for this curve fitting will now be described.

The yield $y(E_b,t)$ from equation 20 can be rewritten as

$$y(E_b,t) = \int_{E_{lab}=0}^{\infty} Q(E_b,E_{lab})\sigma(E_{lab})\, dE_{lab} \qquad (29)$$

where $Q(E_b,E_{lab})$ physically represents the effects of beam resolution, target thickness, and beam straggle in the target. In terms of the quantities used in equation 20:

$$Q(E_b,E_{lab}) = \int_{E_i=E_{lab}}^{\infty}\int_{x=0}^{t} g(E_b,E_i)w(E_i,E_{lab},x)n_1(x)\, dx\, dE_i \qquad (30)$$

FIGURE 15: Yield Curve for the $^{27}Al(p,\gamma)^{28}Si$ Reaction

This figure shows the experimental yield curve measured for the $^{27}Al(p,\gamma)^{28}Si$ reaction in the energy range from 1.4-2.62 MeV. The energy scale has been adjusted so that energies coincide as far as possible with resonance energy measurements by Antoufiev et al. (1963). The quantity actually shown is the SCA counts obtained at each beam energy for an integrated charge of 50 μC. The SCA was set to accept pulses in the energy range 7.5-14.5 MeV. Room background has been subtracted from the points.

FIGURE 15

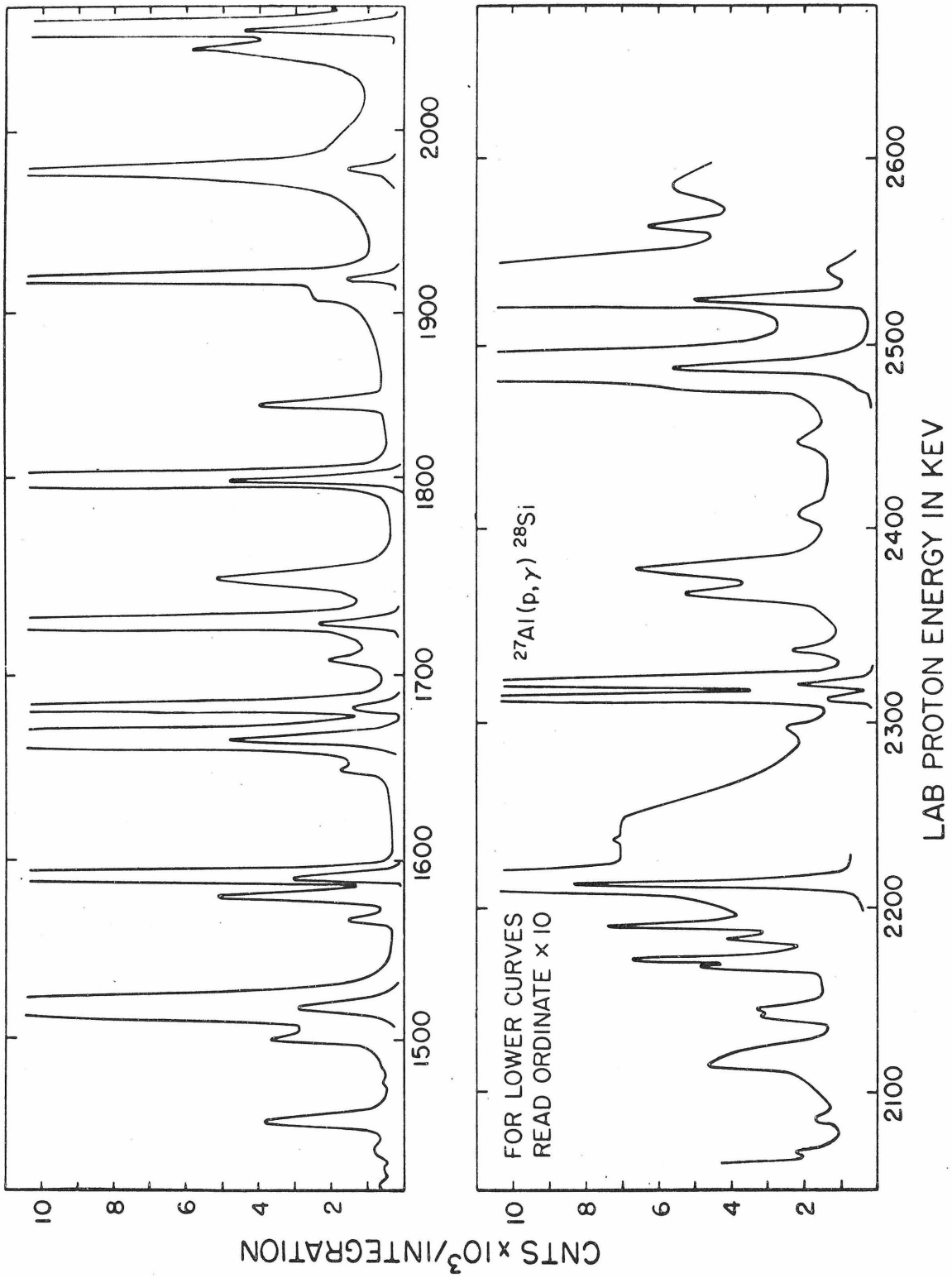
CNTS x 10³/INTEGRATION
LAB PROTON ENERGY IN KEV
FOR LOWER CURVES
READ ORDINATE x 10
27Al(p,γ) 28Si
10
8
6
4
2
1500
1600
1700
1800
1900
2000
2100
2200
2300
2400
2500
2600

For a very narrow resonance, $\sigma(E_{lab}) \propto \delta(E_{lab} - E^r_{lab})$; in which case, $y(E_b,t) \propto Q(E_b, E^r_{lab})$. The assumption was then made that the shape of the narrowest peaks observed in the yield function represented $Q(E_b,E_{lab})$; since Q is a function of beam energy, several such shapes were used to cover the entire energy range.

The values assumed for $Q(E_b,E_{lab})$ by this procedure were then used in equation 29 together with Breit-Wigner resonance parameters for $\sigma(E)$. The IBM 7094 computer was programmed to perform the integration of equation 29. This program accepted discrete points on a resolution function shape, and used least square fitting methods to fit these points with a series of quadratic curve segments. If a quadratic expression is used for Q in equation 29, the integral can be written in closed form. Thus replacing Q by a series of quadratic segments allowed $y(E_b,t)$ to be evaluated as a sum of several terms, rather than evaluating a numerical integral at each beam energy. The program also performed various useful normalizations on the Q's; the integrated yields were given by the program in units of "SCA counts-keV."

The general method of attack was to guess initial values of the Breit-Wigner parameters for all the obvious resonances of figure 15. The program then generated the contribution of every resonance at every beam energy of interest and produced the total resonant contribution at each beam energy. The fit to the experimental data thus obtained was inspected, and refined guesses were made of the resonance parameters. The program itself did not perform this variation in resonance parameters, but typically only three or four such

iterations were required to fit the yield curve. Figure 16 shows such a fit.

The output of this fitting program was the integrated yields, widths, and energies for all the resonances in this region. A smoothly varying background was also obtained. The resonance energies obtained in this fitting procedure were adjusted slightly to coincide as far as possible with those found by Antoufiev et al. (1963), since no special care was taken in our work to obtain absolute resonance energies.

Table 1 lists the resonance parameters obtained through this fitting procedure; the table also includes the thick target data of section VI.B. For the weaker resonances, the thin target data did not yield accurate widths; and for some stronger levels, upper limits of $\lesssim 2$ keV were all that could be reliably deduced. Even though widths were required in the computer fit, they are omitted from table 1 if they were poorly determined. The method of study (whether by thick or thin target techniques) is indicated, as well as the gamma spectrum analysis method used (methods 1-5 of section IV.D). Widths were not inferred from the thick target analyses. All thin target strengths were measured relative to the strong 0.992 MeV resonance strength.

The smoothly varying background may be taken as an upper limit to the nonresonant yield, or alternatively as unresolved broad resonances, which would be equivalent for the astrophysical purposes. A more stringent upper limit was obtained by subtracting the yield

FIGURE 16: Computed Fit to Yield Curve

A small segment of the experimental yield curve of figure 15 is shown in this figure together with the computed yield curve. Reference to figure 15 indicates that this segment of the yield curve is the most complex observed, and as such, was the most difficult to fit. The text should be consulted for details of the fitting procedure.

FIGURE 16

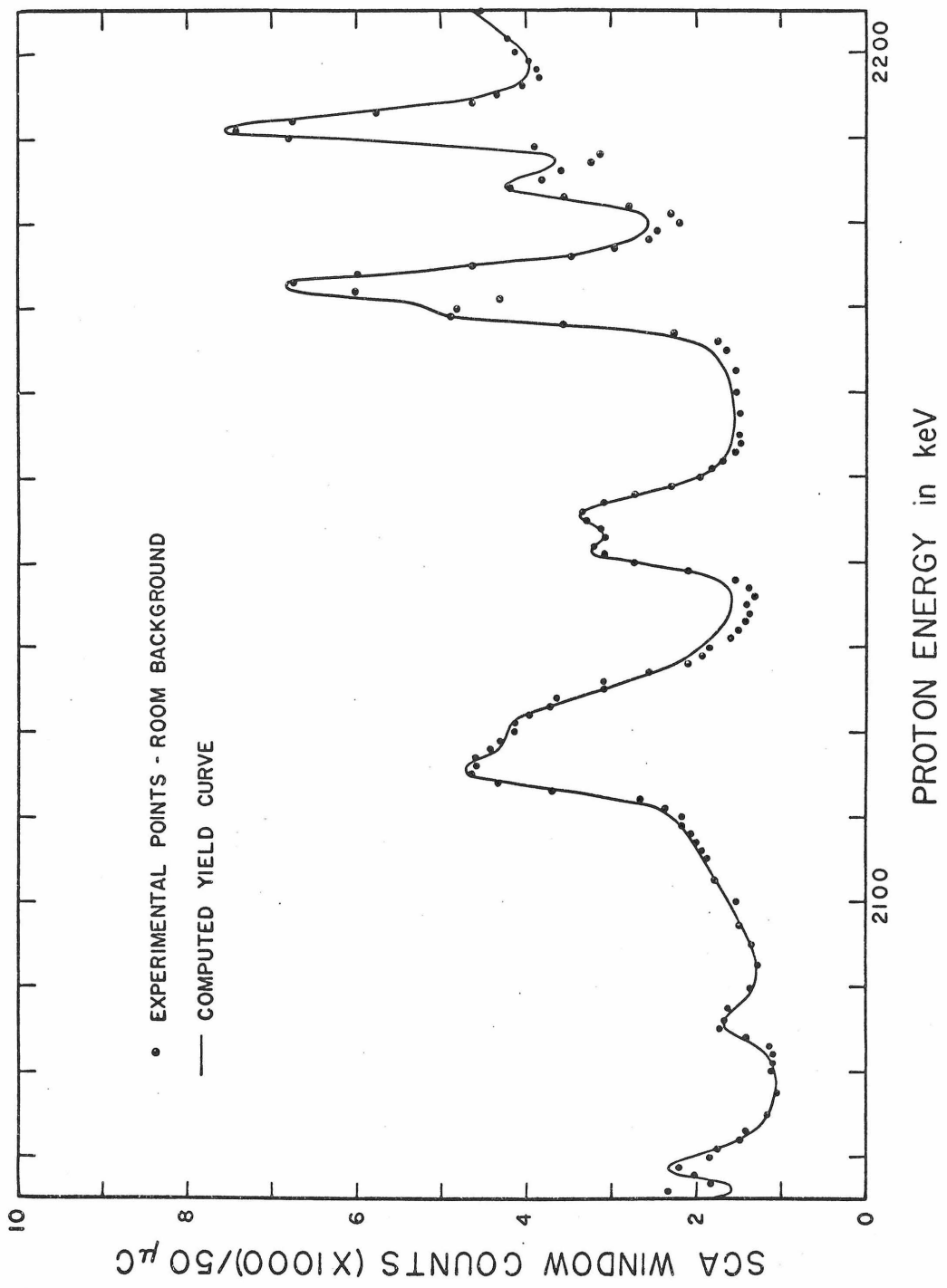
SCA WINDOW COUNTS (X1000)/50 μC
0
2
4
6
8
10
2100
2200
PROTON ENERGY in keV
• EXPERIMENTAL POINTS - ROOM BACKGROUND
— COMPUTED YIELD CURVE

as measured on the target backing. Since the target spot had considerably more bombardment than the backing, and hence more contamination, the result of the subtraction is still an overestimate of the nonresonant yield from the Al target. The resulting nonresonant yield has been converted to a cross section and is shown in figure 17. The total lack of knowledge of spectral characteristics for the nonresonant yield required the use of method 5 of section IV.D for the nonresonant yield analysis.

The principal contaminant reactions giving contributions within the SCA window were $^{13}C(p,\gamma)^{14}N$, $^{19}F(p,\gamma)^{20}Ne$, and $^{15}N(p,\gamma)^{16}O$. At three energies, well removed from any $^{27}Al(p,\gamma)^{28}Si$ resonances, particularly long runs were taken. The contaminant contributions were identified and removed from the spectrum thus obtained. After allowing for the contribution of distant $^{27}Al(p,\gamma)^{28}Si$ resonances, the nonresonant cross section obtained at 1.61 MeV was 75% of the previously determined "upper limit" at this energy. At 1.06 MeV the nonresonant cross section was 0.27 ± 0.14 μb and at 0.58 MeV, the nonresonant cross section was < 0.07 μb.

This background that remained after fitting the prominent resonances, could, of course, have been fitted by the addition of further broad resonances. But spectra for this "non-resonant" yield were not known, thus some of the structure evident in it might not even be due to the $^{27}Al(p,\gamma)^{28}Si$ reaction. In any case, even if this nonresonant yield is entirely due to the $^{27}Al(p,\gamma)^{28}Si$ reaction, it contributes less than 3% to the total photodisintegration rate of ^{28}Si at $T_9 = 5$ and is completely negligible for lower temperatures.

FIGURE 17: Nonresonant cross section for $^{27}Al(p,\gamma)^{28}Si$

This figure shows the upper limit for the nonresonant cross section obtained from a fit to the yield curve measured for the $^{27}Al(p,\gamma)^{28}Si$ reaction. At 1.61 MeV, a more careful determination of nonresonant yield gave a value 75% of the value given by the curve. At two lower energies, determinations were also made and the values thus obtained are given on the figure. The text should be consulted for further details.

FIGURE 17

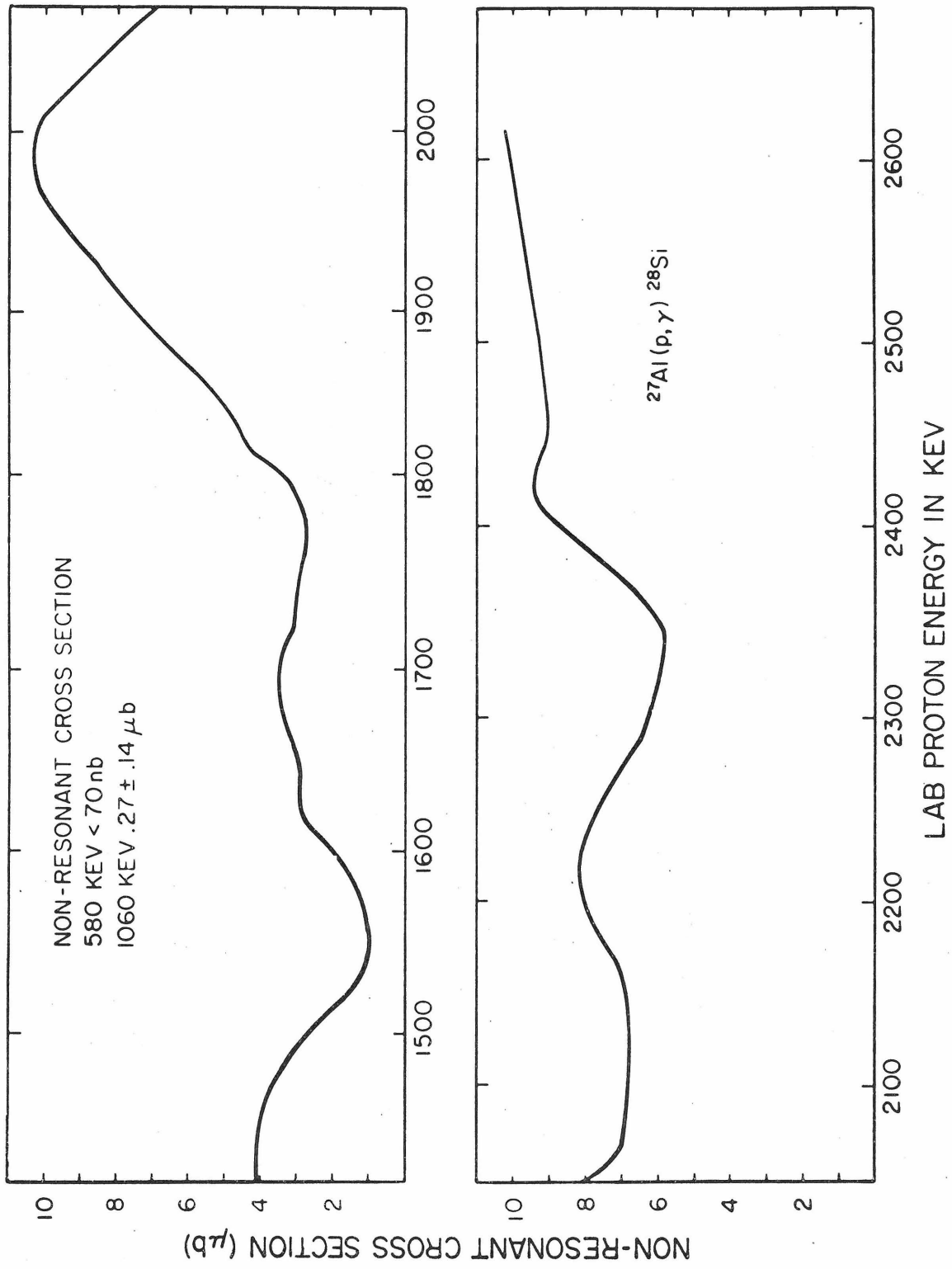
NON-RESONANT CROSS SECTION
580 KEV < 70 nb
1060 KEV .27 ± .14 μb
$^{27}Al(p,\gamma)\,^{28}Si$
NON-RESONANT CROSS SECTION (μb)
LAB PROTON ENERGY IN KEV
10
8
6
4
2
1500
1600
1700
1800
1900
2000
2100
2200
2300
2400
2500
2600

The total integrated nonresonant cross section above 1.4 MeV is ~ 10% of the total integrated resonance cross section.

Most of the uncertainties present in the thick target analysis are present in the thin target analysis as well. The uncertainty in $\varepsilon(E)$ does not appear explicitly in equations 26 and 27, but such uncertainty is still involved since all measurements were made relative to the 0.992 MeV resonance strength, which was determined by thick target analysis. Thus the 11% uncertainty in the resonance strength of the 0.992 MeV resonance is present, as well as approximately 10% uncertainty in the determination of the integrated yield of the 0.992 MeV resonance. For the integrated yields obtained from the fitting program, an uncertainty of 20% has been taken as representative.

Uncertainties have been entered in table 1. Where both thick and thin target data were taken, the strength shown in table 1 is a weighted average of the two measurements.

VII. THE $^{24}Mg(\alpha,\gamma)^{28}Si$ REACTION

The (γ,α) photodisintegration process competes with the (γ,p) process and a determination of the total photodisintegration rate of ^{28}Si therefore requires a knowledge of the (α,γ) resonance strengths. The detection techniques used in the study of the $^{27}Al(p,\gamma)^{28}Si$ reaction are directly applicable to this reaction and allow measurement of the resonance strengths for the two reactions on a consistent absolute strength scale.

A. Experimental Details

Targets were prepared either from reagent grade, metallic, natural magnesium, or from metallic, isotopic ^{24}Mg (99.7% ^{24}Mg, obtained from Oak Ridge National Laboratory) evaporated in vacuo from directly heated Ta boats. Since the vapor pressure of Mg is much higher than that of Al (the temperature required for a vapor pressure of 10^{-7} Torr is 740 °C for Al and 210 °C for Mg), and since much higher beam currents were required by the low yield of the (α,γ) reaction, target cooling was a necessity. The standard 0.25 mm tantalum target blanks could not be used due to the low thermal conductivity of Ta and 0.56 mm copper backings were used instead. This thickness of copper gives a total attenuation of gamma rays within 25% of that given by the standard Ta blanks over the energy range of interest. The backings were fastened to one end of a 6.3 mm diameter copper rod of 17 cm length, the other end of the rod was maintained at 0 °C by an ice-water bath. With this system, the temperature of the target can be estimated as about 35P °C, where P is the total power

(in watts) dissipated by the beam in the target.

A standard quartz-crystal deposition monitor (made by the Sloan Instrument Corporation) was used to estimate when a desired target thickness had been attained. In the case of Al deposition, target thicknesses were repeatable to within 10-20% with this monitor, but for Mg deposition the initial results were erratic. It was found that evaporation of a few $\mu g/cm^2$ of gold on the quartz crystals completely alleviated these difficulties; apparently the magnesium was not adhering reliably to the quartz surface. Similar problems were present in the magnesium deposition on the copper blanks, but if the blanks were rubbed with emery paper just prior to pumping the vacuum, fairly uniform deposition was attained.

Transmission targets of the magnesium on thin (20 $\mu g/cm^2$) carbon foil backings were evaporated simultaneously with the copper-backed targets. To test for target oxidation, a 2 MeV alpha particle beam was scattered through the foil and the resulting scattered particles were studied with an Ortec surface barrier detector at 90^o to the beam. Analysis of the elastic scattering peaks (discussed in Appendix III) indicated that $N_O/N_{Mg} < 10\%$; of this contamination, some fraction will be in the form of a surface layer which does not affect thick target yield measurements. For the thick target strength analyses, a value of $N_O/N_{Mg} = 6 \pm 3\%$ was used for calculations of the atomic stopping cross sections.

Beam currents used varied from 2 - 6 μa of He^+ ions, the higher currents were used at the lower energies. The lower tem-

peratures at which the Mg targets were operated created much more serious carbon deposition problems than had been encountered for the Al targets. Bombardment of each target spot was limited to 3600 μC to reduce contamination problems; approximately 20 such spots were available per target blank.

An unusual problem encountered was the presence of 6 MeV radiation during bombardment. This radiation source was eliminated by 4" of lead shielding around the cross-field slits. Apparently residual hydrogen in the ion source was being accelerated down the beam tube, and as the mass 1 component was stopped in the preliminary mass analysis at the cross-field slits, the $^{19}F(p,\alpha'\gamma)^{16}O$ reaction was occurring on deposits near the slits.

B. Measurement of Yield Curve

Only one investigation of the $^{24}Mg(\alpha,\gamma)^{28}Si$ yield below 2.8 MeV has been published (Smulders and Endt, 1962). This group measured resonance energies and strengths for 15 resonances in this range; however, since (as will be discussed in the next chapter) there is considerable disagreement between the Utrecht measurements and our measurement of the $^{27}Al(p,\gamma)^{28}Si$ resonance strengths, it was considered worthwhile to remeasure the $^{24}Mg(\alpha,\gamma)^{28}Si$ strengths.

Resonances are sufficiently isolated for the $^{24}Mg(\alpha,\gamma)^{28}Si$ reaction that a fairly thick target could be used both to measure a yield curve and to measure thick target strengths. A yield curve was measured for the $^{24}Mg(\alpha,\gamma)^{28}Si$ reaction for E_α = 1.0 - 2.8 MeV on natural magnesium targets; integrated charge per point varied from

300 to 1500 μC. The yield was monitored by the single channel analyzer (SCA); the SCA counts, minus a room background (measured as in the $^{27}Al(p,\gamma)^{28}Si$ case), and corrected to 300 μC of charge per point, are displayed in figure 18. The lower bias of the SCA was set at 7.6 MeV for $E_\alpha < 2.0$ MeV; however, neutron induced pulses in the scintillation counters required that the lower bias level be raised to 8.9 Mev for $E_\alpha > 2.0$ MeV. (The neutron source was mainly the exoergic $^{13}C(\alpha,n)^{16}O$ reaction; the main source of background is neutron capture on ^{127}I which has a positive Q of 6.58 MeV. See, for example, Thompson, 1964.) To verify the identification of each resonance as arising from the ^{24}Mg in the target, each resonance was checked on a thin isotopic ^{24}Mg target. The yield curve shown in figure 18 is in good agreement with that of Smulders and Endt (1962) for $E_\alpha > 1.5$ Mev.

At $E_\alpha \approx 1.35$ MeV, the measured yield curve exhibited some structure which prompted a more careful study. The yields displayed in the inset of figure 18 were obtained for an integrated charge of 3600 μC per point, on both a thick natural Mg target and a thin (unfortunately rather non-uniform) isotopic ^{24}Mg target, suggesting the existence of a resonance in the $^{24}Mg(\alpha,\gamma)^{28}Si$ reaction. In addition, spectra were collected during these measurements; a total charge of 0.12 C was collected in an attempt to obtain a usable pulse height spectrum for this resonance. Even with a run of this length, few conclusions could be drawn concerning the decay of the resonance; however, further confirmation that the level was in ^{28}Si was provided

FIGURE 18: Yield Curve for the $^{24}Mg(\alpha,\gamma)^{28}Si$ Reaction

This figure shows the experimental yield curve measured for the $^{24}Mg(\alpha,\gamma)^{28}Si$ reaction in the energy range from 1.1 - 2.8 MeV. The energy scale has been adjusted so that energies coincide with resonance energies given by Endt and Van der Leun (1967). The quantity actually shown is the SCA counts obtained at each beam energy for an integrated charge of 300 μC. For $1.1 < E_\alpha < 2.0$ MeV, the SCA lower bias was set at 7.6 MeV. For $2.0 < E_\alpha < 2.8$ MeV, the SCA lower bias was set at 8.9 MeV. Room background has been subtracted from the points shown in the main figure. The inset shows a detailed study of the SCA counts for the region $1.33 < E_\alpha < 1.40$ MeV, without room background subtraction, for integrated charge of 3600 μC per point.

FIGURE 18

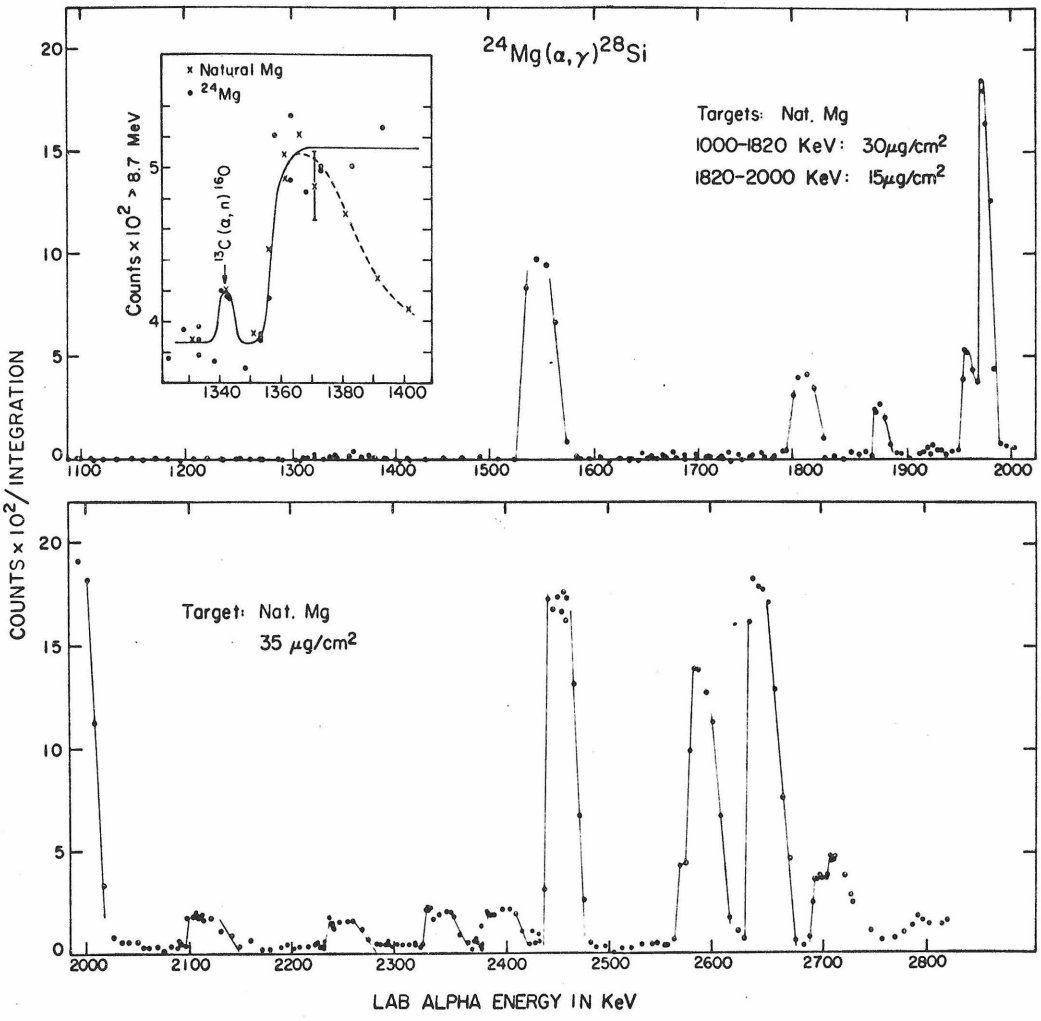
$^{24}Mg(\alpha,\gamma)^{28}Si$
Targets: Nat. Mg
1000-1820 KeV: 30μg/cm²
1820-2000 KeV: 15μg/cm²
× Natural Mg
• ^{24}Mg
Counts × 10² > 8.7 MeV
$^{13}C(\alpha,n)^{16}O$
Target: Nat. Mg
35 μg/cm²
COUNTS × 10²/INTEGRATION
LAB ALPHA ENERGY IN KeV

by the cutoff in the pulse height spectrum at the appropriate excitation energy. The small peak in the inset located 18 ± 5 keV below the resonance energy was identified as the 1.340 ± 0.004 MeV resonance in the reaction $^{13}C(\alpha,n)^{16}O$ (Ajzenberg-Selove and Lauritsen, 1959); this was verified by bombarding a tantalum target on which ^{13}C had been deposited (this target was provided by Dr. John Morris).

C. Resonance Parameters

As in the $^{27}Al(p,\gamma)^{28}Si$ case, a spectrum characteristic of each resonance was obtained by combining two spectra measured on the rapidly rising front edge of a thick target yield curve, the energies of the two runs usually differed by less than 3 keV. Neutron induced background in the spectra was of sufficient magnitude that pulse height spectra could not be extracted reliably below about 4 MeV. All resonance spectra were therefore analyzed with the η curves using either method 3, if an approximate decay scheme for the resonance was known, or method 4 of section IV.D. Approximate decay schemes were obtained mainly from the previous work by Smulders and Endt (1962); in some cases these authors had determined the dominant transitions, and in other cases, they had established correspondences to resonances in the $^{27}Al(p,\gamma)^{28}Si$ reaction (for which accurate decay schemes are known). The thick target yield N_γ^∞ was obtained by multiplying the step height in SCA counts by the factor N_γ/N_{SCA} obtained from the spectrum analysis. Equation 23 was then applied to N_γ^∞. These resonance strengths are given in table 3; the uncertainties listed were obtained from the following considerations. Resonance

energies are those given by Endt and Van der Leun (1967), since no special precautions were taken to measure absolute resonance energies. An exception is the 1.358 MeV resonance, for which the energy was measured relative to the neighboring $^{13}C(\alpha,n)^{16}O$ resonance (Ajzenberg-Selove and Lauritsen, 1959).

The atomic stopping cross section $\varepsilon(E)$ for the target was obtained from the equations given by Whaling (1958) for which he recommends an uncertainty of 20% for $E_\alpha < 2$ MeV; an uncertainty of 10% was assigned to $\varepsilon(E)$ for $E_\alpha > 2$ MeV. The isotopic composition of natural magnesium was taken as 78.7% ^{24}Mg. Uncertainty in the stopping cross sections due to target oxidation was negligible compared with these larger uncertainties.

Angular distributions had been measured in some cases by Smulders and Endt (1962) and corrections were applied in these cases. Reference to Section III.D should be made for detailed discussion of these corrections. An uncertainty of 10% was included on resonances for which angular distributions had not been measured.

Uncertainty in measurement of N_{SCA} on the thick target plateau was usually small relative to the larger uncertainties given above. Error in the determination of N_γ using the η curves was estimated at 15% in most cases since accurate branching ratios were not available (compare, for instance, table 2 which was applied in the $^{27}Al(p,\gamma)^{28}Si$ spectrum analyses).

The spectrum of the 1.358 MeV resonance showed a substantial γ_1 transition; this was determined by comparing the variation in

$N_i'(f)$ for this spectrum to the η curves of figure 14 ($N_i'(f)$ differs only by constants from $\eta(f)$; see equation 19).

Using subroutines written by Mrs. B. A. Zimmerman, the α-channel penetration factors P_ℓ were evaluated for the 1.358 MeV resonance. The Wigner single-particle width limits for Γ_α (discussed, for example, by Weidenmüller, 1964) were calculated from these P_ℓ; and, by comparison with the measured resonance strength for this resonance, it was determined that $\ell \leq 4$. For the spinless particles in this case $J = \ell$; therefore, $J \leq 4$, and $\pi = (-1)^J$ for the 1.358 MeV resonance.

In an attempt to obtain some information on radiative yield at lower energies, a very thick (stopping) target of natural magnesium was used; table 4 presents the data obtained at three bombarding energies. Only a room background, measured with the beam shut off, was subtracted from the SCA counts; this value is shown in the center column (per 10^{15} α). To obtain an upper limit, the uncertainty in the SCA counts of the center column was added to the measured SCA counts; this figure was converted to radiative yield by using the low extreme value of $\eta(f_b)$ from figure 14. The upper limit to radiative yield thus obtained has been converted to an upper limit on the sum of the resonance strengths for possible resonances below the bombarding energy and is given in the last column. This must be interpreted as a very generous upper limit since no correction for neutron induced SCA counts has been applied. Furthermore, at such low energies, $\ell = 0$ and $\ell = 1$ interactions would be anticipated, which

would populate only 0^+ and 1^- levels. Transitions from such levels would most probably be simple γ_1 cascades; however, the low extreme value of $\eta(f_b)$ used to obtain the upper limit is appropriate for very complex three-gamma cascades.

VIII. COMPARISON WITH OTHER RESONANCE STRENGTH MEASUREMENTS

As discussed in the introduction, one of the prime motivations for measuring resonance strengths in the $^{27}Al(p,\gamma)^{28}Si$ reaction below E_p = 1.4 MeV was to settle the discrepancies which exist in the literature between various groups. This chapter will attempt to shed light on the rather contradictory state of the current literature.

A. The $^{24}Mg(\alpha,\gamma)^{28}Si$ and $^{27}Al(p,\gamma)^{28}Si$ Reactions

Only one group (Smulders and Endt, 1962) has investigated the $^{24}Mg(\alpha,\gamma)^{28}Si$ reaction in the energy range covered in this work. The yield curve given in figure 18 is in good agreement with this group with the exception of the new resonance at 1.358 MeV. Resonance strengths given in table 3 are in good agreement with those given by Smulders and Endt; note, however, that the strengths listed in table 3 are given in the center-of-mass energy scale and should be scaled by the ratio 28/24 to compare with strengths given in the literature. The data given by Smulders and Endt were obtained by standard resonance yield techniques and had not been normalized to any other series of measurements.

The literature regarding the $^{27}Al(p,\gamma)^{28}Si$ reaction is not as simple to discuss; more than one type of measurement has been used, and much of the data are normalized, directly or indirectly, to other data.

For several resonances, table 5 presents a comparison of the strengths obtained in this work with strengths obtained by previous

investigators. The strengths quoted by the review article of Endt and Van der Leun (1967) are those of the two columns attributed to Nordhagen.

Table 5 illustrates several puzzling discrepancies. The results of this paper are in good agreement with the results of Nordhagen's Nuclear Physics papers (table 5 footnote b) and with the absolute measurements of Smith and Endt, and Luukko at the 774 keV resonance. However, Endt and Van der Leun (1962) refer to Nordhagen's unpublished work on the 774 and 1183 keV resonances (footnote g) as a correction to the value obtained by Smith and Endt for the 774 keV resonance. Adding to this difficulty is the statement by Nordhagen (1966) that his Nuclear Physics data (footnote b) (which are consistent with the present work) are based on a careful calibration at the 1183 keV resonance (footnote g) (which is definitely not consistent with this work).

Another discrepancy concerns the results at the very strong 1381 and 1388 keV resonances. The present paper is consistent with the data of Nordhagen (footnote h) and Gibson even though both of these authors normalize to 40 ev for the resonance strength at the 992 keV resonance (for which the present work gives 22.8 ev, in laboratory energy units). However, Gibson (footnote i) is in gross disagreement with Nordhagen (footnote b) at the strong 1317 and 1364 keV resonances, while the present paper agrees with Nordhagen at these resonances. The resonance strengths presented by Antoufiev at these resonances can not be reconciled with the data of any of the other investigators.

With one exception, the references listed in table 5 used con-

ventional resonance yield techniques, although their detection efficiencies were much lower than those used in the present work. Of these conventional yield measurements, NaI detectors were used by all except Gibson et al. (1968) (who used Ge(Li) detectors). The one exception is the work of Engelbertink and Endt (1966).

Perhaps the most crucial discrepancy, as mentioned in the introduction, is between the results of the present work (which agree with Smith and Endt, and Luukko), and the resonance strength obtained by Engelbertink and Endt for the 633 keV resonance (which agrees with Nordhagen's unpublished correction to Smith and Endt's work) based on a resonance absorption measurement in $^{30}Si(p,\gamma)^{31}P$.

Engelbertink and Endt (1966) bombarded a series of chemical compound targets. Using conventional thin target yield analysis, and relying on the stoichiometric ratios of the targets, they obtained relative resonance strengths in a variety of nuclei. These relative strengths were normalized by a resonance absorption measurement in $^{30}Si(p,\gamma)^{31}P$. While many of the nuclei they considered were used in several compounds, this was not the case for Al. The 633 keV resonance in the $^{27}Al(p,\gamma)^{28}Si$ reaction was tied into their network of inter-related strengths only by a single measurement on an Al_2Cl_6 target. If the stoichiometric ratio of Al_2Cl_6 had been altered during the target evaporation, this measurement would be invalid.

B. Comparison with Other Reactions

In an attempt to shed further light on the discrepancy with the resonance absorption measurements, the primary calibration resonance

of Engelbertink and Endt (1966) in the $^{30}Si(p,\gamma)^{31}P$ reaction was investigated with the thick target techniques discussed in section V.A. At the isotropic 622 keV resonance, a thick target yield was measured on a silicon target (89.1% ^{30}Si, obtained from Oak Ridge). The silicon was evaporated on a thin carbon foil, as well as on the tantalum target backings and the oxygen content was checked by elastic scattering of 2 MeV alpha particles through the carbon foil (this technique will be discussed in Appendix III); a small correction (~ 5%) was included in the final strength due to oxidation of the silicon target. The result obtained was $(2J+1)\Gamma_p\Gamma_\gamma/\Gamma = 3.93 \pm 0.40$ eV (on the lab energy scale). The resonance absorption value, based on a γ_0 branching ratio of 94% is 3.10 ± 0.26 eV (Smith and Endt, 1958).

The $^{26}Mg(p,\gamma)^{27}Al$ reaction at 1966 keV has also been investigated by resonance absorption techniques (Van der Leun and Jaspers, 1966). A thick target yield was studied using an evaporated magnesium target (99.7% ^{26}Mg, obtained from Oak Ridge). The oxygen content of the target was checked with neutron time-of-flight techniques against an oxidized tungsten target. (Both the ^{26}Mg target and oxygen analysis were provided by Mr. A. B. McDonald.) A small (~ 4%) correction was included in the final strength due to oxygen, and small angular distribution effects were allowed for. The final result was $(2J+1)\Gamma_p\Gamma_\gamma/\Gamma = 9.7 \pm 1.6$ eV (on the lab energy scale). The resonance absorption value is 6.4 ± 2.0 eV, based on a γ_0 branching ratio of 65% (Van der Leun and Jaspers, 1966; Van der Leun, Sheppard, and Endt, 1967).

These strength measurements of (p,γ) reactions on ^{30}Si and ^{26}Mg do not resolve the problems with the $^{27}Al(p,\gamma)^{28}Si$ strengths, and, in fact, may point to still other problems. Several important statements can be made using the above results.

1) The ratio of the $^{26}Mg(p,\gamma)^{27}Al$ and $^{30}Si(p,\gamma)^{31}P$ strengths measured in this work is consistent with the ratio of the strengths measured in the resonance absorption studies.

2) With regard to the $^{26}Mg(p,\gamma)^{27}Al$ and $^{30}Si(p,\gamma)^{31}P$ resonance yield measurements reported above, unknown impurities in a target can only lower strengths obtained with thick target yields, and the targets used were very nearly pure elemental targets. Yet the measurements of this paper are above the resonance absorption points and slightly outside the given uncertainties.

3) The present result for the ^{31}P resonance, used by Engelbertink and Endt as their normalization standard, is 27 ± 17% above that used by Engelbertink and Endt. However, the strength obtained here for the 633 keV resonance in the $^{27}Al(p,\gamma)^{28}Si$ reaction lies 42 ± 12% below that obtained by Engelbertink and Endt through the use of compound targets, using the resonance absorption result on ^{31}P as their absolute standard.

We are thus in serious disagreement with resonance strengths obtained by the group at Utrecht.

IX. INTERNAL CONSISTENCY TESTS

The preceding chapter gave a brief view of the confusing state of the current literature with regard to resonance strengths. The $^{24}Mg(\alpha,\gamma)^{28}Si$ strengths reported in this work are in reasonable agreement with the only data with which they can be compared. The $^{27}Al(p,\gamma)^{28}Si$ data are in agreement with some of the published strengths and in disagreement with other published values. In the course of the experimental program, particular attention was devoted to tests of the crucial parameters entering into the $^{27}Al(p,\gamma)^{28}Si$ strengths, and these tests are reported below. These tests greatly strengthen one's confidence in the strengths measured in this program.

All the resonance strengths reported in this work result either directly from thick target measurements, or from thin target yields normalized to thick target measurements. Equation 23 which was used for all thick target analyses shows that the resonance strengths are proportional to the atomic stopping cross section given by equation 24. In the Al data reduction, contaminants were assumed to be negligible, i.e., $n_i/n_{Al} \approx 0$; significant contamination of the Al targets would invalidate this procedure. To experimentally determine $\varepsilon(E)$, the following procedure was used: The integrated yield, Y, was measured for the 0.992 MeV resonance for several locations on a target of ~ 15 keV thickness for 1 MeV protons. Equation 27 demonstrated that if the surface density of target nuclei ($n_{Al}t$) is known, $\varepsilon(E)$ can be determined from the ratio of the integrated yield Y to the thick target

plateau height. (The target utilized was sufficiently thick that the plateau height was attained; for the 0.992 MeV resonance used, $\Gamma \approx 40$ eV.) A determination of the quantity $n_{Al}t$ was accomplished by measurement of the target area with a traveling stage microscope and by the determination of the total weight of Al on the target by a commercial laboratory (Truesdail Laboratories, Los Angeles). This laboratory stripped the Al from the Ta target backing in dilute HCl. The technique of atomic absorption spectrophotometry was then applied to deduce the total amount of Al present (to within 2% estimated standard deviation). From these data, the average value of $n_{Al}t$ was determined. Using this value of $n_{Al}t$, together with the averaged ratio of [Y/(thick target plateau height)], in equation 27 gave $\varepsilon(0.992 \text{ MeV}) = (7.90 \pm 0.40) \times 10^{-15}$ eV-cm^2. The value used in the data analysis, obtained from Whaling's tables (1958) for pure Al, was $\varepsilon(0.992 \text{ MeV}) = (7.88 \pm 0.55) \times 10^{-15}$ eV-cm^2, where the error here is the 7% rather arbitrarily assigned to the tabular data. This is taken as very strong evidence that contamination of the targets is not a serious problem here, and also that the value of $\varepsilon(E)$ for $E \approx 1$ MeV is correct. Furthermore, at higher energies $\varepsilon_{Al}(E)$ is very accurately known from Nielsen's (1961) work.

The uncertainty in the values of $\varepsilon(E)$ increases as E decreases. One check was made at the 0.633 MeV resonance to verify that $\varepsilon(0.992 \text{ MeV})/\varepsilon(0.633 \text{ MeV})$ agreed with the tables. The resonance strength of the 0.633 MeV resonance measured by thick target techniques was compared to the strength measured by thin target techniques through standardization to the 0.992 MeV resonance strength

(measured by thick target techniques). The two measurements of the 0.633 MeV resonance strength agreed well within their combined uncertainties, confirming that the ratio of $\varepsilon(E)$ values from Whaling's formula at 0.633 MeV and 0.992 MeV is correct to within 10%.

A further check was the comparison of resonance strengths determined by both thick and thin target techniques at 12 resonances above 1.4 MeV. In all cases, the agreement between the two determinations was well within the experimental uncertainties. This serves more as a test of the accuracy of the yield curve fitting procedure (discussed in Section VI.C), rather than of $\varepsilon(E)$, since the claimed uncertainty in $\varepsilon(E)$ is only about 3% for $E > 1.4$ MeV.

As a sensitive test of the accuracy of the determination of N_γ at the 0.992 MeV resonance, a very nearly direct comparison of the resonance strength was made to a calibrated ^{88}Y gamma ray source. For the 0.992 MeV resonance, 94% (Azuma, 1966; Boydell, 1967) of the radiative captures cascade through the 1.78 MeV first excited state of ^{28}Si. Nearly all (99.5%) of the ^{88}Y decays produce a 1.84 MeV gamma ray. A single 4" × 4" NaI crystal at 10 cm distance from the target at an angle of 55° with respect to the beam ($P_2(\cos 55^\circ) = 0$) was used to determine the 1.78 MeV photopeak counts. A slight correction was applied for a weak $P_4(\cos\theta)$ term in the angular distribution of the 1.78 MeV radiation (Antoufiev et al., 1964), and allowance was made for coincidence summing (i.e., transfer of a 1.78 MeV peak count out of the peak area due to interaction of another member of the cascade). The calibrated ^{88}Y source was used to determine the photopeak efficiency for 1.84 MeV gamma rays experi-

mentally; coincidence summing corrections were applied in this case as well. Both the total efficiency (using the theoretical attenuation coefficients for NaI) and the photofraction (using Heath's photofractions (1964) measured for a 7.6 cm diameter × 7.6 cm long NaI crystal as a guide) were corrected slightly for the difference between 1.78 and 1.84 MeV. The resulting resonance strength was 22.6 ± 2.7 eV. This value is in good agreement with the value given in table 1 measured by thick target analysis in the standard geometry. This provides further confirmation that the determination of N_γ is valid.

X. ASTROPHYSICAL RATES

A. Calculation of Interaction Rates

With the data obtained in this experimental program, summarized in tables 1 and 3, rate calculations were carried out. These data have been supplemented by cross sections measured by other authors outside the energy range studied in the current work.

The interaction rate, the product of cross section and velocity averaged over a normalized Maxwell-Boltzmann velocity distribution, for the reaction $A + B \rightarrow C + \gamma$, is given by:

$$\langle \sigma v \rangle^0 = \left(\frac{2\pi\hbar^2}{MkT}\right)^{3/2} \sum_r \frac{g_C^r}{g_A^0 g_B^0} \left(\frac{\Gamma_A \Gamma_\gamma}{\hbar\Gamma}\right)_r \exp(-E_r/kT)$$

$$+ \left(\frac{8}{\pi M}\right)^{1/2} (kT)^{-3/2} \int \sigma_{nr}(E) E \exp(-E/kT)\, dE \qquad (30)$$

where: $\langle \sigma v \rangle^0$ refers to the interaction rate for both nuclei A and B in their ground states only,

M = reduced mass of nuclei A and B,

$g_A^0 = (2J_A^0 + 1)$ for the ground state of nucleus A, similarly for g_B^0,

$g_C^r(\Gamma_A\Gamma_\gamma/\Gamma)_r$ = resonance strength for the r^{th} resonance in the given reaction, measured in center-of-mass energy units,

E_r = resonance energy for the r^{th} resonance, in CM energy units,

E = center-of-mass energy,

$\sigma_{nr}(E)$ = cross section for the radiative capture reaction.

Since total gamma ray widths Γ_γ are used above, contributions of excited states of nucleus C are included. The first term in equation 30 is the contribution from separate resonances; the second term is more convenient to apply when only $\sigma(E)$, rather than resonance parameters, is known, e.g., for nonresonant cross section data. Reference should be made to Appendix I for comments on the effect of induced emission on laboratory-measured radiative widths, references to the pertinent literature on astrophysical rates, and for discussion of the effects of excited states of A and B. These effects are not large for the ^{28}Si case, however, since even at $T_9 = 5$, 89% of the ^{27}Al and 83% of the ^{24}Mg are in their ground states.

B. Data Used for the ^{27}Al(p,γ)^{28}Si Rates

Chapter VI presented total resonance strengths and upper limits to nonresonant cross sections for the proton energy range 0.3 - 2.6 MeV. These data have been supplemented by data obtained by other investigators outside this energy range.

The tables of Endt and Van der Leun (1967) list three resonances below 0.3 MeV, these have been included in the rate calculations. Two groups have studied the reaction at higher energies, Gove *et al.* (1961) have obtained cross sections for the (p,γ_0) and (p,γ_1) reactions from $E_p = 3.8 - 10.4$ MeV. Singh *et al.* (1965) have measured the (p,γ_0), (p,γ_1) and (p,γ_{2+3}) cross sections from 4.0 - 12.5 MeV. In the region of overlap, the more detailed results of the latter paper were used.

In the energy range from 2.6 - 3.8 MeV, no (p_0,γ) data of

sufficient detail are available, and the following approximation was used. The data of table 1 below 2.6 MeV were averaged over 200 keV intervals and the average radiative capture cross sections thus obtained were compared to the data of Gove et al. (1961), and Singh et al. (1965) above 3.8 MeV. The energy-averaged total cross section in the region 2.2 - 2.6 MeV (~ 100 μb) was approximately the same as that above 3.8 MeV. A value of $\langle\sigma\rangle = 125 \pm 100$ μb was assumed for $E_p = 2.6 - 3.8$ MeV. A lower limit of $\langle\sigma\rangle \sim 25$ μb in this region was extracted by applying detailed balance to the (γ_0, p_0) bremsstrahlung data of Ullrich (1964). The uncertainty introduced in $\langle\sigma v\rangle^0$ by this approximation was 4.5% at $T_9 = 5$, and is quite negligible at lower temperatures. The upper limit to nonresonant yield from figure 17 was included in these calculations, but it contributed only 3% to the rate at $T_9 = 5$, and less at lower temperatures.

C. Data Used for the $^{24}Mg(\alpha,\gamma)^{28}Si$ Rates

Table 3 presented total resonance strengths for alpha particle energies below 2.8 MeV. Nonresonant data were not extracted due to the $^{13}C(\alpha,n)^{16}O$ background contamination. These data have been supplemented by data obtained by other investigators outside this energy range.

Data of Smulders and Endt (1962) were used for the alpha particle energy range 2.8 - 3.2 MeV. From $E_\alpha = 3.2 - 4.5$ MeV, only γ_0 and γ_1 data were available from the work of Weinman et al. (1964); no correction to their data was applied for $\gamma_{\geq 2}$ transitions. From $E_\alpha = 5.2 - 14.5$ MeV, γ_0 and γ_1 transitions have

been studied by Meyer-Schutzmeister et al. (1968); again no estimate for $\gamma_{\geq 2}$ transitions was included.

No (α_0,γ) data are available for E_α = 4.4 - 5.2 MeV, however, (γ_0,α_0) data are available from bremsstrahlung studies (Ullrich, 1964). These data were converted to the corresponding (α_0,γ_0) cross sections using detailed balance, and normalized to the data of Meyer-Schutzmeister et al. for $E_\alpha \geq 5.2$ MeV. By this process, (α_0,γ_0) data were obtained for E_α = 4.4 - 5.2 MeV. As an estimate of $\gamma_{\geq 1}$ transitions, the (α_0,γ_0) cross section obtained was doubled; thus $\langle\sigma\rangle_{\alpha_0\gamma} \approx 2\langle\sigma\rangle_{\alpha_0\gamma_0}$ was used.

The uncertainty in the total (α_0,γ) cross sections used above E_α = 3.2 MeV is considerable, however, the total uncertainty in this data does not carry over to the rate calculations. For T_9 = 2, 4, and 5, the resonances above 3.2 MeV contribute only 0.15%, 7%, and 14% to the total interaction rate, respectively. Furthermore, since the (γ,α) channel contributes only about 10% to the total ^{28}Si photodisintegration rate at T_9 = 5, these uncertainties are greatly reduced in significance if emphasis is on the photodisintegration rate.

D. Numerical Results for $\langle\sigma v\rangle^0$ and Empirical Fits

Numerical calculations of the interaction rate, multiplied by Avogadro's number, were made with the available data as discussed in the two preceding sections. Table 6 presents these numerical results at selected temperatures. For many applications, however, the numerical results are unnecessarily difficult to use, and semi-empirical fits to the rate data are more useful.

Various alternative forms for semi-empirical fits to $N_A\langle\sigma v\rangle$ have been tried by Fowler, Caughlan, and Zimmerman (1967, henceforth denoted by FCZ), who found that the form $\langle\sigma v\rangle = A \exp(-E_{th}/kT)$ yields the best fits for $T_9 \geq 1$. Such a functional form implies a $\sigma(E) \propto (E-E_{th})^{1/2}/E$ for $E \geq E_{th}$, and $\sigma(E) = 0$ for $E < E_{th}$; i.e., a cross section which has a threshold at E_{th}, above which it rises approximately as the velocity of the incident particle. At high energies, this form implies $\sigma(E) \propto \lambda\!\!\!^{-2}$ (i.e., $(2J_r+1)\Gamma_p\Gamma_\gamma/\Gamma \approx$ constant). An approximate definition of E_{th} is the bombarding energy at which $\Gamma_p \approx \Gamma_\gamma$; thus for $E > E_{th}$, $\Gamma_p\Gamma_\gamma/\Gamma \approx \Gamma_\gamma$. From this discussion, it is obvious that this function form for $\langle\sigma v\rangle$ will not be adequate at lower temperatures where the effective interaction energy E_0 (equation 2) is less than E_{th}; i.e., where penetration effects on Γ_p are still dominant.

A least squares fit to the data of table 6 for $T_9 = 1.0 - 5.0$ using the form of FCZ, gave for the $^{27}Al(p,\gamma)^{28}Si$ interaction rate:

$$N_A\langle\sigma v\rangle^0 = 8.19 \times 10^4 \exp(-6.342/T_9) \ .$$

This expression fits the data of table 6 with a maximum deviation of 14% over the range $T_9 = 1.0 - 5.0$, but at $T_9 = 0.5$, this fit is about a factor of 8 below the numerical results of table 6.

For the $^{24}Mg(\alpha,\gamma)^{28}Si$ reaction, the best fit for the range $T_9 = 1.0 - 5.0$ was given by

$$N_A\langle\sigma v\rangle^0 = 1.85 \times 10^3 \exp(-15.163/T_9)$$

which fits the data of table 6 with a maximum deviation of 26% over

this temperature range. At $T_9 = 0.5$, this fit is about a factor of 4 below the data of table 6.

One possibility for decreasing the maximum deviation of these fits, and extending their usefulness to lower temperatures (for application to processes other than silicon-burning) would involve an attempt to account for effects due to resonances below E_{th} by a single resonance with resonance energy below E_{th}. This has the effect of increasing the available parameters to four by adding a term $CT^{-3/2}\exp -D/T$ to the form used by FCZ (cf. equation 30). For the $^{27}Al(p,\gamma)^{28}Si$ case, a search was made for such four parameter fits and good fits were obtained over the range $T_9 = 0.5 - 5.0$. However, four parameters fits of the simpler form A exp -B/T + C exp -D/T were also attempted and this simpler form yielded even better fits. This form was then applied to the two reactions of interest here.

For the $^{27}Al(p,\gamma)^{28}Si$ case, the form

$$N_A\langle \sigma v\rangle^0 = 9.16 \times 10^4 \exp(-7.305/T_9) + 4.61 \times 10^3 \exp(-3.857/T_9)$$

fits the data of table 6 with a maximum deviation of 5% over the range $T_9 = 0.5 - 5.0$. Of course, the data of table 6 have a standard deviation of the order of 15 - 20% arising from uncertainties in the resonance data of table 1 and the approximations discussed in section IX.B.

For the $^{24}Mg(\alpha,\gamma)^{28}Si$ case, the form obtained was

$$N_A\langle \sigma v\rangle^0 = 3.39 \times 10^3 \exp(-19.575/T_9) + 6.21 \times 10^2 \exp(-13.863/T_9)$$

which fits the data of table 6 with a maximum deviation of 9% for

$T_9 = 0.5 - 5.0$. Again, this is well within the uncertainties in the rates of table 6 which, in light of the approximations of section IX.C and the uncertainties in the data of table 3, are of the order of 25 - 30%.

E. Photodisintegration Rates

Appendix I demonstrates that the $\lambda_{\gamma A_0}$ photodisintegration rate is given by:

$$\lambda_{\gamma A_0} = \frac{g_A^0 g_B^0}{G_C} \left(\frac{MkT}{2\pi\hbar^2}\right)^{3/2} \langle \sigma v \rangle^0 \exp(-Q/kT) \tag{31}$$

where $\lambda_{\gamma A_0}$ refers to photodisintegration of nucleus C through the (γ, A_0) channel. The notation is the same as that of equation 30. In equation 31, the partition function G is given by

$$G_C = \sum_{i=0} (2J_i(C)+1)\exp(-E_i(C)/kT) \tag{32}$$

where $J_i(C)$ and $E_i(C)$ are the spin and excitation energy of the i^{th} state of nucleus C.

The total photodisintegration rate must include contributions from the (γ, p_0), (γ, p_1), etc., channels; in general

$$\lambda_\gamma = \lambda_{\gamma p_0} + \lambda_{\gamma \alpha_0} + \sum_{i \geq 1} (\lambda_{\gamma p_i} + \lambda_{\gamma \alpha_i}) \ . \tag{33}$$

Data are available only for calculation of the first two terms of equation 33, but Appendix I will discuss the approximate contribution of the third term to λ_γ.

Using equation 31, $\lambda_{\gamma p_0}$ and $\lambda_{\gamma \alpha_0}$ have been calculated for

several temperatures and are given in table 7. The semi-empirical fits to $N_A\langle\sigma v\rangle^0$ given in the preceding section may be inserted in equation 31 to give corresponding functional forms of $\lambda_{\gamma A_0}$. The quantity $(MkT/2\pi\hbar^2)^{3/2} = 0.98677 \times 10^{10}(A_A A_B/A_C)^{3/2} T_9^{3/2} N_A$, where A_A is the mass number of nucleus A, etc. Numerically, $g_p = 2$, $g_\alpha = 1$, $g^0_{Al} = 6$, $g^0_{Mg} = 1$, $G(^{28}Si) \approx 1 + 5\exp(-20.642/T_9)$, and $1/kT = 11.605/T_9$.

XI. SUMMARY

The two goals of the current experimental program have been accomplished. A NaI spectrometer yielding very high detection efficiencies has been built and carefully calibrated. The partial detection efficiency (η) curves are applicable to reactions other than the two considered here; they should be useful for other reactions involving excitation energies of roughly the same magnitude as considered in the ^{28}Si nucleus. This spectrometer and the η curves will be applied to a study of the resonance strengths for the (p,γ) and (α,γ) reactions leading to ^{24}Mg. Even for reactions whose Q is much lower, the spectrometer will be useful. In these cases, the partial detection efficiency curves of figure 14 should not be used, but the experimentally determined total detection efficiencies and monochromatic line shapes may be applied in many cases.

Tables 1 and 3 summarize the resonance parameters determined in this experimental program for the ^{27}Al$(p,\gamma)^{28}$Si and ^{24}Mg$(\alpha,\gamma)^{28}$Si reactions. Strengths were determined for a total of 101 resonances in these two reactions. Particular attention has been given to tests of internal consistency to demonstrate that the detection efficiencies and target purity assumed in the ^{27}Al$(p,\gamma)^{28}$Si data analysis were correct.

Interaction rates and photodisintegration rates have been calculated from the data obtained in this work and are given in tables 6 and 7. In the case of ^{28}Si, photodisintegration to excited states of ^{27}Al and ^{24}Mg is not expected to be a large correction (as discussed

in Appendix I); however, the ^{24}Mg photodisintegration rate (which is the dominant rate determining mechanism in silicon-burning) may be more strongly influenced by photodisintegration proceeding to excited states of ^{23}Na and ^{20}Ne. As discussed in the introduction, $\lambda_\gamma(^{28}\text{Si})$ is now understood to be of secondary importance in silicon-burning calculations; thus any re-evaluation of these calculations should await completion of the ^{24}Mg case.

APPENDIX I. DERIVATIONS OF ASTROPHYSICAL RATES

The determination of astrophysical reaction rates from experimentally measured parameters has been considered by many authors, and several excellent discussions exist, for example: Fowler and Vogl (1964); Fowler and Hoyle (1964); Clayton (Chapter IV, 1968); Fowler, Caughlan, and Zimmerman (1967, referred to as FCZ).

This Appendix can not treat this extensive subject in any comprehensive fashion, and reference to FCZ (which is an excellent general review article) will be made at several points. Three areas will be considered. 1) The formulae given by FCZ and used in chapter X for the rate calculations neglect induced emission; this is considered further here. 2) The derivation of Fowler and Hoyle (1964) regarding effects of excited states in the ^{28}Si nucleus will be sketched. 3) The general equations for interaction and photodisintegration rates including effects of excited states in the ^{27}Al or ^{24}Mg nuclei will be given; comments on the probable importance of such effects are also given.

A. Photodisintegration rate for a single level

Photodisintegration rates may be calculated from a thermodynamic argument or a more detailed, brute force, calculation. Both methods are outlined here.

In thermodynamic equilibrium, every rate is balanced by its inverse. Consider the rate for the reaction $A + B \rightarrow C^* + \gamma$, where C^* refers to an excited state of nucleus C at energy E_C^*, A and B are

assumed to be in their ground states.[1] If n_A denotes the equilibrium number density of nucleus A in the ground state, and similarly for n_B and n_{C^*}, we have

$$n_{C^*}\lambda_\gamma(C^*) = n_A n_B \langle \sigma v \rangle^*_{AB} \tag{34}$$

where $\langle \sigma v \rangle^*_{AB}$ is the interaction rate for nuclei A and B to produce the C^* state (cf. FCZ equation 32, also given as the second term of equation 30) and $\lambda_\gamma(C^*)$ is the photodisintegration rate for nucleus C in the C^* state. At equilibrium, as assumed here, the number densities of the three constituents are related by the Saha equation (cf. Clayton, p. 29, 1968; FCZ equation 18); although this equation was originally derived to relate number densities of various atomic ionization states, it is equally applicable to the "nuclear ionization" phenomena under consideration. Application of the Saha equation yields (cf. equation 30 for notation):

$$\lambda_\gamma(C^*) = \left(\frac{MkT}{2\pi\hbar^2}\right)^{3/2} \frac{g^0_A g^0_B}{g^*_C} \exp\left[-(Q-E^*_C)/kt\right] \langle \sigma v \rangle^*_{AB} \tag{35}$$

where $Q-E^*_C$ is the energy release in the reaction $A + B \rightarrow C^* + \gamma$. For the present derivation, a single Breit-Wigner resonance (equation 21) may be assumed for $\sigma^*(E)$, however, the value of Γ^*_γ used in this expression must be modified. (Γ^*_γ is the radiative width for the given resonance, determined under laboratory conditions, for transition from the resonance level C^r to the C^* level.) Emission induced by

---

[1] In this appendix, a superscript asterisk will denote excited states of C while superscript numbers will refer to excited states of B.

the presence of the black body Planck radiation in the stellar environment must be considered in addition to the spontaneous emission width measured in the laboratory. The Einstein coefficients (Clayton, p. 28, 1968) relate the probability of spontaneous emission $A_{r\rightarrow *}$ ($A_{r\rightarrow *} \propto \Gamma^*_\gamma$) to the probability for induced emission $B_{r\rightarrow *} n_\gamma(\nu)$, where $n_\gamma(\nu)$ is the photon number density (Planck distribution):

$$B_{r\rightarrow *} n_\gamma(\nu) = \frac{A_{r\rightarrow *}}{e^{h\nu/kT} - 1} \tag{36}$$

$n_\gamma(\nu)$ is to be evaluated at $\nu = (E^r_C - E^*_C + Q)/h$.

Equation 30 gives the result of integration of $\langle \sigma v \rangle$ for a single resonance with Breit-Wigner parameters Γ_A, Γ_γ, and Γ; including the induced contribution to Γ_γ and Γ, equation 30 becomes

$$\langle \sigma v \rangle^*_{AB} = \left(\frac{2\pi\hbar^2}{MkT}\right)^{3/2} \frac{g^r_C}{g^0_A g^0_B \hbar} \frac{\Gamma_A \Gamma^*_\gamma \left[1 + \frac{1}{e^{h\nu/kT} - 1}\right]}{\Gamma + \frac{\Gamma_\gamma}{e^{h\nu/kT} - 1}} \exp - E^r_C/kT \tag{37}$$

or using (35)

$$\lambda_\gamma(C^*) = \frac{1}{\hbar} \frac{g^r_C}{g^*_C} \frac{\Gamma_A \Gamma^*_\gamma (1 - e^{-h\nu/kT})^{-1}}{\Gamma\left[1 + \frac{\Gamma_\gamma}{\Gamma}(e^{h\nu/kT} - 1)^{-1}\right]} \exp(-Q + E^*_C - E^r_C)/kT \tag{38}$$

Even at $T_9 = 5$, where $kT = 0.43$ MeV, the terms arising from induced emission are negligible for the nuclei of interest here. For ^{28}Si, virtually all transitions are to states below 7 MeV in excitation energy; for such transitions $h\nu/kT > 9$, thus (38) becomes:

$$\lambda_\gamma(C^*) = \frac{g_C^r}{g_C^*} \frac{\Gamma_A \Gamma_\gamma^*}{\hbar\Gamma} \exp(-Q + E_C^* - E_C^r)/kT \qquad (39)$$

An interesting exercise is to derive (38) from a "brute force" standpoint, without appealing directly to the Saha equilibrium equation; indirectly, of course, the Saha equilibrium equation is intimately related to the Planck distribution.

The photodisintegration rate is given by:

$$\lambda_\gamma(C^*) = c\int_0^\infty \sigma_{C^*+\gamma\rightarrow A+B}(h\nu) n_\gamma(\nu)\, d\nu \qquad (40)$$

where $n_\gamma(\nu)$, the Planck distribution, is

$$n_\gamma(\nu) = \frac{8\pi h}{(hc)^3} \frac{(h\nu)^2}{e^{h\nu/kT} - 1} \qquad (41)$$

and $\sigma(h\nu)$ is a single Breit-Wigner resonance,

$$\sigma_{C^*+\gamma\rightarrow A+B}(h\nu) = \pi\lambda_\gamma^2 \frac{g_C^r}{2g_C^*} \frac{\Gamma_\gamma^* \Gamma_A}{(E_\gamma - E_C^r - Q + E_C^*)^2 + \Gamma'^2/4} \qquad (42)$$

where $\Gamma' = \Gamma + \Gamma_\gamma(e^{h\nu/kT} - 1)^{-1}$ from the induced emission effects. For a narrow resonance, $n_\gamma(\nu)$ may be removed from the integral of (40); the integration of (40) may then be accomplished to yield (38).

It may be noted that (39) is obtained most simply if a Boltzmann-like distribution is used for $n_\gamma(\nu)$ (i.e., ignoring the -1 in the denominator of (41)). This is not surprising since Clayton (p. 26) shows that if induced emission is neglected, a Boltzmann-like distri-

bution for $n_\gamma(\nu)$ is consistent with a Maxwell-Boltzmann distribution for excited states of a system.

B. Photodisintegration Rate for a Realistic Nucleus

Equation 39 was derived for photodisintegration from a single excited state of nucleus C, C^*, through a single resonance at E_C^r. If many resonances contribute to $\lambda_\gamma(C^*)$, the rate may be obtained simply by summing over the contributions of the individual resonances. For this, more realistic, case:

$$\lambda_\gamma(C^*) = \frac{1}{g_C^*} \sum_r g_C^r \left.\frac{\Gamma_A \Gamma_\gamma^*}{\hbar\Gamma}\right)_r \exp(-Q - E_C^r + E_C^*)/kT \qquad (43)$$

If the distribution among excited states C^* can be described by an equilibrium distribution, the occupation probability of state C^* is

$$P(C^*) = \frac{g_C^*}{G_C} \exp -E_C^*/kT \qquad (44)$$

where G_C is the partition function for nucleus C given in equation 32. The total photodisintegration rate of the nucleus, <u>to the ground states of nuclei A and B</u>, is:

$$\lambda_{\gamma A_0} = \sum_* P(C^*)\lambda_\gamma(C^*) \qquad (45a)$$

$$= \sum_{*,r} \frac{g_C^r}{G_C} \left.\frac{\Gamma_A \Gamma_\gamma^*}{\hbar\Gamma}\right)_r \exp(-Q - E_C^r)/kT \qquad (45b)$$

$$= \frac{1}{\hbar G_C} \sum_r g_C^r \left.\frac{\Gamma_A \Gamma_\gamma}{\Gamma}\right)_r \exp(-Q - E_C^r)/kT \qquad (45c)$$

where the last step required $\sum_{*} \Gamma^{*}_{\gamma,r} = \Gamma_{\gamma,r}$; i.e., the total radiative width of the resonant level r. Note that this simple expression arose because the enhanced probability of finding the lower energy gamma ray required for photodisintegration from an excited state was balanced by the decreased probability of finding the excited state occupied. Equation 31 follows either from comparing the resonant contribution of equation 30 to (45c), or more directly from (35).

The assumption of equilibrium among the excited states of C should be valid if the photoexcitation lifetime for the states C^* is much less than the time scale for the astrophysical process under consideration, (cf. FCZ). The spontaneous decay lifetimes $\tau_{sp}(C^*)$ have been measured for many ^{28}Si levels (Gibson et al., 1968) and using FCZ equation 11, for $E^i_C < E^*_C$,

$$\tau(C^i \rightarrow C^*) = \frac{g^i_C}{g^*_C} \tau_{sp}(C^* \rightarrow C^i)[\exp(E^*_C - E^i_C)/kT - 1]. \qquad (46)$$

The photoexcitation lifetimes for transitions to the lower states were calculated and compared to $1/\lambda_{\gamma p_0 + \alpha_0}(^{28}Si)$ (cf. table 7). Such a comparison is shown in table 8. Since the $^{24}Mg + \alpha \rightleftharpoons \gamma + {}^{28}Si$ equilibrium considerably increases the time scale over $1/\lambda_{\gamma}(^{28}Si)$, this is a very generous comparison. From table 8, it is seen that the equilibrium assumption is excellent for all levels of interest.

C. Effects of Excited States on Astrophysical Rates

The effects of excited states in the ^{28}Si nucleus were easily accounted for in the preceding section. (For this section, the general

notation A, B, and C will be abandoned and specialized to the ^{28}Si case). However, the effects of photodisintegration to the p_1 or α_1 channels are very difficult to calculate, although formally they are easily inserted. The derivation of (45c) could be repeated, but as is easily anticipated, one obtains

$$\lambda_{\gamma p}(^{28}Si) = \frac{1}{\hbar G_{Si}} \sum_r g^r_{Si} \left(\frac{\left(\sum_i \Gamma_{p_i}\right)\Gamma_\gamma}{\Gamma} \right)_r \exp\,(-Q - E^r)/kT \qquad (47)$$

where E^r continues to refer to the resonance energy which would be measured for the p_0 channel. Of course, $\Gamma_{p_i} \equiv 0$ until $E^r > E_i(^{27}Al)$.

The complete interaction rate may also be formally written down. If $P(^{27}Al^i)$ is the occupation probability for the i^{th} state of ^{27}Al, and $\langle \sigma v \rangle^i_{p\gamma}$ is the interaction rate for ^{27}Al in its i^{th} excited state, we have

$$\langle \sigma v \rangle_{p\gamma} = \sum_i P(^{27}Al^i) \langle \sigma v \rangle^i_{p\gamma} \qquad (48a)$$

$$= \frac{1}{G_{Al}} \sum_i g^i_{Al} \exp - E_i(^{27}Al)/kT \langle \sigma v \rangle^i_{p\gamma} \qquad (48b)$$

and in analogy with equation 30:

$$\langle \sigma v \rangle^i_{p\gamma} = \left(\frac{2\pi\hbar^2}{MkT}\right)^{3/2} \sum_r \frac{g^r_{Si}}{g_p g^i_{Al}} \left(\frac{\Gamma_{p_i}\Gamma_\gamma}{\hbar\Gamma} \right)_r \exp - (E^r - E_i(^{27}Al))/kT \qquad (49)$$

or, inserting (49) in (48b),

$$\langle \sigma v \rangle_{p\gamma} = \frac{1}{G_{Al} g_p} \left(\frac{2\pi\hbar^2}{MkT}\right)^{3/2} \sum_r g^r_{Si} \left(\frac{\left(\sum_i \Gamma_{p_i}\right)\Gamma_\gamma}{\hbar\Gamma} \right)_r \exp - E^r/kT \qquad (50)$$

and from equations 50 and 47, the extremely useful relation

$$\lambda_{\gamma p}(^{28}\mathrm{Si}) = \frac{G_{\mathrm{Al}} g_p}{G_{\mathrm{Si}}} \left(\frac{MkT}{2\pi\hbar^2} \right)^{3/2} \exp - Q/kT \langle \sigma v \rangle_{p\gamma} \qquad (51)$$

is obtained. If the proton had low-lying states, g_p would be replaced by G_p. Equation 51 follows more directly from equation 35. Equations like 47-51 may also be written for the $^{24}\mathrm{Mg} + \alpha$ case.

Data are not available for a complete calculation of $\lambda_{\gamma p}$ or $\langle \sigma v \rangle_{p\gamma}$; the ratios $\Gamma_{p_i}/\Gamma_{p_0}$ would be required for all resonances. Even such knowledge does not guarantee a correct treatment since it is conceivable that some resonances would be so weak in a p_0-induced reaction that they would not be observed; furthermore, if $\Gamma_{p_i}/\Gamma_{p_0} \gg 1$, such p_i resonances could be quite important in the total rates. Similar comments apply to $\langle \sigma v \rangle_{\alpha\gamma}$.

Bahcall and Fowler (1969) have considered the effect of excited states in what they have called the equal strength approximation; the result of their calculation is $\langle \sigma v \rangle^i \approx \text{const} \approx \langle \sigma v \rangle^0$. An assumption made in their work is that the ratio of the outgoing width to the total width is approximately constant, an assumption which is invalid in the case of the radiative capture reactions under study here, since for low p_0 energies, $\Gamma \approx \Gamma_\gamma$, and for low p_1 energies, $\Gamma \approx \Gamma_{p_0} \gtrsim \Gamma_\gamma$. Another, more complicated, approach to estimating the reaction rates is outlined by Truran et al. (1966a) which, however, includes only E1 radiative transi-

tions and probably would have to be expanded to include E2 and M1 contributions before it would be completely valid. An estimate of the importance of excited state channels was made with an approach somewhat similar to that adopted by Truran et al. (1966a); this calculation will now be discussed.

The use of optical model transmission functions in determinations of average cross sections has been summarized by Vogt (1969), who shows that the relation

$$T_c^{J^\pi} = 2\pi \frac{\langle \Gamma_c \rangle^{J^\pi}}{D^{J^\pi}} \tag{52}$$

is valid for $T_c \ll 1$, where $T_c^{J^\pi}$ is the transmission function for channel c. $\langle \Gamma_c \rangle^{J^\pi}$ is the average resonance width for channel c for levels of spin and parity J^π; and D^{J^π} is the average spacing of compound nucleus states of a given J^π. T_c, $\langle \Gamma \rangle$, and D are functions of excitation energy. The condition $T_c \ll 1$ is not always satisfied in what follows, but Vogt points out that relation 52 is still a reasonable estimate even for $T_c \approx 1$. Following Vogt, the average cross section for a channel c of the reaction $0 + 1 \rightarrow 2 + \gamma$, is given by

$$\langle \sigma \rangle_{c\gamma} = 2\pi^2 \lambda_c^2 \sum_{J^\pi} \frac{(2J+1)}{(2J_0^c+1)(2J_1^c+1)} \frac{\langle \Gamma_c \rangle^{J^\pi} \langle \Gamma_\gamma \rangle^{J^\pi}}{D^{J^\pi} \left[\sum_{c'} \langle \Gamma_{c'} \rangle^{J^\pi} + \langle \Gamma_\gamma \rangle^{J^\pi} \right]} \tag{53}$$

where the channel c denotes a particular state of nuclei 0 and 1, such as the p_0 or p_1 channels, for example. The summation in the denominator of (53) is to be carried out over all interaction channels

open at a given excitation energy. In the notation of (52)

$$\langle \sigma \rangle_{c\gamma} = 2\pi^2 \lambda_c^2 \sum_{J^\pi} \frac{(2J+1)}{(2J_0^c+1)(2J_1^c+1)} \frac{T_c^{J^\pi} \langle \Gamma_\gamma \rangle^{J^\pi}}{D^{J^\pi} \left[\sum_{c'} T_{c'}^{J^\pi} + \frac{2\pi \langle \Gamma_\gamma \rangle^{J^\pi}}{D^{J^\pi}} \right]} \tag{54}$$

This $\langle \sigma \rangle_{c\gamma}$ (which is a function of excitation energy) may be inserted in the second term of (30) to allow the determination of $\langle \sigma v \rangle_{c\gamma}$.

For greatest accuracy, the transmission functions should be calculated from a realistic optical model potential $V(r)$, employing a diffuse-edge nuclear potential, such as a Saxon-Woods shape,

$$V(r) = \frac{V_o + iW_o}{1 + e^{(r-R_o)/a}} \tag{55}$$

where W_o is the absorptive potential. Such calculations are discussed by Vogt (1969) in several special cases. However, the time-consuming calculation of optical model transmission functions is not necessary for a rough estimate of excited state effects; and, in any case, there is no guarantee that optical model parameters known from elastic scattering data would be applicable to excited state calculations.

If the nucleus is assumed to be a "black" square well of depth V_o, i.e., interior to the nuclear radius R_c only incoming waves exist, the transmission function, for given angular momentum ℓ, can be written in closed form:

$$T_c^{\ell} = \frac{4KR_c P_{\ell}}{S_{\ell}^2 + (KR_c + P_{\ell})^2} \tag{56}$$

where

$$K = \sqrt{\frac{2M(V_o + E)}{\hbar^2}} \tag{57}$$

P_{ℓ} and S_{ℓ} are the familiar penetration and shift functions

$$P_{\ell} = kR_c / [F_{\ell}^2(kR_c) + G_{\ell}^2(kR_c)] \tag{58a}$$

$$S_{\ell} = \frac{kR_c}{2} \left[\frac{d}{d(kr)} \left\{ \ln [F_{\ell}^2(kr) + G_{\ell}^2(kr)] \right\} \right]_{kr = kR_c} \tag{58b}$$

where F_{ℓ} and G_{ℓ} are the regular and irregular Coulomb functions, $k = \sqrt{2ME/\hbar^2}$, M is the reduced mass of nuclei 0 and 1, and E is the center of mass energy of nuclei 0 and 1. The transmission functions defined in (56) depend only on ℓ since no J-dependent forces were assumed. The transmission functions of (52) are obtained from (56) by

$$T_c^{J^{\pi}} = \sum_{s,\ell} T_c^{\ell} \tag{59}$$

where the summation indices range over all channel spins s and angular momenta ℓ consistent with the given J^{π}.

As is well known, charged particle transmission functions are sensitive to nuclear radius and potential shape. Vogt (1962) and Vogt, Michaud, and Reeves (1965) have discussed the unphysical reflection which occurs when a square well potential is assumed rather than the

potential shape of (55). They showed that a square well, of radius $R_o + \Delta R$, (cf. equation 55) could be defined which would duplicate the properties of a diffuse edge potential, if all penetrabilities were scaled by a reflection factor f. Vogt et al. (1965) gave a series of graphs from which ΔR and f could be determined for a given V_o, R_o and a. The procedure followed in the present calculation was to calculate transmission functions from (56) with the replacement of P_ℓ by fP_ℓ; R_c was taken as $R_o + \Delta R$.

The nuclear level density was taken from the extensive compilation of Gilbert and Cameron (1965) who used the expression, at high excitation energies E_x,

$$\rho(J^\pi, U) = \left[D^{J^\pi}(E_x)\right]^{-1} = \frac{1}{48\sqrt{2}} \frac{e^{2\sqrt{aU}}}{U(aU)^{1/4}} \frac{(2J+1)e^{-(2J+1)^2/8\sigma^2}}{\sigma^3} \qquad (60)$$

where, for ^{28}Si, $a = 3.05\ (MeV)^{-1}$, $\sigma = 2.0$, and $U = E_x - 3.89$ MeV. Reference to Gilbert and Cameron (1965) should be made for details.

$\langle \Gamma_\gamma \rangle^{J^\pi}$ was taken as a constant independent of J^π and excitation energy. In the limit of numerous final states of all spin and parity combinations, approximate independence of J^π would be expected. Since ^{28}Si has few low-lying states, this is only a rough approximation in this case. At the high excitation energies of interest here, independence of E_x is a good assumption. It is primarily on these points that the present treatment differs from the work of Truran (1966a). Truran considered $\langle \Gamma_\gamma \rangle^{J^\pi}$ to be a function of both J^π and E_x; he used level density formulae for the final states to calcu-

late average E1 transition rates. (The author gratefully acknowledges many discussions with Dr. J. W. Truran in connection with such calculations of reaction rates.)

A computer code was written for the IBM 360/75 which used $\langle\sigma\rangle_c$ from (54) to calculate $N_A\langle\sigma v\rangle_{c\gamma}$ from (30). Five channels were considered: p_0, p_1, p_2, α_0, α_1. Nuclear radii were taken from Vogt (1969) for proton channels ($R_o = 1.25\ A^{1/3}$, a = 0.5 fermi) and from Rost (1962) for alpha channels (R_o = 4.76 fermi, a = 0.55 fermi). The real potential well depth V_o was taken as 55 MeV for the proton channels (Vogt, 1969) and 48 MeV for the alpha channels (Rost, 1962). Values of f and ΔR obtained from Vogt et al. (1965) were

$$\Delta R^p = 0.06 \text{ fermi} \qquad f^p = 2.5$$

$$\Delta R^\alpha = 0.67 \text{ fermi} \qquad f^\alpha = 4.6$$

The transmission functions T_c^ℓ calculated from these parameters were converted to $T_c^{J^\pi}$ with the use of equation 59. The program considered $J \leq 8$, $\pi = \pm$ and performed the required integrations as sums over an energy grid. $\langle\Gamma_\gamma\rangle$ was varied to fit $N_A\langle\sigma v\rangle_{p_0\gamma}$ from table 6 at $T_9 = 5$; $\langle\Gamma_\gamma\rangle = 1.2$ eV was used.

Table 9 summarizes the results of this program, both the calculated values of $N_A\langle\sigma v\rangle_{p_0\gamma}$ and $N_A\langle\sigma v\rangle_{\alpha_0\gamma}$ are given, as well as the ratios of $\langle\sigma v\rangle_{p_1\gamma}/\langle\sigma v\rangle_{p_0\gamma}$, $\langle\sigma v\rangle_{p_2\gamma}/\langle\sigma v\rangle_{p_0\gamma}$ and $\langle\sigma v\rangle_{\alpha_1\gamma}/\langle\sigma v\rangle_{\alpha_0\gamma}$. It should be stressed that the ratios of $\langle\sigma v\rangle$'s are more likely to be correct than the absolute values of the $\langle\sigma v\rangle$'s. Such ratios will, to at least some extent, cancel out errors in the choice of channel radii

and other parameters. Table 9 also lists the experimental values of $N_A\langle\sigma v\rangle_{p_0\gamma}$ and $N_A\langle\sigma v\rangle_{\alpha_0\gamma}$ from table 6. It is most gratifying to note that the calculations reproduce the experimental values within a factor of 5, over the seven decades spanned by $N_A\langle\sigma v\rangle_{\alpha_0\gamma}$ and the three decades spanned by $N_A\langle\sigma v\rangle_{p_0\gamma}$.

As would be expected from the previous discussion, the approximation $\langle\sigma v\rangle^e \approx \langle\sigma v\rangle^g$ does not agree with the present calculation. The very low values for $\langle\sigma v\rangle_{\alpha_1\gamma}/\langle\sigma v\rangle_{\alpha_0\gamma}$ result from the p_0 channel (with channel spins 2 and 3) dominating the decay of levels which the α_1 channel (with channel spin 2) also populates. (As a test of this conclusion, the program was run with only the α_0 and α_1 channels, i.e., setting $T_c^{J^\pi} \equiv 0$ for all the proton channels; $\langle\sigma v\rangle_{\alpha_1\gamma}/\langle\sigma v\rangle_{\alpha_0\gamma} \approx$ 0.43 at $T_9 = 5.0$ resulted.)

Using the data of this calculation presented in table 9, equations 48a and b may be used to extract $\langle\sigma v\rangle_{p\gamma}$ and $\langle\sigma v\rangle_{\alpha\gamma}$. If $\langle\sigma v\rangle_{p\gamma} = F(T)\langle\sigma v\rangle_{p_0\gamma}$, where $\langle\sigma v\rangle_{p_0\gamma}$ is given in table 6, it follows that $F(T) = 0.92$, 0.95, 0.98 and 0.996, at $T_9 = 5.0$, 4.0, 3.0 and 2.0 respectively. Similarly, if $\langle\sigma v\rangle_{\alpha\gamma} = G(T)\langle\sigma v\rangle_{\alpha_0\gamma}$, $G(T) = 0.83$, 0.92, 0.98 and 0.998, at $T_9 = 5.0$, 4.0, 3.0 and 2.0 respectively.

Total photodisintegration rates, including contributions of excited states of the residual nuclei may be obtained most simply from (51) and the $\langle\sigma v\rangle_{p\gamma}$ and $\langle\sigma v\rangle_{\alpha\gamma}$ given above. From (51) and (31)

$$\lambda_{\gamma p} = \frac{G_{Al}}{g^0_{Al}} \frac{\langle\sigma v\rangle_{p\gamma}}{\langle\sigma v\rangle_{p_0\gamma}} \lambda_{\gamma p_0} \tag{61}$$

and similarly for $\lambda_{\gamma\alpha}$; $\lambda_{\gamma p_0}$ and $\lambda_{\gamma\alpha_0}$ were given in table 7. Writing

$\lambda_{\gamma p} = A(T)\lambda_{\gamma p_0}$, $A(T) \approx 1.02$ and 1.01 for $T_9 = 5.0$ and 4.0 respectively, and $A(T) \approx 1.00$ for $T_9 \leq 3.0$. Similarly, if $\lambda_{\gamma\alpha} = B(T)\lambda_{\gamma\alpha_0}$, $B(T) \approx 1.01$ for $T_9 = 5.0$ and $B(T) \approx 1.00$ for $T_9 \leq 4.0$.

While considerable uncertainty must be attached to the type of calculations outlined above, the conclusions that $\lambda_{\gamma\alpha} \approx \lambda_{\gamma\alpha_0}$ and $\lambda_{\gamma p} \approx \gamma_{\gamma p_0}$, i.e., that no strong rate enhancements are present due to photodisintegration to excited states of the residual nuclei, are probably correct.

APPENDIX II. DEAD TIME CORRECTIONS

At each of the resonances studied, it was necessary to obtain a spectrum characteristic of the gamma ray cascades of the particular level. In most cases, three spectrum measurements were taken at each resonance.

1) The measurement labelled SPEC (SPECtrum) was taken for integrated charge Q at a bombarding energy slightly above the resonance energy, i.e., either on the thick target plateau, on the peak of a thin target yield measurement, or on the rapidly rising front edge of a yield curve.

2) The measurement labelled RB (Room Background) was taken with the beam intercepted by a quartz plate located 2 meters from the target chamber. The quartz plate did not produce appreciable background, and, as will be shown, this spectrum was multiplied by a very small coefficient in the final determination of the actual resonance spectrum.

3) The measurement labelled BOR (Background-Off-Resonance) was taken for integrated charge Q at a bombarding energy slightly below the resonance energy, i.e., either completely off the resonance, or near the bottom of the rapidly rising front edge of the resonance yield curve. In particular, the BOR spectrum contained less resonant contribution than the SPEC spectrum.

For the count rates encountered (typically of the order of 1.3×10^3 sec^{-1}, the highest ever used was about 21×10^3 sec^{-1}), the dead time of the pulse height analyzer is not negligible. (Dead

time refers to the time during which the analyzer is occupied in digitizing and storing a pulse, and is not capable of accepting a pulse presented to it.) The following procedure was used to correct for these effects.

For the spectrum measurements, both the clock time and the analyzer live time (given by the clock time minus the dead time, this is available as an optional output on the RIDL analyzer) were recorded. Since the live time corresponds to the length of time the analyzer was capable of accepting a pulse, it is evident that the SPEC measurement contains a room background contribution equal to that which would be obtained from a room background measurement of duration LTSPEC (the recorded live time of the SPEC measurement). Thus as a correction for room background, the RB spectrum was scaled by the ratio LTSPEC/LTRB and subtracted from the SPEC run; similarly the same RB spectrum, scaled by the ratio LTBOR/LTRB was subtracted from the BOR run.

Additional corrections were determined with the aid of the single channel analyzer (SCA). The channel numbers of the pulse height analyzer corresponding to the upper and lower bounds of the SCA window were determined by gating the analyzer with the SCA for a short time. (Reference to figure 3 might be helpful here.) During the three spectrum measurements, the SCA drove a scalar, and these scalar readings were recorded as SCL(SPEC), SCA(RB), and SCL(BOR). The IBM 7094 computer which handled the PHA output was given the upper and lower channel numbers of the SCA window; the computer then determined the number of pulses in the analyzer

channels corresponding to the SCA window. These were labelled WNDW(SPEC), WNDW(RB), and WNDW(BOR).

If spectrum pulses are fairly regular in time, the appropriate correction for dead time effects is just to scale the analyzer counts per channel by the ratio TT/LT, where TT refers to the "true" or "clock" time. However, since the beam induced count rate may be a rapidly varying function of time (if the beam current fluctuates), it would not be correct to apply such an average correction factor, and more care is required. The appropriate factor is simply the ratio of the beam-induced scalar counts to the beam-induced window counts; i.e., for run A, where A is either the SPEC or BOR run:

$$\mathrm{COEF(A)} = \left[\mathrm{SCL(A)} - \frac{\mathrm{TTA}}{\mathrm{TTRB}}\,\mathrm{SCL(RB)}\right] \Big/ \left[\mathrm{WNDW(A)} - \frac{\mathrm{LTA}}{\mathrm{LTRB}}\,\mathrm{WNDW(RB)}\right] \tag{62}$$

The fully corrected, beam-induced, SPEC spectrum is then

$$\mathrm{COEF(SPEC)}\left([\mathrm{SPEC}] - \frac{\mathrm{LTSPEC}}{\mathrm{LTRB}}[\mathrm{RB}]\right) \tag{63}$$

and the fully corrected, beam-induced, BOR spectrum is

$$\mathrm{COEF(BOR)}\left([\mathrm{BOR}] - \frac{\mathrm{LTBOR}}{\mathrm{LTRB}}[\mathrm{RB}]\right) \tag{64}$$

The spectrum characteristic of the resonance in question is obtained from the difference of the above two spectra. The coefficients on the RB spectrum in equations 63 and 64 were very near 1, thus the net coefficient applied to the RB spectrum was very nearly zero in this final difference spectrum.

Even though the above equations represent the completely general correction factors, the full expressions were not always used. In the early stages of the work, the approximation

$$COEF(A) \approx SCL(A) / WNDW(A) \qquad (65)$$

was used; equation 62 reduces to this value for count rates much larger than room background (as was almost always the case for the SPEC measurement). In addition, for a uniform count rate, the approximate equality of equation 65 is an identity. At all stages of the experimental program, great effort was expended on careful tuning and maintenance of the accelerator to insure beam stability. If the beam current was interrupted during a measurement, the entire measurement was repeated.

Although the programs were later modified to use the completely general equations, there was only negligible effect on the SPEC measurements. However, use of equation 62 proved to be impossible for the BOR in many cases. On very low count rate BOR measurements, the denominator of equation 62 approaches zero; statistical variations in the number of window counts in the BOR and RB runs then lead to meaningless values of COEF(BOR). Thus it was necessary to revert to equation 65 in these cases; in general the programs calculated COEF(A) by equation 65 on any measurement for which $SCL(A)/WNDW(A) < 1.05$.

APPENDIX III. CONTAMINANT TESTS WITH ELASTIC SCATTERING

For some of the targets considered in this experimental work, elastic scattering of alphas was used to test for contaminants. For these tests, a thin carbon foil (10-20 $\mu g/cm^2$) was positioned beside the solid Ta target blanks during the target evaporation. While the target blank was transferred to the pyrex target chamber for gamma ray yield experiments, the foil was transferred to a small scattering chamber on the electrostatic analyzer leg of the 3 MeV accelerator. Alpha particles at incident energy of 2 MeV were then scattered through the foil. An Ortec surface barrier Si detector was positioned behind a small aperture at 90° to the beam; the foil was positioned to bisect the angle between the beam and detector, thus all scattered particles passed through equal foil thicknesses. A sample spectrum is shown in figure 19, together with a sketch of the geometry.

For alpha particles, the energy E_A of particles scattered at 90° from a nucleus of atomic number A is

$$E_A = \frac{A-4}{A+4} E_0 \tag{66}$$

where E_0 is the incident energy. At E_0 = 2 MeV, the C - O and O - Mg peak separations are 200 and 230 keV respectively. If Rutherford scattering is assumed, the number of counts in the elastic scattering peak for each nucleus may be related to the areal density of the nucleus in question. No elastic scattering anomalies have been detected for the $^{16}O + \alpha$ reaction below 2.4 MeV (Cameron, 1953);

and for the higher Z peaks, Coulomb elastic scattering should dominate any nuclear resonance anomalies for such low alpha energies. From the Rutherford scattering cross section, one may easily deduce, for a lab angle of 90°:

$$\frac{N_A}{N_B} = \frac{\text{number of counts in peak A}}{\text{number of counts in peak B}} \left(\frac{Z_B}{Z_A}\right)^2 \sqrt{\frac{1 - 16/M_B^2}{1 - 16/M_A^2}} \qquad (67)$$

where N_A, Z_A, M_A = average number density, charge number, and mass number of nucleus A, and similarly for nucleus B. The main factor in equation 67 is just the ratio of the square of the charge numbers as expected, the square root term represents a small correction for center-of-mass effects on the solid angle of the counter.

FIGURE 19: Alpha Particle Spectrum

This figure shows a typical spectrum recorded by the surface barrier detector. A 2 MeV beam of alpha particles was scattered through the carbon foil as indicated on the figure. Peaks due to elastic scattering from carbon, oxygen, and magnesium are clearly visible. In addition, a thin layer of gold was evaporated on the carbon foil to aid in uniform magnesium deposition. Alpha particles scattered off the high Z gold layer result in an intense elastic peak at higher energies and provide the background visible above the Mg peak. A spectrum similar to this was measured on a carbon foil which had been transferred directly to the scattering chamber without the vacuum depositions. A measure of the oxygen associated with the carbon foil was thus obtained and subtracted from the spectrum of this figure. Analysis of the resulting spectrum by equation 67 gave $N_0/N_{Mg} < 10\%$.

FIGURE 19

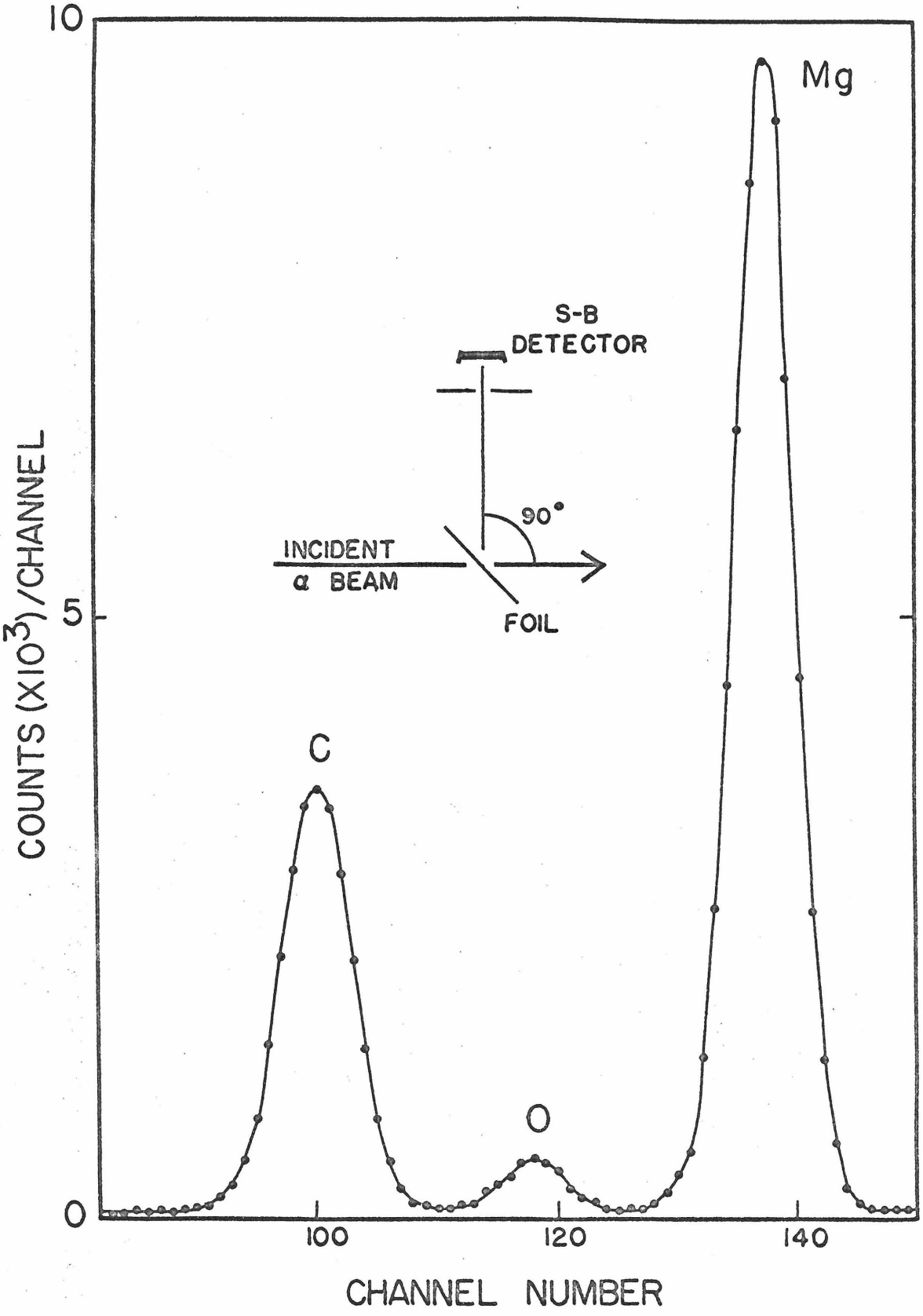
10
5
0
COUNTS (X10^3)/CHANNEL
Mg
S-B
DETECTOR
90°
INCIDENT
α BEAM
FOIL
C
O
100
120
140
CHANNEL NUMBER

REFERENCES

F. Ajzenberg-Selove and T. Lauritsen, 1959, Nucl. Phys. 11, 1.

S. C. Anspach, L. M. Cavallo, S. B. Garfinkel, J. M. R. Hutchinson, and C. N. Smith, 1965, National Bureau of Standards, Misc.-Publ. 260-9.

Y. P. Antoufiev, L. M. El-Nadi, D. A. E. Darwish, O. E. Badawy, and P. V. Sorokin, 1963, Nucl. Phys. 46, 1.

Y. P. Antoufiev, O. E. Badaway, L. M. El-Nadi, D. A. E. Darwish, and P. V. Sorokin, 1964, Nucl. Phys. 54, 301.

R. E. Azuma, L. E. Carlson, A. M. Charlesworth, K. P. Jackson, N. Anyas-Weiss, and B. Lalovic, 1966, Can. J. Phys. 44, 3075.

N. A. Bahcall and W.A. Fowler, 1969, submitted to Astrophys. J.

M. J. Berger and S. M. Seltzer, 1964, Studies in Penetration of Charged Particles in Matter, NAS-NRC Publication 1133, Nuclear Science Series Report No. 39.

H. Bichsel, 1964, Studies in Penetration of Charged Particles in Matter, NAS-NRC Publication 1133, Nuclear Science Series Report No. 39.

D. Bodansky, D. Clayton, and W. A. Fowler, 1968, Astrophys. J. Suppl. No. 48, 16, 299.

S. C. Boydell, 1967, University of Queensland, private communication.

R. L. Bramblett, J. T. Caldwell, B. L. Berman, R. R. Harvey, and S. C. Fultz, 1966, Phys. Rev. 148, 1198.

J. R. Cameron, 1953, Phys. Rev. 90, 839.

C. H. Chang, C. S. Cook, H. Primakoff, 1953, Phys. Rev. 90, 544.

D. Clayton, 1968, Principles of Stellar Evolution and Nucleosynthesis, McGraw Hill, New York.

C. M. Davisson, 1965, Alpha-, Beta- and Gamma-Ray Spectroscopy, ed. by K. Siegbahn, North-Holland Publishing Co., Amsterdam, Ch. II.

P. M. Endt and A. Heyligers, 1960, Physica 26, 230.

P. M. Endt and C. Van der Leun, 1962, Nucl. Phys. 34, 1.

P. M. Endt and C. Van der Leun, 1967, Nucl. Phys. A105, 1.

G. A. P. Engelbertink and P. M. Endt, 1966, Nucl. Phys. 88, 12.

U. Fano, 1952, National Bureau of Standards, Applied Mathematics Series, No. 13.

W. A. Fowler, G. R. Caughlan, and B. A. Zimmerman, 1967, Ann. Rev. Astr. and Astrophys. 5, 525. (referred to as FCZ)

W. A. Fowler and F. Hoyle, 1964, Astrophys. J. Suppl. No. 91, 9, 201.

W. A. Fowler and J. L. Vogl, 1964, Lectures in Theoretical Physics, Vol. VI, University of Colorado Press, Boulder.

E. F. Gibson, K. Battleson, and D. K. McDaniels, 1968, Phys. Rev. 172, 1004.

A. Gilbert and A. G. W. Cameron, 1965, Can. J. Phys. 43, 1446.

H. E. Gove, 1959, Nuclear Reactions I, ed. by P. M. Endt and M. Demeur, North Holland Publishing Company, Amsterdam, Ch. VI.

H. E. Gove, A. E. Litherland, and R. Batchelor, 1961, Nucl. Phys. 26, 480.

P. J. Grant, F. C. Flack, J. G. Rutherglen, W. M. Deuchars, 1954, Proc. Phys. Soc. (London) 67A, 751.

G. W. Grodstein, 1957, X-Ray Attenuation Coefficients from 10 keV to 100 MeV, National Bureau of Standards Circular 583.

Harshaw Chemical Co., 1962, Harshaw Scintillation Phosphors, Cleveland, Ohio.

R. L. Heath, 1964, Scintillation Spectrometry I, IDO-16880-1 AEC Research and Development Report, TID-4500.

R. Hofstader, 1948, Phys. Rev. 74, 100.

R. Hofstader, E. W. O'Dell, and C. T. Schmidt, 1964, Transactions of the IEEE NS-11, 12.

L. Katz and A. S. Penfold, 1952, Rev. Mod. Phys. 24, 28.

R. Kavanaugh, 1956, Ph.D. Thesis, California Institute of Technology.

A. A. Kraus, A. P. French, W. A. Fowler, and C. C. Lauritsen, 1953, Phys. Rev. 89, 299.

J. D. Larson, 1965, Ph.D. Thesis, California Institute of Technology.

H. Leutz, G. Schulz, and L. Van Gelderen, 1966, Nucl. Instr. and Meth. 40, 257.

R. L. Macklin, J. H. Gibbons, and T. Inada, 1963, Nucl. Phys. 43, 353.

J. S. Marshall, and A. G. Wood, 1937, Can. J. Research A15, 39.

L. Meyer-Schutzmeister, Z. Vager, R. E. Segel, and P. P. Singh, 1968, Nucl. Phys. A108, 180.

W. F. Miller and W. J. Snow, 1961, Nucleonics 19, 174.

M. C. Moxon and E. R. Rae, 1963, Nucl. Instr. and Meth. 24, 445.

J. H. Neiler and P. R. Bell, 1965, Alpha-, Beta- and Gamma-Ray Spectroscopy, ed. by K. Siegbahn, North-Holland Publishing Co., Amsterdam, Ch. V.

L. P. Nielsen, 1961, Mat. Fys. Vid. Dan. Medd. Selsk. 33, No. 6.

D. W. Palmer, J. G. Skofronick, D. G. Costello, A. L. Morsell, W. E. Kane, and R. G. Herb, 1963, Phys. Rev. 130, 1153.

P. D. M. Parker, 1963, Ph.D. Thesis, California Institute of Technology.

J. D. Pearson, 1963, Ph.D. Thesis, California Institute of Technology.

H. J. Rose, F. Riess, and W. Trost, 1964, Nucl. Phys. 52, 481.

M. E. Rose, 1953, Phys. Rev. 91, 610.

E. Rost, 1962, Phys. Rev. 128, 2708.

P. P. Singh, R. E. Segel, L. Meyer-Schutzmeister, S. S. Hanna, and R. G. Allas, 1965, Nucl. Phys. 65, 577.

P. R. Smith and P. M. Endt, 1958, Phys. Rev. 110, 1442.

P. J. M. Smulders and P. M. Endt, 1962, Physica 28, 1093.

B. J. Snyder, 1967, Nucl. Instr. and Meth. 46, 173.

P. H. Stelson, 1954, Phys. Rev. 96, 1584.

L. C. Thompson, 1964, Nucl. Instr. and Meth. 25, 333.

J. W. Truran, A. G. W. Cameron, and A. Gilbert, 1966, Can. J. Phys. 44, 563.

J. W. Truran, C. J. Hansen, A. G. W. Cameron, and A. Gilbert, 1966a, Can. J. Phys. 44, 451.

H. Ullrich, 1964, Phys. Lett. 12, 114.

C. Van der Leun and P. M. Endt, 1958, Phys. Rev. 110, 96.

C. Van der Leun and N. C. Burhoven Jaspers, 1966, Nucl. Phys. 88, 235.

C. Van der Leun, D. M. Sheppard and P. M. Endt, 1967, Nucl. Phys. A100, 316.

E. Vogt, 1962, Rev. Mod. Phys. 34, 723.

E. Vogt, G. Michaud, and H. Reeves, 1965, Phys. Lett. 19, 570.

E. Vogt, 1969, Advances in Nuclear Physics 1, 261.

H. A. Weidenmüller, 1964, Notes of Lecture Series at California Institute of Technology.

J. A. Weinman, L. Meyer-Schutzmeister, and L. L. Lee, Jr., 1964, Phys. Rev. 133B, 590.

W. Whaling, 1958, Handbuch der Physik 34, 193.

E. A. Wolicki, R. Jastrow, and F. Brooks, 1956, NRL Report 4833.

J. M. Wyckoff, B. Ziegler, H. W. Koch, and R. Uhlig, 1965, Phys. Rev. 137B, 576.

C. D. Zerby and H. S. Moran, 1961, Nucl. Instr. and Meth. 14, 115.

Table 1

Summary of $^{27}Al(p,\gamma)^{28}Si$ Yield Data

Resonance Energy (keV)[a]	$(2J+1)\Gamma_p\Gamma_\gamma/\Gamma$ (eV)[b]	Method of Analysis[c]			Γ (keV)[a]
		thick	thin	N_γ	
327	0.023 ± 0.005	x		3	
406	0.12 ± 0.02	x		3	
447	0.018 ± 0.006	x		5	
505, 507 [d]	0.86 ± 0.12	x		1	
612	0.059 ± 0.009	x		3	
633	3.0 ± 0.4	x		1	
655	1.39 ± 0.17	x		1	
679	0.65 ± 0.08	x		1	
731	1.55 ± 0.19	x		1	
736	1.91 ± 0.25	x		1	
742	0.32 ± 0.07	x		3	
760	1.51 ± 0.20	x		1	
767	2.1 ± 0.3	x		1	
774	4.9 ± 0.6	x		1	
885	0.16 ± 0.03	x		2	
923	1.56 ± 0.20	x		1	
937	2.1 ± 0.3	x		1	
992	22.0 ± 2.4	x		1	
1002	0.58 ± 0.12		x	1	
1025	3.9 ± 0.5	x		1	
1090	1.08 ± 0.13	x		1	
1098	0.54 ± 0.06	x		1	
1118	10.2 ± 2.0		x	1	
1172	1.11 ± 0.17	x	x	2	
1183	2.7 ± 0.4	x	x	1	
1200	12.2 ± 2.4		x	1	
1213	5.5 ± 1.2		x	1	
1262	7.0 ± 0.9	x		1	
1276	0.63 ± 0.09	x		2	
1317	8.9 ± 1.1	x		1	
1328	4.7 ± 0.8	x		2	
1364, 1365 [d]	9.1 ± 1.0	x		1	
1381	51. ± 6.	x		1	
1388	40. ± 5.	x		1	
1435	0.16 ± 0.06		x	4	
1451	2.4 ± 0.6		x	1	3.
1499	1.1 ± 0.3		x	2	
1514	15.7 ± 3.5		x	1	4.
1568	0.63 ± 0.18		x	2	
1579	1.56 ± 0.29	x	x	2	$\lesssim$ 2.
1589	9.9 ± 1.2	x	x	1	$\lesssim$ 2.

(continued)

Table 1 (continued)

Resonance Energy (keV)[a]	$(2J+1)\Gamma_p\Gamma_\gamma/\Gamma$ (eV)[b]		Method of Analysis[c] thick	thin	N_γ	Γ (keV)[a]
1647	0.57	± 0.21		x	4	
1669	19.2	± 2.3	x	x	1	2.
1680	3.7	± 0.4	x	x	1	≲ 2.
1709	1.1	± 0.3		x	4	
1726	14.7	± 2.4	x	x	2	≲ 2.
1746	4.0	± 1.0		x	2	7.
1797	14.8	± 1.8	x	x	1	≲ 2.
1838	2.3	± 0.6		x	2	
1909	2.7	± 1.1		x	5	13.
1917	5.9	± 0.9	x	x	1	≲ 2.
1976	6.6	± 2.6		x	5	12.
1978	4.8	± 1.5		x	4	≲ 2.
2041	4.2	± 1.6		x	5	8.
2054	21.8	± 2.6	x	x	1	≲ 2.
2067	0.56	± 0.22		x	5	
2084	0.36	± 0.15		x	5	
2106	2.7	± 1.1		x	5	24.
2114	1.3	± 0.5		x	5	
2120	2.7	± 1.1		x	5	6.
2140	0.9	± 0.4		x	5	
2144	1.1	± 0.4		x	5	
2168	1.5	± 0.6		x	5	≲ 2.
2171	2.8	± 0.9		x	4	≲ 2.
2183	0.9	± 0.4		x	5	
2190	1.9	± 0.6		x	4	≲ 2.
2212	34.	± 5.	x	x	3	≲ 2.
2221	33.	±12.		x	5	50.
2249	23.	± 8.		x	5	41.
2296	0.55	± 0.23		x	5	
2312	5.3	± 1.7	x	x	5	≲ 2.
2320	13.0	± 2.7	x	x	4	≲ 2.
2334	0.69	± 0.29		x	5	
2365	3.2	± 1.2		x	5	4.
2375	6.1	± 2.4		x	5	6.
2407	1.3	± 0.5		x	5	9.
2447	1.1	± 0.4		x	5	6.
2481	5.3	± 2.2		x	5	5.
2489	42.	± 8.	x	x	3	2.
2522	27.	± 7.		x	3	≲ 2.
2537	22.	± 9.		x	5	12.
2560	2.8	± 1.1		x	5	4.
2584	17.	± 7.		x	5	26.

[a] Lab energy scale

[b] C. M. energy scale

[c] Refer to Chapters IV and V

[d] Total strength for both resonances

Table 2

Spectrum Analysis Errors
$^{27}Al(p,\gamma)^{28}Si$

Method Number	Error in N_γ [a]
1	$\lesssim$ 10%
2	$\lesssim$ 12%
3	$\lesssim$ 12%
4	$\lesssim$ 20%
5	$\lesssim$ 30%

[a] Refer to Chapter VI

Table 3

Summary of $^{24}Mg(\alpha,\gamma)^{28}Si$ Resonance Yield Data

Resonance Energy in keV[a,b]	$(2J+1)\Gamma_\alpha\Gamma_\gamma/\Gamma$ in eV[c]
1358 ± 7	0.0019 ± 0.0006
1533	0.081 ± 0.020
1788	0.058 ± 0.014
1868	0.045 ± 0.010
1954	0.119 ± 0.026
1968	0.29 ± 0.06
2097	0.037 ± 0.008
2238	0.053 ± 0.011
2325	0.091 ± 0.019
2380	0.074 ± 0.019
2437	0.29 ± 0.06
2566	0.067 ± 0.015
2580	0.19 ± 0.03
2634	0.50 ± 0.10
2692	0.060 ± 0.012
2704	0.028 ± 0.008

[a] Resonance energies from Endt and Van der Leun (1967), except for the 1358 keV resonance

[b] Lab energy scale

[c] C. M. energy scale

Table 4

$^{24}Mg(\alpha,\gamma)^{28}Si$ Thick (Stopping) Target Data

Bombarding Energy (MeV)	SCA Counts - Room Background per $10^{15}\alpha$ [a]	Upper Limit to $\sum_{E_r<E_\alpha} (2J_\gamma+1)\Gamma_\alpha\Gamma_\gamma/\Gamma$ (eV)[b]
1.0	0.5 ± 0.7	0.0006
1.15	1.2 ± 0.8	0.0011
1.30	2.1 ± 0.8	0.0019

[a] SCA lower bias was set at 7.9 MeV. Only room background was subtracted.

[b] See text, section VII.C, for method of calculation. Given in C.M. energy units.

Table 5

Comparison to $(2J+1)\Gamma_p\Gamma_\gamma/\Gamma$[a] from Previous Investigators

Resonance Energy (keV)	This Paper	Nordhagen[b]	Smith[c]	Luukko[e]	Spring[f]	Nordhagen[g]	Gibson[i]	Antoufiev[j]	Engelbertink[l]
633	3.1 ± 0.4		2.5 ± 0.7[d]			5.4 ± 1.8[d]			5.3 ± 0.8
774	5.1 ± 0.7		4.7 ± 1.5	5.5 ± 1.7		10.2 ± 3.0			
937	2.2 ± 0.3	2.1							
992	22.8 ± 2.5				38. ± 6.	40[h]	(40)	17.	
1118	10.6 ± 2.1	14.5							
1183	2.8 ± 0.4					4.7 ± 1.5		1.7	
1262	7.3 ± 1.0	8.8					14	6.2	
1317	9.2 ± 1.0	9.5					20	14.	
1364-5	9.4 ± 1.0	9.6					21	7.8	
1381	53. ± 6.					65[h]	57	10.2	
1388	42. ± 5.					50[h]	39	9.9	
1514	16.3 ± 3.6						17	7.4	
1589	10.3 ± 1.2						15	9.5	
1669	19.9 ± 2.4						20	6.1	
1726	15.2 ± 2.5						27		
2054	23. ± 2.5						33	7.9	
2212	35. ± 6.						43	24.[k]	
2489	44. ± 8.							32.	

Table 5 Footnotes

[a] Laboratory energy scale.

[b] R. Nordhagen, Nucl. Phys. 44 (1963) 130; R. Nordhagen and A. Tveter, Nuclear Phys. 56 (1964) 337 and 63 (1965) 529.

[c] Smith and Endt (1958) (measured value at 774 keV only).

[d] From relative yields of Endt and Heyligers (1960), normalized to the absolute value at the 774 keV resonance.

[e] A. Luukko, Soc. Sci. Fenn. Comm. Phys.-Mat. 31 (1965) Nr. 6.

[f] E. Spring, Soc. Sci. Fenn. Comm. Phys.-Mat. 28 (1963) Nr. 6.

[g] Nordhagen and Smith (1961) unpublished work quoted by Endt and Van der Leun (1962) (values at 774 and 1183 keV only).

[h] From "approximate yields" given by R. Nordhagen (Nucl. Instr. Meth. 12 (1961) 291) scaled by ratio of the resonance strengths for the 774 keV resonance given by references of footnotes c and g.

[i] From Gibson et al. (1968), all values relative to 40 eV at the 992 keV resonance, stated errors ±30%.

[j] From Antoufiev et al. (1963) and Antoufiev et al., Nucl. Phys. 56 (1964) 401. Measured $(2J+1)\Gamma_p\Gamma_{\gamma_1}/\Gamma$ and, for most of the resonances, $\Gamma_{\gamma_1}/\Gamma_\gamma$. Where Antoufiev did not measure this ratio, it was taken from Boydell (1967).

[k] Either 24 or 2.4, the two references of footnote j differ by a factor of 10 on this resonance.

[l] Engelbertink and Endt (1966).

Table 6

Stellar Interaction Rates

Temp 10^9 °K	$N_A\langle\sigma v\rangle^0$	
	$^{27}Al(p,\gamma)^{28}Si$	$^{24}Mg(\alpha,\gamma)^{28}Si$
0.1	1.43×10^{-8}	3.27×10^{-56}
0.2	8.47×10^{-4}	2.50×10^{-27}
0.3	4.25×10^{-2}	9.12×10^{-18}
0.4	4.27×10^{-1}	6.25×10^{-13}
0.5	2.19×10^{-0}	5.70×10^{-10}
0.6	7.67×10^{-0}	5.68×10^{-8}
0.7	$2.09 \times 10^{+1}$	1.55×10^{-6}
0.8	$4.75 \times 10^{+1}$	1.86×10^{-5}
0.9	$9.38 \times 10^{+1}$	1.29×10^{-4}
1.0	$1.66 \times 10^{+2}$	6.06×10^{-4}
1.5	$1.07 \times 10^{+3}$	6.64×10^{-2}
2.0	$3.01 \times 10^{+3}$	7.48×10^{-1}
2.5	$5.91 \times 10^{+3}$	3.45×10^{-0}
3.0	$9.46 \times 10^{+3}$	$1.02 \times 10^{+1}$
3.5	$1.34 \times 10^{+4}$	$2.35 \times 10^{+1}$
4.0	$1.75 \times 10^{+4}$	$4.48 \times 10^{+1}$
4.5	$2.17 \times 10^{+4}$	$7.58 \times 10^{+1}$
5.0	$2.58 \times 10^{+4}$	$1.17 \times 10^{+2}$

Table 7

Photodisintegration Rate λ_γ of ^{28}Si (sec^{-1})

	Temperature (10^9 °K)			
Channel	1.5	2.0	2.5	3.0
(γ,p_0)	2.65×10^{-25}	6.18×10^{-15}	1.16×10^{-8}	1.90×10^{-4}
(γ,α_0)	2.23×10^{-24}	9.34×10^{-15}	6.45×10^{-9}	5.66×10^{-5}
(γ,α_0+p_0)	2.50×10^{-24}	1.55×10^{-14}	1.81×10^{-8}	2.47×10^{-4}
	Temperature (10^9 °K)			
Channel	3.5	4.0	4.5	5.0
(γ,p_0)	2.03×10^{-1}	$3.88 \times 10^{+1}$	$2.35 \times 10^{+3}$	$6.32 \times 10^{+4}$
(γ,α_0)	4.01×10^{-2}	$5.79 \times 10^{+0}$	$2.86 \times 10^{+2}$	$6.60 \times 10^{+3}$
(γ,α_0+p_0)	2.43×10^{-1}	$4.46 \times 10^{+1}$	$2.63 \times 10^{+3}$	$6.98 \times 10^{+4}$

Table 8

Photoexcitation Lifetimes for ^{28}Si Levels below 8 MeV

Initial State (MeV)	J^π	Final State (MeV)	J^π	$\tau_{sp}(i\rightarrow f)$[a] (psec)	Photoexcitation Lifetime ($f\rightarrow i$)[b] $T_9 = 3$ (sec)	$T_9 = 5$
1.78	2^+	0.	0^+	0.58	1.1×10^{-10}	7.2×10^{-12}
4.62	4^+	1.78	2^+	0.061	2.0×10^{-9}	2.5×10^{-11}
6.28	3^+	1.78	2^+	1.59	4.1×10^{-5}	3.9×10^{-8}
6.88	3^-	1.78	2^+	8.21	2.2×10^{-3}	8.1×10^{-7}
6.89	4^+	1.78	2^+	0.165[c]	3.5×10^{-5}	1.3×10^{-8}
7.38	1^+	1.78	2^+	0.024	1.0×10^{-4}	1.8×10^{-8}
7.42	2^+	0.	0^+	0.043	2.5×10^{-2}	2.6×10^{-7}
7.80	3^+	1.78	2^+	0.39	3.6×10^{-3}	3.2×10^{-7}
7.93	2^+	0.	0^+	unknown	-	-
		$1/\lambda_{\gamma\, p_0 + \alpha_0}(^{28}\mathrm{Si})$[d] =			4.0×10^{-3}	1.4×10^{-5}

[a] Spontaneous decay lifetime for given transition, calculated from total level lifetime and level branching ratios measured by Gibson *et al.* (1968).

[b] Discussed in Appendix I [c] From Endt and Van der Leun (1967) [d] From table 7

Table 9

$N_A\langle\sigma v\rangle$ for Excited States

	Temperature (10^9 °K)				
	1.0	2.0	3.0	4.0	5.0
$\langle\sigma v\rangle_{p_1\gamma}/\langle\sigma v\rangle_{p_0\gamma}$	0.11	0.17	0.21	0.24	0.27
$\langle\sigma v\rangle_{p_2\gamma}/\langle\sigma v\rangle_{p_0\gamma}$	0.03	0.05	0.07	0.10	0.12
$\langle\sigma v\rangle_{\alpha_1\gamma}/\langle\sigma v\rangle_{\alpha_0\gamma}$	0.02	0.01	0.01	0.02	0.04
$N_A\langle\sigma v\rangle_{p_0\gamma}$:					
Calculated[a]	6.37×10^2	6.81×10^3	1.56×10^4	2.36×10^4	3.02×10^4
Experimental[b]	1.66×10^2	3.01×10^3	9.46×10^3	1.75×10^4	2.58×10^4
$N_A\langle\sigma v\rangle_{\alpha_0\gamma}$:					
Calculated[a]	5.15×10^{-4}	2.37×10^0	4.99×10^1	2.31×10^1	5.75×10^2
Experimental[b]	6.06×10^{-4}	7.48×10^{-1}	1.02×10^1	4.48×10^1	1.17×10^2

[a] See Appendix I.C.

[b] From table 6.